REPORT NO.
UCB/SESM-73/07

STRUCTURAL ENGINEERING
AND STRUCTURAL MECHANICS

NONLINEAR ANALYSIS OF REINFORCED CONCRETE SLABS AND SHELLS

by

C. S. LIN

APRIL 1973

DEPARTMENT OF CIVIL ENGINEERING
UNIVERSITY OF CALIFORNIA
BERKELEY, CALIFORNIA

Structures and Materials Research
Department of Civil Engineering
Division of Structural Engineering
and
Structural Mechanics

NONLINEAR ANALYSIS OF REINFORCED CONCRETE SLABS AND SHELLS

by

Cheng-Shung Lin

Faculty Investigator: A.C. Scordelis

Prepared under the Sponsorship of
National Science Foundation
Grant GK-28073X

College of Engineering
Office of Research Services
University of California
Berkeley, California

April 1973

ABSTRACT

A general finite element method of analysis is developed to analyze reinforced concrete slabs of arbitrary geometry and free-form shells under dead loads and monotonically increasing live loads. The method can be used to trace the load-deformation response and crack propagation through the elastic, inelastic and ultimate ranges. The internal concrete and steel stresses can also be determined for any stage of the response history.

The nonlinear analysis includes cracking of the concrete, the tension stiffening effect of concrete between the cracks, and the nonlinear stress-strain relationships for the concrete and steel reinforcement. The concrete is assumed to be brittle in tension and elasto-plastic in compression. The von Mises yield criterion and the associated flow rule are adopted to govern the plastic behavior of the concrete. The reinforcing steel is considered as a one-dimensional elasto-plastic material.

A layered triangular shell finite element taking account of the coupling effect between the membrane action and the bending action is developed. An incremental tangent stiffness method is used to obtain a numerical solution.

A general computer program is developed to implement the analysis. A series of examples including beams, slabs and shells are analyzed. Validity of the method is studied by comparing the analytical results with experimental data. Effects of various important parameters are also discussed.

ACKNOWLEDGEMENTS

The author wishes to express his deepest appreciation to Professor A.C. Scordelis for his guidance, support and encouragement throughout the course of this research. The author is also grateful to Professors G.H. Powell and C.S. Hsu for serving as members of his thesis committee.

This research was sponsored by the National Science Foundation by Grant GK-28073X. The Computer Center at the University of California, Berkeley provided facilities for the computer work.

TABLE OF CONTENTS

	Page
ABSTRACT	i
ACKNOWLEDGEMENTS	ii
TABLE OF CONTENTS	iii
1. INTRODUCTION	1
1.1 General Remarks	1
1.2 Historical Background	2
1.3 Object and Scope	6
2. MATERIAL PROPERTIES AND CONSTITUTIVE RELATIONS	8
2.1 Introduction	8
2.2 Concrete	9
2.2.1 Stress-Strain Relationship	9
2.2.2 Failure Criteria	14
2.2.3 Uncracked Elastic Stiffness	21
2.2.4 Cracked Stiffness	21
2.2.5 Plastic Stiffness	26
2.2.6 Crushed Stiffness	30
2.3 Steel	30
2.4 Composite Layer System	31
2.5 Summary	33
3. FINITE ELEMENT IDEALIZATION	34
3.1 General Remarks	34
3.2 Displacement Formulation	35
3.3 Application to Shell Structures	38
3.4 Layered Discretization	43
3.4.1 Evaluation of the Element Stiffness	43

TABLE OF CONTENTS (Cont.)

3.4.2 Evaluation of the Layer Strains and Stress 45

3.4.3 Evaluation of the Unbalanced Nodal Forces. 45

3.5 Selection of Elements 46

3.6 Assemblage of Elements 49

3.6.1 Coordinate Transformation 49

3.6.2 Boundary Element. 54

3.6.3 Remarks 54

3.7 Summary. 55

4. NONLINEAR ANALYSIS 57

4.1 General Remarks 57

4.2 Review of Numerical Methods 58

4.3 Analysis of Reinforced Concrete Shells . . . 61

4.4 Evaluation of the Unbalanced Nodal Forces. . 65

4.5 Convergence Criteria 69

4.6 Computer Program 71

5. NUMERICAL EXAMPLES 77

5.1 General Remarks 77

5.2 Reinforced Concrete Beams 78

5.2.1 Example 1 -- Hypothetical Beams . . . 78

5.2.2 Example 2 -- Bresler-Scordelis Beam B3 86

5.3 Reinforced Concrete Slabs 92

5.3.1 Example 3 -- Cardenas Circular Slab C2 92

TABLE OF CONTENTS (Cont.)

5.3.2 Example 4 -- Cardenas Rectangular Slab B7 98

5.3.3 Example 5 -- McNeice Slab 104

5.4 Reinforced Concrete Shells 109

5.4.1 Example 6 -- Hedgren Cylindrical Shell 109

5.4.2 Example 7 -- Hyperbolic Paraboloid Shell 131

5.5 Computer Time 137

6. PARAMETER STUDIES 140

6.1 Introduction 140

6.2 Tension Stiffening Effect. 140

6.3 Load Increments. 144

6.4 Convergence Criteria 145

6.5 Yield Surface and Flow Rule. 149

6.6 Cracked Shear Constant 150

7. CONCLUSIONS 152

7.1 Summary 152

7.2 Conclusions 153

7.3 Recommendations for Further Studies 154

REFERENCES. 156

1. INTRODUCTION

1.1 General Remarks

Reinforced concrete shell structures possess many of the qualities of an ideal structure. They require a minimum amount of material and permit the covering of large areas without intermediate support. Their forms offer virtually unlimited possibilities for aesthetic and architectural expression. However, their design is usually still based on a linear elastic analysis assuming that the materials are uncracked, homogeneous, isotropic and linearly elastic. It has long been recognized that the reinforced concrete shells, and slabs as special forms of shells, are usually too heavily loaded to remain in the range of validity of linear elastic theory. Many of them experience considerable cracking even under normal service loads. In order to assess their true safety against failure and to ensure their serviceability at the working load, a complete analysis tracing their response through the elastic, inelastic and ultimate ranges is desirable.

Experiments on microconcrete models can very well render a clear understanding of the nonlinear behavior of the concrete shells, but are very expensive and technically difficult. Furthermore, a great many models are required to cover all the possible variations of the important variables. Hence, there is a need for a general method of analysis to complement, and eventually to replace, the physical experiments. It is believed that the ultimate solution is a method of

analysis confirmed by a few selected well-controlled experiments.

The development of an analytical model for reinforced concrete structures is complicated by the following facts.

1. The structural system is composed of two materials, concrete and steel.

2. The structural system has a continuously changing topology due to the cracking of the concrete under increasing load.

3. The stress-strain relationship for concrete is nonlinear and is a function of many variables. Constitutive relationship and failure criteria for concrete under multi-axial stress states are difficult to define.

4. Concrete deformations are influenced by creep and shrinkage and are dependent on load and environmental history.

5. Cracking in the concrete exhibits some degree of random characteristics.

6. Effects of dowel action in the steel reinforcement, aggregate interlocking and bond slip between the reinforcement and the concrete are difficult to model.

1.2 Historical Background

Classical thin shell theory yields differential equations whose complexity depends on the shell geometry. Closed form solutions are available only for a few very simple shapes under very simple loading and boundary conditions. Thanks

to the advent of high-speed digital computers and modern numerical methods, such as the finite element method, the analysis of free-form shells subjected to arbitrary loading and boundary conditions becomes possible.

The earliest published application of the finite element method to reinforced concrete structures was by Ngo and Scordelis [1.1]. In these studies, simple beams were analyzed in which the concrete and steel reinforcement were represented by plane stress triangular finite elements and special bond link elements were used to connect the steel to the concrete. Linear elastic analyses were performed on beams with predefined crack patterns to determine principal stresses in the concrete, stresses in the steel reinforcement and bond stresses. Ngo, Scordelis and Franklin [1.2] used this same approach to study shear in beams with diagonal tension cracks, considering the effect of stirrups, dowel shear, aggregate interlock and horizontal splitting along reinforcement near the support.

Nilson [1.3, 1.4] introduced nonlinear material properties and a nonlinear bond-slip relationship into the analysis and used an incremental loading technique to account for these nonlinearities. Cracking was accounted for by stopping the solution when an element indicated a tensile failure and thence redefining a new cracked structure which was again input into the computer and reloaded incrementally. The method was applied to concentric and eccentric reinforced tensile members subjected to loads applied longitudinally

through the reinforcing bars and the results were checked against experimental results.

Franklin [1.5] advanced the capability of the analytical method by developing an incremental loading procedure which can trace the response of plane stress systems from initial loading to failure in one continuous computer analysis. Instead of redefining the finite element mesh and nodal connectivities, the cracking of concrete was accounted for by modifying the material properties and redistributing the unbalanced stresses. Iterations are performed within each increment to account for the change of material properties. Franklin used special frame-type elements, quadrilateral plane stress elements, one-dimensional truss elements, two-dimensional bond links and tie links to study reinforced concrete frames with or without infilled shear panels.

Zienkiewicz et al [1.6, 1.7, 1.8, 1.9] have made plane stress studies of reinforced concrete structures which include tensile cracking and elasto-plastic behavior in compression using an "initial stress" approach. Cervenka [1.10] derived a constitutive relationship for the composite concrete-steel material, and studied reinforced concrete shear walls and spandrel beams under monotonically increasing or cyclic loading.

McCutcheon, Mirza, Mufti et al [1.11, 1.12, 1.13, 1.14, 1.15] have conducted an extensive research investigation on the application of the finite element method to reinforced concrete structures. They studied plane stress problems

using a modeling system similar to that of Nilson, extended to incorporated automatic cracking and bond failures in one continuous computer analysis. Prestressed concrete slabs have also been studied using an elasto-plastic concept to account for cracking.

Studies of reinforced concrete slabs by the finite element method have been presented by Jofriet and McNeice [1.16]. A progressive cracking procedure was used together with some semi-empirical bilinear moment curvature relationship. Bells and Elms [1.17, 1.18] adopted a similar material idealization to study slabs and shells. Recently Scanlon [1.19] has developed a layered finite element for reinforced concrete slabs which can account for the effects of cracking and time dependent behavior. The layered rectangular slab-elements can be cracked progressively layer by layer, and cracks are assumed to propagate only parallel and perpendicular to orthogonal reinforcements.

Rashid [1.20, 1.21, 1.22] and Wahl and Kasiba [1.23] have made extensive finite element studies of prestressed concrete nuclear reactor pressure vessels treated as axi-symmetrical solids. Rashid's work is the most advanced since it attempts to take into account cracking, temperature, creep and load history.

Schnobrich et al. [1.24, 1.25] have made significant contributions to the analysis of shear wall-frame systems as well as plates and shells. They used composite plane

stress quadrilateral elements, including the concrete stiffness and reinforcement stiffness, for the walls or frames, and a special flexural element for the frame and link elements to connect the wall elements to the frame elements. This work is similar to that by Franklin [1.5]. In their work on the plates and shells, a rectangular shallow shell layered finite element was developed. Owing to the inherent limitations of the finite element they used, the class of structures that can be analyzed are restricted to plates and shallow shells of constant thickness.

Lastly, in a recent state of the art paper by Scordelis [1.26], a comprehensive survey of the past and current research on the finite element analysis of reinforced concrete structures is presented. The paper concludes with a discussion of the major problems and questions needing answers on this general subject.

1.3 Object and Scope

The objective of this study is to develop a general method of analysis which can analyze reinforced concrete slabs of arbitrary geometry and free-form shells under dead loads and monotonically increasing live loads. The analysis includes tracing the load-deformation response and crack propogation and determining the internal concrete and steel stresses.

The nonlinear effects considered are cracking of the concrete, the tension stiffening effect of concrete between

cracks, and the nonlinear stress strain relationship for the concrete and steel reinforcement. Bond slip between the reinforcement and concrete, time dependent effects and thermal effects are not included. Also not considered are the effects of inelastic load reversals and large deformations.

A layered triangular finite element taking account of the coupling effect between the membrane action and the bending action is developed. A tangent stiffness iterative method incorporated with incremental loading procedure is used for the nonlinear analysis.

Finally a series of numerical examples including beams, slabs and shells are presented. Validity of the method is studied by comparing the analytical results with experimental data. Effects of various important parameters are also discussed.

2. MATERIAL PROPERTIES AND CONSTITUTIVE RELATIONS

2.1 Introduction

Reinforced concrete is a composite material consisting of steel reinforcement and concrete. The properties of steel reinforcement are generally well defined. However, those for concrete are more difficult to define because it is a heterogeneous material composed of mortar and aggregate. Nevertheless for purposes of analysis, concrete is generally considered as homogeneous in a macroscopic sense. It is the intrinsic heterogeneity which makes the determination of the constitutive relation of concrete a formidable task. Because of the complexity of analyzing shells themselves, in this study the nonlinear material model will be made very simple but yet capable of capturing the dominant behavior of the reinforced concrete material.

Most reinforced concrete slab or shell structures experience cyclic loading or load reversal in their lives. Wind load, traffic load and seismic load are among the most common loads encountered by the structures. The unloading behavior of concrete in the inelastic or cracked range is very difficult to define. The scope of the present investigation is restricted to the case of monotonically increasing loads, but an ultimate goal of future studies should also include cyclic loading. Under monotonical loading it is quite unlikely that significant unloading (strain decreasing)

will ever occur, so the change of material states due to unloading is ignored in this study. Those cases with significant unloading should be included in the cyclic loading or load reversal cases.

The short-time nonlinear behavior of reinforced concrete structures are mainly attributed to the nonlinear stress-strain relationship, cracking and crushing of concrete, and the bond slip between the reinforcement and the concrete. The direct effect of bond slip will not be considered in this study.

As will be seen in the subsequent discussion, the material properties of concrete and steel will depend on the stress or strain state of the material. In order to account for the varied material properties within a finite element, the element is divided into imaginary concrete layers and steel layers (Fig. 2.1). Each layer may have different material properties corresponding to its stress or strain state. Besides, in accordance with the Kirchhoff's hypotheses the transverse normal stress is neglected, thus any point in the element may be considered to be in a state of plane stress. Therefore only the plane stress constitutive relations need to be developed for the layer system.

2.2 Concrete

2.2.1 Stress-Strain Relationship

A typical uniaxial stress-strain relation for concrete is shown in Fig. 2.2. On the tension side, the

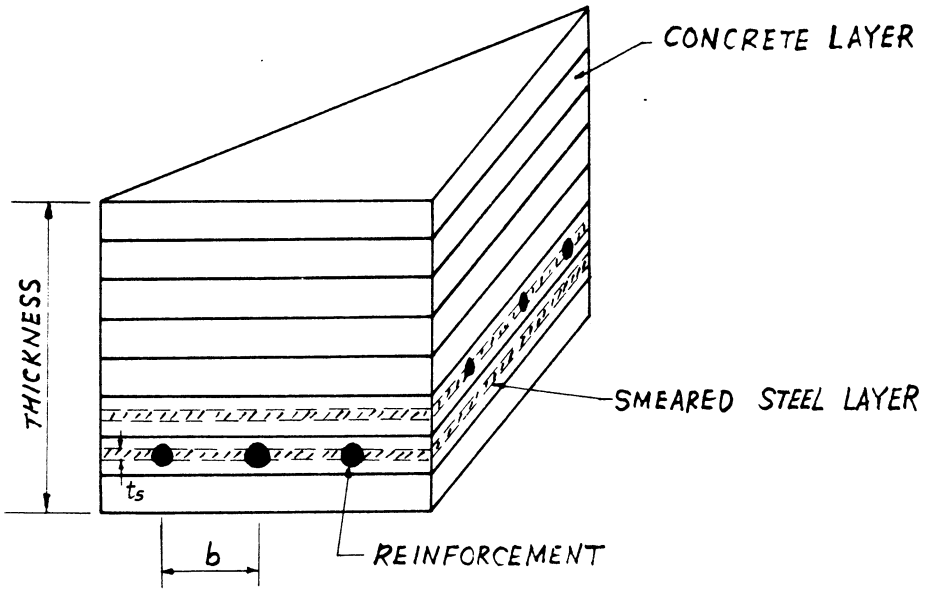

FIG. 2.1 LAYER SYSTEM

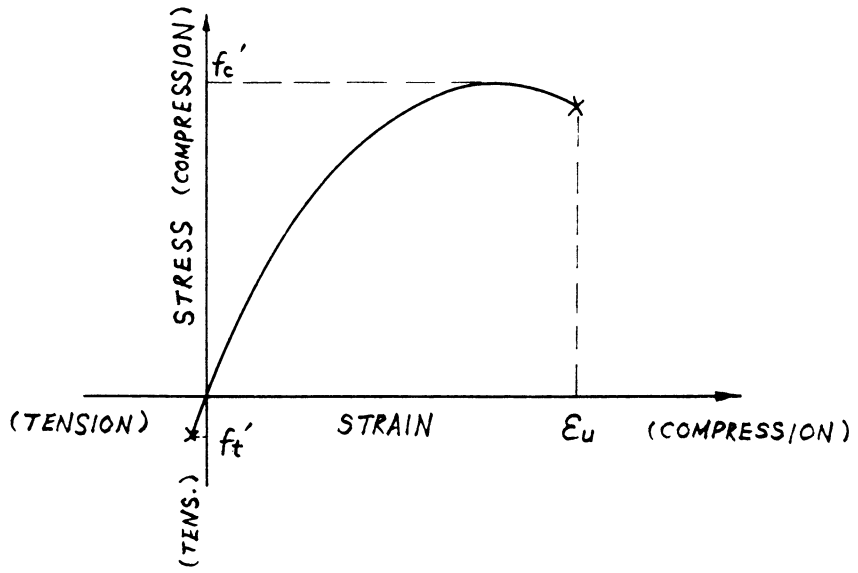

FIG. 2.2 UNIAXIAL STRESS-STRAIN RELATION FOR CONCRETE

curve is nearly linear up to the tensile strength where the concrete cracks and the stress drops to zero. On the compression side, the curve starts out with a nearly linear portion that stretches to about 30% of the ultimate stress, then deviates gradually from the straight line till the slope becomes zero and reaches the ultimate stress. A descending tail follows the peak and finally ends with a complete crushing. The departure of the curve from linearity can be attributed mainly to the development of internal microcracking at the interfaces between the cement paste and the aggregate. The theory of internal microcracking [2.1, 2.2, 2.3] can give only a qualitative description of the stress-strain relationship. For the quantitative description many empirical formulas are available, but each has its own limit of validity and degree of approximation. Fig. 2.3 compares several of the formulas in non-dimensional form. It can be seen that the curvature of the various diagrams may differ considerably. In general, the selection of a formula or the determination of parameters for a formula can be done by curve fitting, so that the diagram fits well a given series of experimental results. All of these formulas are only applicable to the case of uniaxial stress state. An extensive review on the subject was presented in a state of the art report by Popovics [2.7].

For the stress-strain relations under biaxial compression a typical experimental result is shown in Fig. 2.4. Like

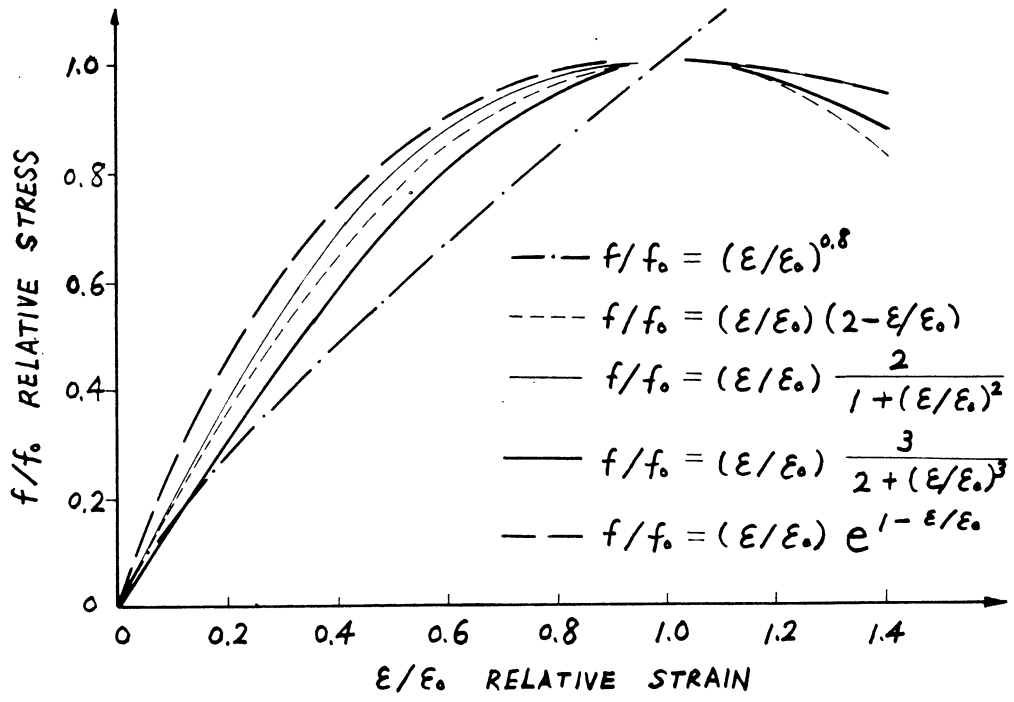

FIG. 2.3 COMPARISON OF SEVERAL FORMULAS FOR STRESS-STRAIN DIAGRAM OF CONCRETE

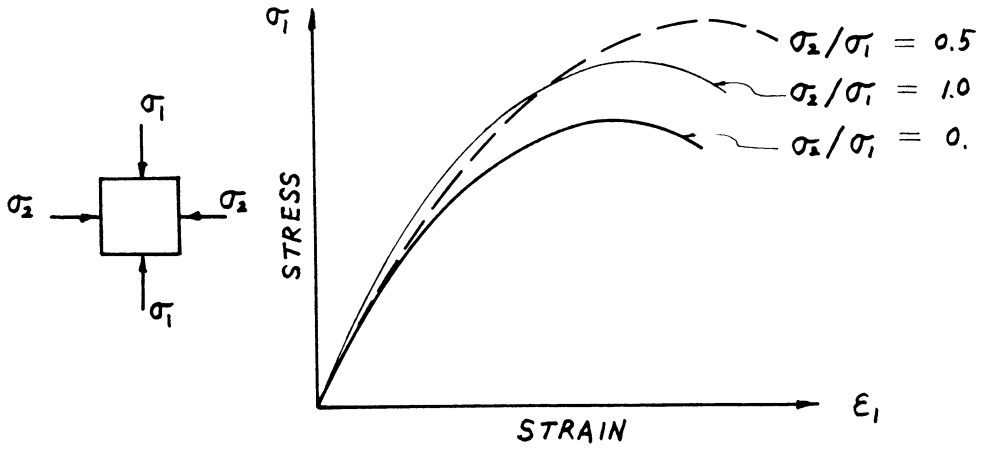

FIG. 2.4 STRESS-STRAIN RELATIONSHIPS OF CONCRETE UNDER BIAXIAL COMPRESSION

an ordinary elastic, homogeneous and isotropic material, the stiffness of the concrete in one of the principal directions increases in the presence of the compressive stress in the perpendicular direction. The increase of stiffness, however, is considerably greater than can be explained by the Poisson's effect alone. According to the microcracking theory the increase of stiffness is mainly due to the confinement of potential microcracking in the presence of biaxial stresses. The test data reported by various investigators deviate from each other considerably. Kupfer et al. [2.8] pointed out that these discrepancies often can be traced back to unintended differences in the stress states developed in the test specimen.

Recently an analytical form for the stress-strain relationship of concrete in biaxial compression has been proposed by Liu et al [2.13]. The expression takes the following form.

$$\sigma = \frac{\epsilon E}{(1-\nu\alpha)(1+C\epsilon+D\epsilon^2)} ,$$

where α = ratio of the principal stress in the orthogonal direction to the principal stress in the direction considered, E = initial tangent modulus in uniaxial loading, ν = Poisson's ratio in uniaxial loading. C and D are functions of α, σ_p and ϵ_p. σ_p and ϵ_p are peak stress in biaxial compression and the strain at peak stress, respectively. The equation provides good agreement between experimental and analytical plots for the ascending portion of the stress-strain curve

(Fig. 2.5). Taylor et al [2.14] also proposed a highly elaborate multilinear biaxial constitutive model for concrete, and applied the model to axisymmetric and planar structures. In the model the principal stress or strain space is divided into regions of equal damage, each of which possesses particular values of modulus of elasticity and Poisson's ratio. The complete construction of the model further involves a series of ad hoc assumptions. Verification of the model with experimental data is still lacking. Most of those ad hoc assumptions have to be verified as a whole, rather than individually, by comparing the over-all results with experimental data. The difficulty will increase rapidly with the number of assumptions. Moreover an elaborate model often requires more computation. A true assessment of the model should consider both the improvement of solution and the increase of computational effort.

However, it is believed that the over-all nonlinear behavior of a reinforced concrete system is dominated by the tensile cracking of the concrete. Therefore it is concluded that the adoption of an elaborate hypothetical stress-strain law is not warranted at this time. In this study the concrete is idealized to be elastic-plastic in biaxial compression, and linear elastic in biaxial tension and tension-compression (Fig. 2.6).

2.2.2 Failure Criteria

Figure 2.7 shows a failure envelop of concrete under biaxial stress loading obtained by Kupfer et al [2.8].

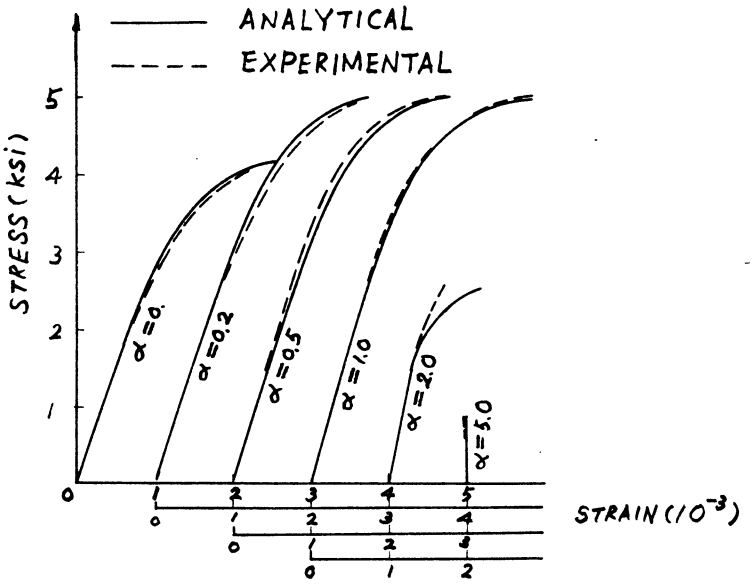

FIG. 2.5 COMPARISON OF LIU'S MODEL WITH EXPERIMENTAL DATA

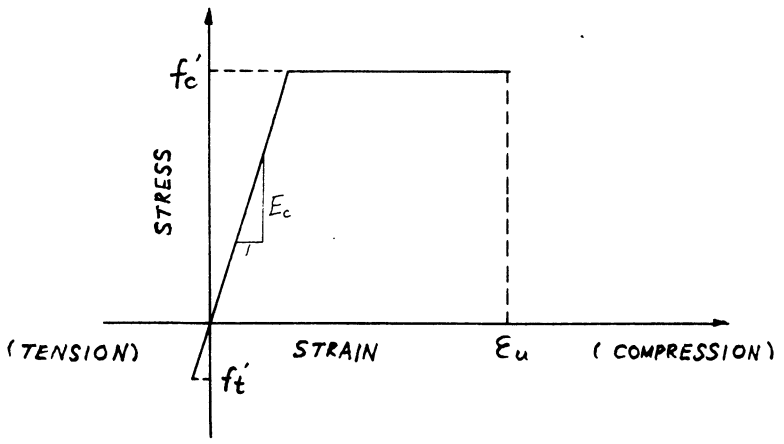

FIG. 2.6 IDEALIZED UNIAXIAL STRESS-STRAIN RELATION FOR CONCRETE

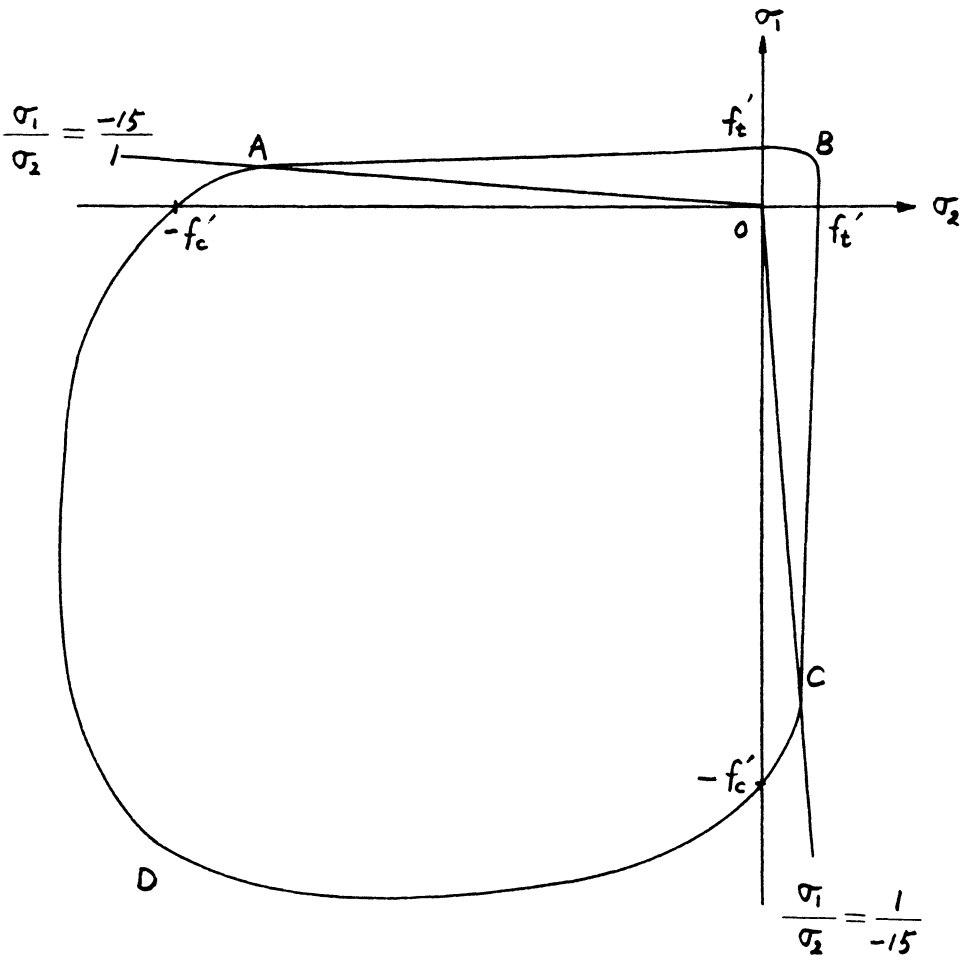

FIG. 2.7 FAILURE SURFACE OF CONCRETE OBTAINED BY KUPFER ET AL.

An examination of the crack patterns in the specimen after failure reveals that the failure can be classified into two distinct modes - cracking and yielding. In Fig. 2.7 OA and OC are radial lines with σ_1/σ_2 equal to -15/1 and 1/-15 respectively. Envelopes ABC and ADC represent the cracking failure envelope and yielding failure envelope respectively. Tests by Kupfer et al [2.8] have shown that if the stress state of concrete reaches envelope ABC, a single cleavage perpendicular to the maximum tensile stress and the free plane of the specimen is formed (Fig. 2.8a). On the other hand, if the stress state reaches envelop ADC, numerous microcracks parallel to the free surfaces of the specimen are formed, but the specimen can still undergo some apparent plastic deformation before it collapses completely. At failure additional major cracks develop with various angles to the free surfaces of the specimen (Fig. 2.8b).

For simplicity, in this investigation von Mises yield criterion is used to approximate the failure surface in biaxial compression so that the results of the well-established plasticity theory can be utilized. The yield criterion can be expressed as follows (Fig. 2.9)

$$F(\sigma) = \sqrt{\sigma_x^2 - \sigma_x \sigma_y + \sigma_y^2 + 3\tau_{xy}^2} - \bar{\sigma} = 0 \qquad (2.1)$$

where $\bar{\sigma}$ is the uniaxial yield strength, and is assumed to be equal to the uniaxial compressive strength f_c'. In terms of principal stresses, it can also be shown as

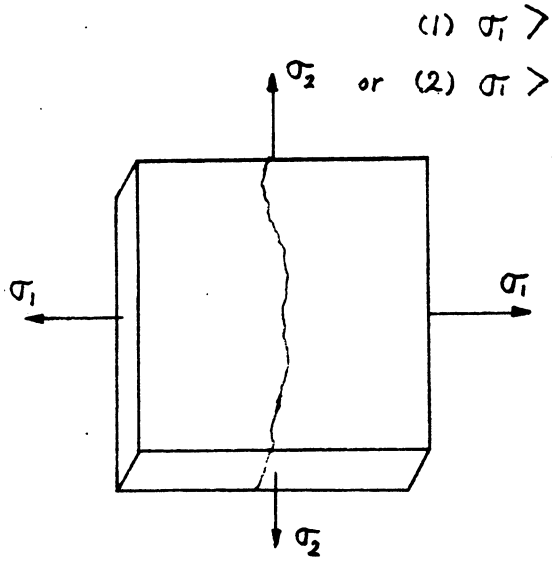

(a) CRACKING FAILURE MODE

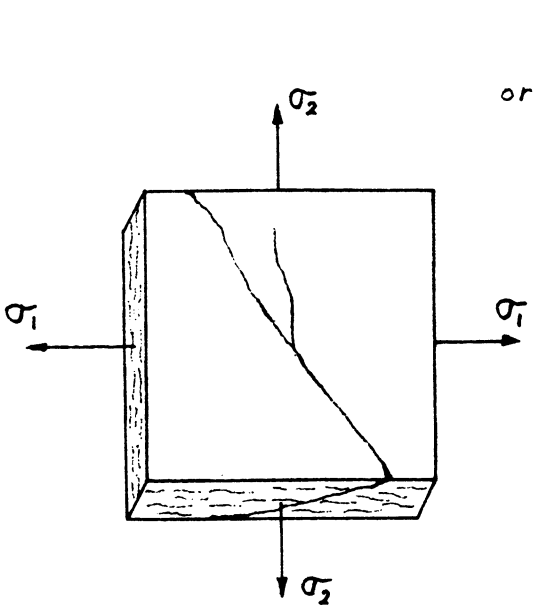

(b) YIELDING FAILURE MODE

FIG. 2.8 FAILURE MODES OF CONCRETE

$$F(\sigma) = \sqrt{\sigma_1^2 - \sigma_1\sigma_2 + \sigma_2^2} - \bar{\sigma} = 0 \qquad (2.2)$$

The apparent plastic yielding of the concrete is not connected with actual plastic flow of cement gel or other components, but rather represents the cumulative effect of microcrack propagation. There is no theory in existence which provides a flow rule governing the post-yielding stress-strain relations for concrete. However, for consistency, the classical normality flow rule is assumed valid for yielded concrete. In addition a crushing surface, analogous to the yield surface but in terms of strains, is postulated to define the complete collapse (or crushing) for the yielded concrete. The crushing surface (Fig. 2.10) is as follows.

$$C(\epsilon) = \sqrt{\epsilon_x^2 - \epsilon_x\epsilon_y + \epsilon_y^2 + \frac{3}{4}\gamma_{xy}^2} - \epsilon_u = 0 \qquad (2.3)$$

$$\text{or} \quad C(\epsilon) = \sqrt{\epsilon_1^2 - \epsilon_1\epsilon_2 + \epsilon_2^2} - \epsilon_u = 0$$

where ϵ_u is the ultimate strain in the uniaxial compression test.

Experimental results consistently show that the strength of concrete under biaxial tension is almost independent of the stress ratio σ_1/σ_2 and equal to the uniaxial tensile strength. The maximum stress failure theory is adopted in this investigation for biaxial tensile stress state. The concrete is assumed to crack when either of the principal

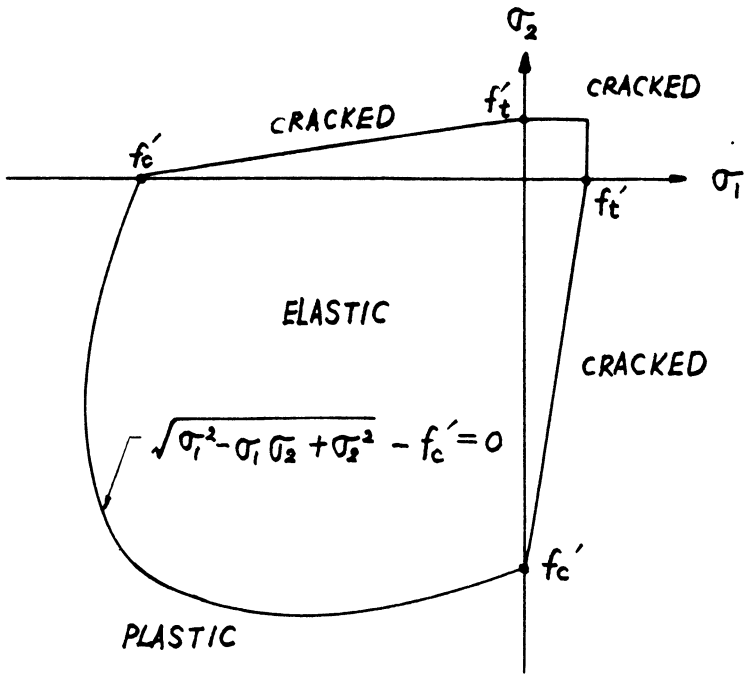

FIG. 2.9 ASSUMED FAILURE SURFACE FOR CONCRETE

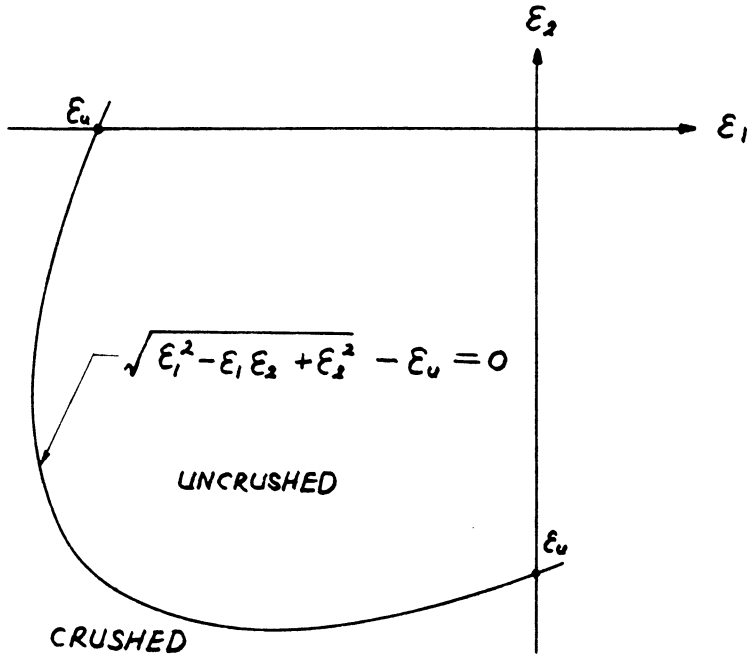

FIG. 2.10 ASSUMED CRUSH SURFACE FOR CONCRETE

stresses exceeds the uniaxial tensile strength f_t' (Fig. 2.9). For the tension-compression stress state, a straight line connecting f_c' and f_t' in Fig. 2.9 is used to approximate the true failure surface, and the failure mode is assumed to be cracked.

2.2.3 Uncracked Elastic Stiffness

In the elastic region (Fig. 2.9), the concrete is assumed to be isotropic, homogeneous, linearly elastic. Thus the stress-strain relations are

$$\begin{Bmatrix} \sigma_x \\ \sigma_y \\ \tau_{xy} \end{Bmatrix} = \frac{E}{1-\nu^2} \begin{bmatrix} 1 & \nu & 0 \\ \nu & 1 & 0 \\ 0 & 0 & \frac{1-\nu}{2} \end{bmatrix} \begin{Bmatrix} \epsilon_x \\ \epsilon_y \\ \gamma_{xy} \end{Bmatrix} \qquad (2.4)$$

where E is modulus of elasticity, and ν is Poisson's ratio.

2.2.4 Cracked Stiffness

When any of the principal stresses exceeds the tensile strength, cracks will occur in a direction perpendicular to that principal stress. The normal stresses at the cracks drop to zero. The shear modulus is also reduced by cracking. The effects of dowel action and aggregate interlock tend to complicate the determination of an effective value for the shear modulus. In this study, a cracked shear constant is introduced to estimate the effective shear modulus including dowel action and aggregate interlock.

Let the coordinate axes x', y' be parallel and perpendicular respectively to the cracks (Fig. 2.11), then the stress-strain relations referring to $x'y'$ coordinate system are .

$$\begin{Bmatrix} \sigma_x \\ \sigma_y \\ \tau_{xy} \end{Bmatrix}' = \begin{bmatrix} E & 0 & 0 \\ 0 & 0 & 0 \\ 0 & 0 & \alpha G \end{bmatrix} \begin{Bmatrix} \epsilon_x \\ \epsilon_y \\ \gamma_{xy} \end{Bmatrix}', \quad \text{or } \{\sigma'\} = [D']\{\epsilon'\} \tag{2.5}$$

where $G = \frac{E}{2(1+\nu)}$ is the uncracked shear modulus, α is the cracked shear constant.

Note that the strain vector transforms in the following manner:

$$\begin{Bmatrix} \epsilon_x \\ \epsilon_y \\ \gamma_{xy} \end{Bmatrix}' = \begin{bmatrix} c^2 & s^2 & sc \\ s^2 & c^2 & -sc \\ -2sc & 2sc & c^2-s^2 \end{bmatrix} \begin{Bmatrix} \epsilon_x \\ \epsilon_y \\ \gamma_{xy} \end{Bmatrix}, \quad \text{or } \{\epsilon'\} = [T]\{\epsilon\}, \tag{2.6}$$

where $c = \cos\beta$, $s = \sin\beta$

β = the angle from x axis to x' axis.

The stress vector transforms as follows:

$$\begin{Bmatrix} \sigma_x \\ \sigma_y \\ \tau_{xy} \end{Bmatrix} = \begin{bmatrix} c^2 & s^2 & -2sc \\ s^2 & c^2 & 2sc \\ sc & -sc & c^2-s^2 \end{bmatrix} \begin{Bmatrix} \sigma_x \\ \sigma_y \\ \tau_{xy} \end{Bmatrix}', \quad \text{or } \{\sigma\} = [T]^T\{\sigma'\} \tag{2.7}$$

Eq. (2.5) can be transformed to global xy coordinate system as follows

$$\{\sigma\} = [D]\{\epsilon\} \tag{2.8}$$

and

$$[D] = [T]^T[D][T] \tag{2.9}$$

If both of the principal stresses exceeds the tensile strength, the concrete will crack in both principal directions. The stress-strain relations in $x'y'$ coordinate system are

$$\begin{Bmatrix} \sigma_x' \\ \sigma_y' \\ \tau_{xy}' \end{Bmatrix} = \begin{bmatrix} 0 & 0 & 0 \\ 0 & 0 & 0 \\ 0 & 0 & \alpha G \end{bmatrix} \begin{Bmatrix} \epsilon_x' \\ \epsilon_y' \\ \gamma_{xy}' \end{Bmatrix} \tag{2.10}$$

Eq. (2.9) is still valid for transforming these relations into the global xy coordinate system.

If the concrete cracks in one direction, and the stress parallel to the cracks reaches yield point f_c', then the stress-strain relations can be expressed as follows:

$$\begin{Bmatrix} d\sigma_x' \\ \sigma_y' \\ \tau_{xy}' \end{Bmatrix} = \begin{bmatrix} 0 & 0 & 0 \\ 0 & 0 & 0 \\ 0 & 0 & \alpha G \end{bmatrix} \begin{Bmatrix} d\epsilon_x' \\ \epsilon_y' \\ \gamma_{xy}' \end{Bmatrix} \tag{2.11}$$

Note that in the incremental form, the first equation of (2.11) indicates that the material retains the yield stress while requiring no increase of stress to be further strained.

Cracking in reinforced concrete is complicated by the presence of the reinforcing bars. Fig. 2.12 shows a reinforced concrete element under uniaxial stress. When the concrete reaches the ultimate tensile strength, primary cracks form at finite intervals along the length. The total load is transferred across these cracks by the reinforcement, but

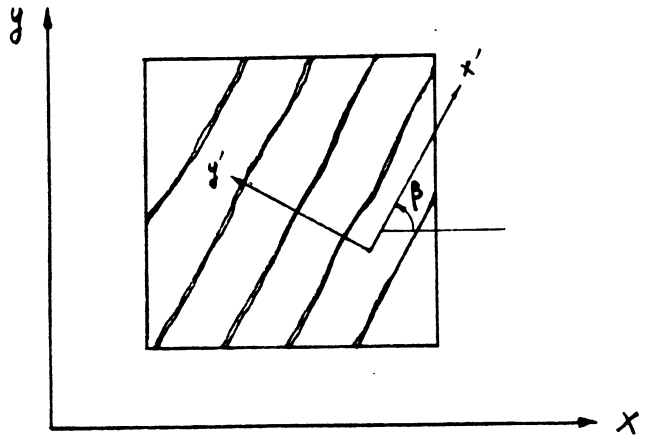

FIG. 2.11 COORDINATE TRANSFORMATION FOR A CRACKED ELEMENT

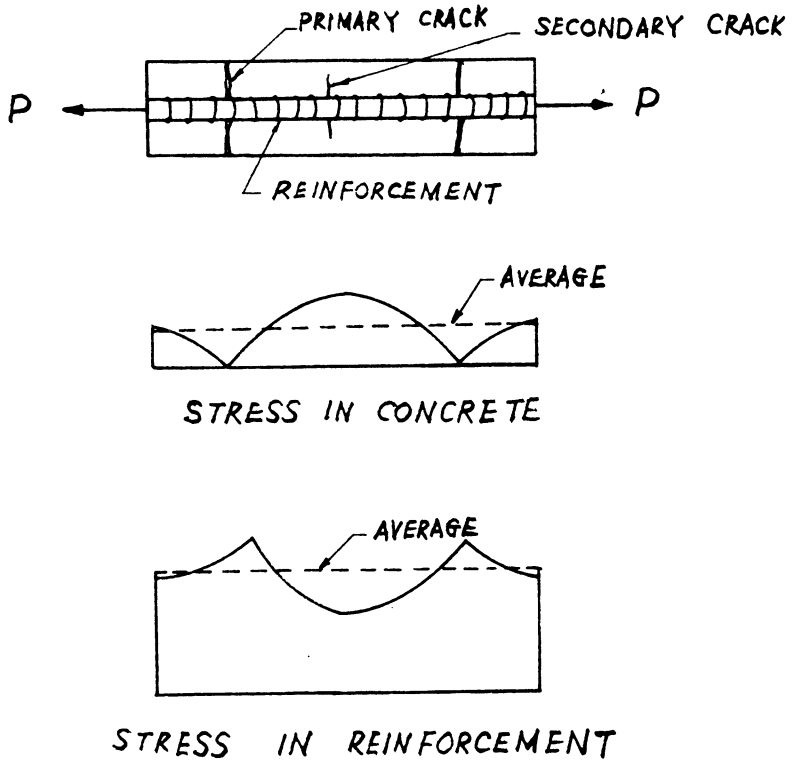

FIG. 2.12 STRESS DISTRIBUTION IN A CRACKED R/C ELEMENT

the concrete between cracks is still capable of carrying stresses because of the bond between steel and concrete. This phenomenon is called the "tension stiffening effect." The concrete stress is zero at the cracks but is not zero if averaged over the length. As the load increases, more cracks form and the amount of tension carried by the concrete progressively decreases. Thus the average concrete stress vs. strain curve for the element may be considered to have an unloading portion (Fig. 2.13). The concept of working with average stress and strain over a relatively long gauge length to account for the tension stiffening effect was first introduced by Scanlon [1.19]. In his work he replaced the average stress-strain curve by a series of straight lines with stepwise decreasing modulus of elasticity (Fig. 2.13). In this investigation, the modulus of the concrete is assumed to be zero once the concrete cracks, but the unbalanced stress is released stepwise gradually according to a specified unloading curve (Fig. 2.14). For instance in Fig. 2.14, the first solution σ_1 exceeds the tensile strength, the concrete cracks, and zero modulus is used for the following solution. σ_{o1} instead of total stress σ_1 is considered as the unbalanced stress. For the second solution σ_{o2} is the unbalanced stress etc.

In the computer program developed for this study, the

unloading curve is specified by inputing pairs of stress and strain values to define a polynomial curve of the form

$$\sigma = a_0 + a_1 \epsilon + a_2 \epsilon^2 + a_3 \epsilon^3$$

An interpolation procedure is used to pass an unloading curve through the given stress-strain points.

It should be noted that the steel stress obtained will also be the average stress in the steel layer. Thus the maximum steel stress is always underestimated. In most cases, however, the cracked concrete will reach the zero-stress stage before the reinforcement reaches the yield point, hence the results should not be significantly affected.

Further note that if the concrete in compression is treated as a strain softening material (Fig. 2.15) the step-wise gradual unloading scheme can also be used to avoid the numerical difficulty caused by using negative moduli. For the sake of simplicity the concrete in compression is treated as a elastic perfectly plastic material in this investigation.

2.2.5 Plastic Stiffness

The associated flow rule of the von Mises yield criterion is also assumed to be valid for the concrete yielding in compression. The normality principal can be expressed as follows.

$$d\{\epsilon\}_p = \lambda \frac{\partial F}{\partial \{\sigma\}} , \qquad (2.12)$$

where $d\{\epsilon\}_p$ denotes the increment of plastic strain,

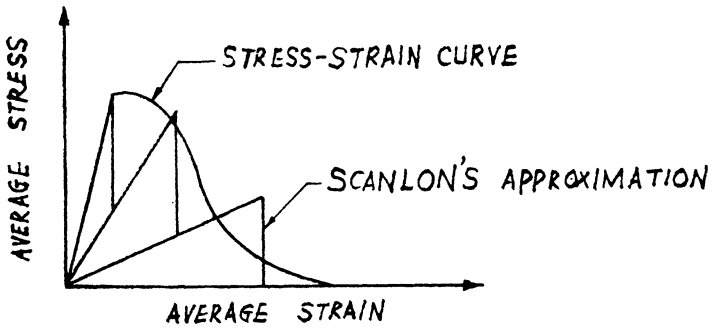

FIG. 2.13 STRESS-STRAIN CURVE FOR CONCRETE IN TENSION

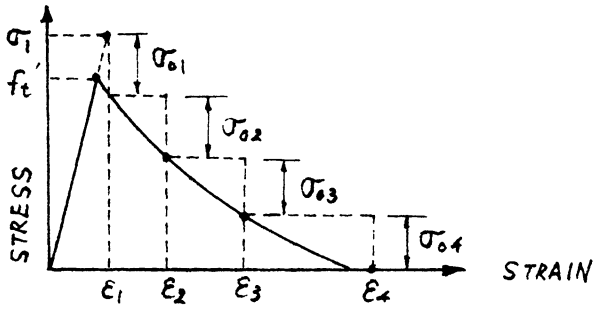

FIG. 2.14 GRADUAL UNLOADING FOR CRACKED CONCRETE

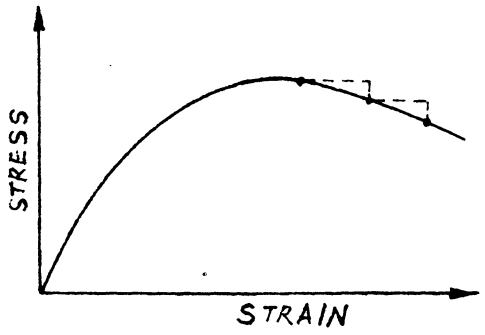

FIG. 2.15 STRAIN SOFTENING STRESS-STRAIN CURVE

λ is a proportional constant, F is the yield function. It is further assumed that during an infinitesimal increment of stress, changes of strain are divisible into elastic and plastic parts, namely

$$d\{\epsilon\} = d\{\epsilon\}_e + d\{\epsilon\}_p \tag{2.13}$$

The elastic strain increments are related to stress increments by the following relation:

$$d\{\epsilon\}_e = [D]^{-1} d\{\sigma\} \quad , \tag{2.14}$$

where [D] is the elasticity matrix. The following incremental stress-strain relationship is obtained following some mathematical manipulation described in detail in References 1.6 and 1.9.

$$d\{\sigma\} = [D]_{ep}\, d\{\epsilon\} \tag{2.15}$$

$$[D]_{ep} = [D] - [D]\left\{\frac{\partial F}{\partial \{\sigma\}}\right\}\left\{\frac{\partial F}{\partial \{\sigma\}}\right\}^T [D] \left[-A + \left\{\frac{\partial F}{\partial \{\sigma\}}\right\}^T [D] \left\{\frac{\partial F}{\partial \{\sigma\}}\right\}\right]^{-1} \tag{2.16}$$

The elasto-plastic matrix $[D]_{ep}$ takes the place of the elasticity matrix [D] in incremental analysis. A is a hardening parameter, equals zero for perfectly plastic material. If the [D] and F given in Sec. 2.2.2 and 2.2.3 are substituted, $[D]_{ep}$ can be expressed explicitly as follows:

$$[D]_{ep} = \frac{E}{Q}\begin{bmatrix} \sigma_y'^2 + \frac{2}{1+\nu}\tau_{xy}^2 & & \text{Sym.} \\ -\sigma_x'\sigma_y' + \frac{2\nu}{1+\nu}\tau_{xy}^2 & \sigma_x'^2 + \frac{2}{1+\nu}\tau_{xy}^2 & \\ -\frac{\sigma_x' + \nu\sigma_y'}{1+\nu}\tau_{xy} & -\frac{\sigma_y' + \nu\sigma_x'}{1+\nu}\tau_{xy} & \frac{R}{2(1+\nu)} \end{bmatrix}, \tag{2.17}$$

where $$R = \sigma_x'^2 + 2\nu\sigma_x'\sigma_y' + \sigma_y'^2$$

$$Q = R + 2(1-\nu)\tau_{xy}^2 ,$$

$$\sigma_x' = \frac{1}{3}(2\sigma_x - \sigma_y) ,$$

$$\sigma_y' = \frac{1}{3}(2\sigma_y - \sigma_x) .$$

The normality flow rule has been proved applicable to many ductile metals. As pointed out earlier, the inelasticity of the concrete is caused not by actual plastic flow, but by the cumulative effect of microcrack propagation. It is questionable whether the normality flow rule is still applicable to concrete. Another question arises naturally as to how important the assumed flow rule is to the overall behavior of a concrete structure as compared to other effects such as cracking, tension stiffening, bond slip and yielding of the reinforcement. The normality flow rule constrains the plastic strain to flow in a direction normal to the yield surface. What would happen if the flow of plastic strain is not constrained but the stress is fixed at the initial yield point on the yield surface? To study this question the following "unconstrained flow rule" will also be used, and the results will be compared with those using the more complex normality flow rule.

$$d\{\sigma\} = [\,0\,]\, d\{\epsilon\} \qquad (2.18)$$

2.2.6 Crushed Stiffness

When the concrete is crushed, it is assumed to lose all its stiffness. Thus, the stress-strain relations are

$$\begin{Bmatrix} \sigma_x \\ \sigma_y \\ \tau_{xy} \end{Bmatrix} = \begin{bmatrix} 0 & 0 & 0 \\ 0 & 0 & 0 \\ 0 & 0 & 0 \end{bmatrix} \begin{Bmatrix} \epsilon_x \\ \epsilon_y \\ \gamma_{xy} \end{Bmatrix} \tag{2.19}$$

2.3 Steel

The crack propagation in reinforced concrete is influenced by local stress concentrations which are in turn influenced by the size and spacing of the reinforcement. In reinforced concrete slabs and shells, unlike beams, reinforcement is usually more uniformly distributed, and reinforcing bars used tend to be smaller in size. The finite element meshes can always be so laid out that the reinforcement is more or less uniformly distributed in each element. In this study, the effects of reinforcement size and spacing will not be considered, and the reinforcement will be assumed to be uniformly distributed over the element. Thus each layer of reinforcement will be replaced by an equivalent smeared distributed steel layer (Fig. 2.1). The equivalent thickness of the layer is

$$t_s = \frac{A_s}{b} = p_s \times d \tag{2.20}$$

where A_s is the area of one reinforcing bar,

b is the spacing of the reinforcing bars,

p_s is the reinforcement ratio,

d is the effective depth of the slab.

The steel is considered as an elastic-plastic material with yield stresses $\pm f_y$ and elastic modulus E_s (Fig. 2.16). It is further assumed that the reinforcing bars carry only uniaxial stress. When the stress in the reinforcement remains in the elastic range, the stress-strain relations referring to the $x'y'$ coordinate system (Fig. 2.17) are

$$\begin{Bmatrix} \sigma_{x'} \\ \sigma_{y'} \\ \tau_{x'y'} \end{Bmatrix} = \begin{bmatrix} E_s & 0 & 0 \\ 0 & 0 & 0 \\ 0 & 0 & 0 \end{bmatrix} \begin{Bmatrix} \epsilon_{x'} \\ \epsilon_{y'} \\ \gamma_{x'y'} \end{Bmatrix} \tag{2.21}$$

Eq. (2.9) may be used to transform the relations to the global coordinate system.

When the reinforcing still has yielded, it is assumed to have zero incremental stiffness, that is

$$d\{\sigma\} = [\,0\,]\, d\{\epsilon\} \tag{2.22}$$

2.4 Composite Layer System

Although the finite element is divided into imaginary concrete and steel layers, the displacement field of the element is still assumed to be continuous. Any volume integration involving the material properties can be carried out layer by layer, namely

$$\int_{vol} \Phi [D]\, dV = \sum_{i=1}^{n_c} \int_{vol} \Phi [D]_{ci}\, dV + \sum_{i=1}^{n_s} \int \Phi [D]_{si}\, dV \tag{2.23}$$

where Φ is an arbitrary function of space,

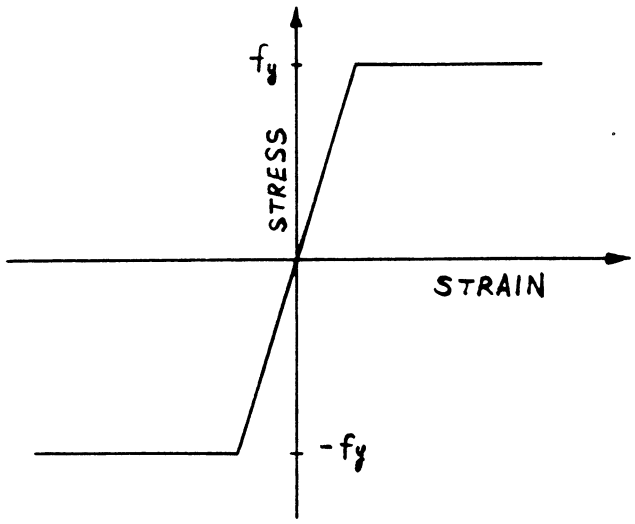

FIG. 2.16 STRESS-STRAIN RELATION FOR STEEL

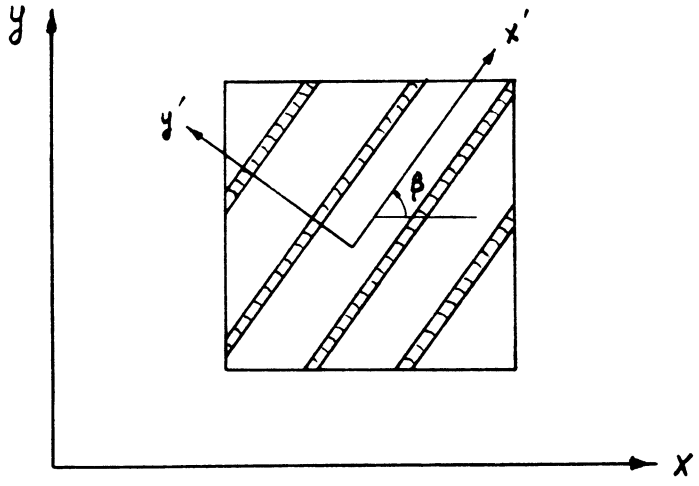

FIG. 2.17 COORDINATE TRANSFORMATION FOR STEEL STIFFNESS

$[D]$ is the material matrix of the element,

$[D]_{ci}$ is the material matrix of the i th concrete layer,

$[D]_{si}$ is the material matrix of the i th steel layer,

n_c is the total number of concrete layers,

n_s is the total number of steel layers.

2.5 Summary

A composite layer system consisting of concrete layers and steel layers is constructed to account for the varied material properties within the finite element. The concrete is assumed to be elasto-plastic in compression and brittle in tension (Fig. 2.6). The von Mises yield surface, a maximum principal stress crack criterion and an effective strain crush criterion are used to define the transition boundaries for different material states (Figs. 2.9, 2.10). The steel is considered as a one-dimensional elasto-plastic material (Fig. 2.16). The tension stiffening effect is accounted for by releasing the unbalanced stress gradually according to a specified unloading curve (Fig. 2.14).

3. FINITE ELEMENT IDEALIZATION

3.1 General Remarks

The finite element method is essentially a discretization procedure through which a continuum with infinite degrees of freedom can be approximated by an assemblage of discrete subregions (or elements) each with a specified finite number of unknowns. The concept was originally introduced by Turner et al. [3.1] in the early 1950s as the result of an attempt to improve the Hrennikoff-McHenry's lattice analogy for the solution of plane stress problems.

Owing to the popularity of the matrix methods in structural mechanics and the accessibility of the high speed digital computers, the method rapidly won widespread acceptance as an effective, powerful and versatile tool in structural mechanics. In attempts to consolidate the mathematical foundation of the method, it was soon recognized as a special form of the classical Rayleigh-Ritz method. It was further realized that the method is a rediscovery of a known mathematical method which appeared in Courant's approximate solution of St. Venant torsion problem in 1943 [3.2].

One of the very basic assumptions in continuum mechanics is that the material is totally continuous. This simplifying assumption means that the molecular structure of matter is to be disregarded, and the material is pictured without gaps or empty spaces. Most engineering materials are formed of either crystals or fibers whose dimensions are extremely

small in comparison with the dimensions of the entire body. Therefore the continuum approach is completely justified for studying the behavior of the material on the average.

Concrete is not a continuum by any standard. Cracks at the interface between coarse aggregate and mortar exist even at unstrained state. These interfacial cracks begin to increase in length, width and number at about 30% of ultimate load. At about 80% of ultimate load, cracks propagate through mortar and form continuous crack patterns. Yet the continuum approach should yield a useful explanation of the average behavior of the concrete, except that the average should be taken over a much larger, finite gauge length.

In the finite element analysis of this study, the displacement field of each element is assumed continuous even after tensile cracks form inside the element. In essence, the cracked concrete is approximated by a continuous medium with equivalent average properties. Therefore the strains or stresses of a concrete or steel layer obtained from the analysis should be interpreted as average values over the whole layer.

3.2 Displacement Formulation

The finite element displacement analysis of an elastic continuum starts with the subdivision of the original system into an assemblage of discrete elements. The displacements $\{f\}$ at any point within the element are approximated by

interpolation functions associated with generalized coordinates r_i which are the nodal point displacements.

$$\{f\} = [N]\{r\}^e = [N_i \; N_j \cdots] \begin{Bmatrix} r_i \\ r_j \\ \vdots \end{Bmatrix} \tag{3.1}$$

where the components of [N] are in general functions of position and $\{r\}^e$ represents a listing of nodal displacements for a particular element.

With displacements known at all points within the element the strains at any point can be determined. These will result in the following relationship:

$$\{\epsilon\} = [B]\{r\}^e \tag{3.2}$$

From the material constitutive law, the stresses

$$\{\sigma\} = [D](\{\epsilon\} - \{\epsilon_o\}) + \{\sigma_o\} \tag{3.3}$$

where [D] is an elasticity matrix containing the appropriate material properties, $\{\epsilon_o\}$ is the initial strain vector, $\{\sigma_o\}$ the initial stress vector.

Applying the virtual work principle or the theorem of minimum potential energy to the total structure as an assemblage of all elements, the following equilibrium equation will be obtained:

$$[K]\{r\} + \{F\}_p + \{F\}_g + \{F\}_{\epsilon_o} + \{F\}_{\sigma_o} - \{R\} = 0 \;, \tag{3.4}$$

where the stiffness matrix

$$[K] = \sum_e \int [B]^T [D][B] \, d(vol.) \;, \tag{3.5}$$

the nodal forces due to body forces

$$\{F\}_p = -\sum_e \int [N]^T \{p\}\, d(\text{vol.}) \quad , \tag{3.6}$$

the nodal forces due to surface forces

$$\{F\}_g = -\sum_e \int [N]^T \{g\}\, d(\text{area}) \quad , \tag{3.7}$$

the nodal forces due to initial strains

$$\{F\}_{\epsilon_0} = -\sum_e \int [B]^T [D] \{\epsilon_0\}\, d(\text{vol}) \quad , \tag{3.8}$$

those due to initial stresses

$$\{F\}_{\sigma_0} = -\sum_e \int [B]^T \{\sigma_0\}\, d(\text{vol.}) \tag{3.9}$$

$\{r\}$ is the vector of all nodal displacements, $\{R\}$ the applied nodal forces, $\{p\}$ the body force vector, $\{g\}$ the surface force vector. The summation notation $\sum_e$ means summation over all elements. In practical computation this is achieved by the well-known direct stiffness method. The stiffness matrix or the force vector for each element is generated sequentially and the summation is carried out by direct addition of the element matrices or vectors to the proper places in the assembled structure matrices or vectors.

The nodal displacements $\{r\}$ can be obtained by solving the system of simultaneous algebraic equations (3.4). The strains and stresses at any point of the element can be determined by the relations in Eqs. (3.2) and (3.3).

3.3 Application to Shell Structures

The finite element analysis of shell structures requires the division of the shell surface into a system of subregions. The surface geometry of each subregion must be idealized by an approximation of its actual curvatures. The simplest approximation is that the elements are flat surfaces or an assemblage of flat surfaces. If the material properties are symmetrical with respect to the middle plane, this approximation will decouple the membrane and the bending actions at the element level. Note that the coupling of these actions will develop once these flat elements are assembled into an approximation of the curved shell surface. If the material properties are not symmetrical or if the individual elements are curved rather than flat, there will be membrane-bending coupling at the element level. In general it is very difficult to define the stiffness properties and to include the rigid body displacement modes for curved elements. Flat elements are more widely used in general shell programs at the present time, and will also be used in this work. The approximation of a typical shell surface by flat triangular elements is shown in Fig. 3.1. The size and shape of the triangles are defined by the coordinates of the nodal points lying on the reference surface of the shell.

If the shell is to be treated as a two-dimensional surface rather than a three-dimensional solid, some kinematic

assumptions have to be adopted. In this investigation, the classical Kirchhoff's hypotheses are adopted. The assumptions may be stated as follows.

(1) The straight fibres of a plate which are perpendicular to the reference surface before deformation remain so after deformation and do not change their length.

(2) The normal stresses acting on planes parallel to the reference surface may be neglected in comparison with the other stresses.

It should be noted that the first assumption results in plane strain constitutive relations, whereas the second assumption yields plane stress condition. This inconsistency can be avoided by assuming that the material is approximated by one with a special type of orthotropy wherein

$$\frac{1}{E_n} = \frac{1}{G_{1n}} = \frac{1}{G_{2n}} = \nu_{1n} = \nu_{2n} = 0$$

where E is the modulus of elasticity, G the shear rigidity, ν the Poisson's ratio; subscripts n indicate the normal direction, 1 and 2 indicate two perpendicular direction on the reference surface (Fig. 3.2).

The Kirchhoff's assumptions enable the displacements at any point of the shell to be described in terms of the displacements and their derivatives on the reference surface. Thus,

$$\begin{aligned} w &= w_0(x, y) \\ u &= u_0(x, y) - z\frac{\partial w}{\partial x} \\ v &= v_0(x, y) - z\frac{\partial w}{\partial y} \end{aligned} \qquad (3.10)$$

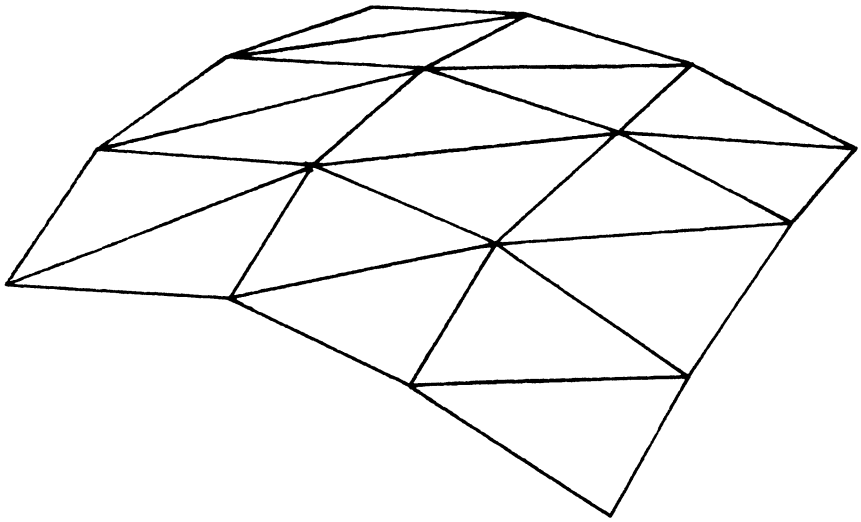

FIG. 3.1 DISCRETIZED SHELL SURFACE

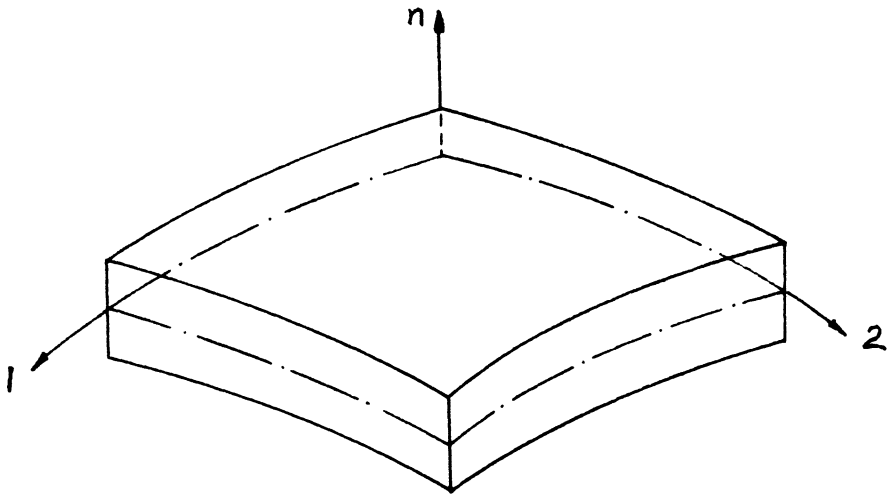

FIG. 3.2 DIFFERENTIAL ELEMENT OF A SHELL

where u, v, w are displacements in x, y, z directions respectively, referring to Fig. 3.3, and letting subscripts "o" indicate the values on the reference surface. Assuming the shape functions for W_o, U_o, V_o gives,

$$w_o = \Psi(x,y) \begin{Bmatrix} w \\ \theta_x \\ \theta_y \end{Bmatrix}^e ,$$

$$u_o = \phi(x,y) \{u\}^e , \tag{3.11}$$

$$v_o = \phi(x,y) \{v\}^e ,$$

where $\theta_x = \frac{\partial w}{\partial y}$, $\theta_y = -\frac{\partial w}{\partial x}$

and the vectors with superscript "e" denote the nodal displacements.

Differentiation of Eq. (3.10) gives

$$\{\epsilon\} = \begin{Bmatrix} \frac{\partial u}{\partial x} \\ \frac{\partial v}{\partial y} \\ \frac{\partial u}{\partial y} + \frac{\partial v}{\partial x} \end{Bmatrix} = \begin{Bmatrix} \frac{\partial u_o}{\partial x} \\ \frac{\partial v_o}{\partial y} \\ \frac{\partial u_o}{\partial y} + \frac{\partial v_o}{\partial x} \end{Bmatrix} - z \begin{Bmatrix} \frac{\partial^2 w}{\partial x^2} \\ \frac{\partial^2 w}{\partial y^2} \\ 2\frac{\partial^2 w}{\partial x \partial y} \end{Bmatrix} \tag{3.12}$$

$$\text{or} \quad \{\epsilon\} = \{\epsilon_o\} - z\{\kappa\}$$

Differentiation of Eq. (3.11) with the usual comma notation yields

$$\{\epsilon_o\} = \begin{bmatrix} \phi_{,x} & 0 \\ 0 & \phi_{,y} \\ \phi_{,y} & \phi_{,x} \end{bmatrix} \begin{Bmatrix} u \\ v \end{Bmatrix}^e = [B_m] \begin{Bmatrix} u \\ v \end{Bmatrix}^e \tag{3.13}$$

$$\{\kappa\} = \begin{bmatrix} \Psi_{,xx} \\ \Psi_{,yy} \\ 2\Psi_{,xy} \end{bmatrix} \begin{Bmatrix} w \\ \theta_x \\ \theta_y \end{Bmatrix}^e = [B_b] \begin{Bmatrix} w \\ \theta_x \\ \theta_y \end{Bmatrix}^e \tag{3.14}$$

Substituting Eqs. (3.13) and (3.14) into (3.12) gives:

$$\{\epsilon\} = \left[-z B_b \;\vdots\; B_m\right] \begin{Bmatrix} w \\ \theta_x \\ \theta_y \\ \hdashline u \\ v \end{Bmatrix}^e = [B]\{\delta\}^e \tag{3.15}$$

From Eq. (3.5) we obtain the element stiffness

$$[K] = \int_{vol} [B]^T [D][B]\, dV = \int_{vol} \left[\begin{array}{c|c} z^2 B_b^T D B_b & -z B_b^T D B_m \\ \hline -z B_m^T D B_b & B_m^T D B_m \end{array}\right] dV$$

$$= \left[\begin{array}{c|c} K_{bb} & K_{bm} \\ \hline K_{mb} & K_{mm} \end{array}\right] \tag{3.16}$$

where $$[K_{bb}] = \int z^2 [B_b]^T [D][B_b]\, dV = \iint [B_b]^T \left[\int z^2 D\, dz\right][B_b]\, dx\, dy \quad , \tag{3.17}$$

$$[K_{bm}] = \iint [B_b]^T \left[-\int z D\, dz\right][B_m]\, dx\, dy = [K_{mb}]^T \tag{3.18}$$

$$[K_{mm}] = \iint [B_m]^T \left[\int D\, dz\right][B_m]\, dx\, dy \tag{3.19}$$

note that B_b and B_m are functions of x, y only.

K_{bb}, K_{bm} and K_{mm} are the bending stiffness, coupling stiffness and membrane stiffness respectively. If the material properties are symmetrical with respect to the middle plane, the term $\int z D dz$ becomes zero, and thus so does K_{bm}. Physically, this is the case wherein the bending and membrane stiffness properties are uncoupled. The nodal forces due to initial stresses can also be found by substituting into Eq. (3.9).

$$\{F\}_{\sigma_0} = \int [B]^T \{\sigma_0\}\, dV = \iint \left[\begin{array}{c} B_b^T \left(-\int z \sigma_0\, dz\right) \\ \hline B_m^T \left(\int \sigma_0\, dz\right) \end{array}\right] dx\, dy \tag{3.20}$$

3.4 Layered Discretization

3.4.1 Evaluation of the Element Stiffness

As pointed out in Chapter 2, any integration involving material properties can be integrated layer by layer. Let c and s denote the number of concrete layers and steel layers respectively for a typical layered finite element shown in Fig. 3.4. Assuming the material properties are constant within each layer, the inner integrations of Eqs. (3.17) to (3.19) can be carried out as follows.

$$[D_{bb}] = \int z^2 [D]\, dz = \sum_{i=1}^{c} \int_{z_i}^{z_{i+1}} z^2 [D_c]_i\, dz + \sum_{i=1}^{s} z_i^2 [D_s]_i t_i$$

$$= \sum_{i=1}^{c} \frac{1}{3}(z_{i+1}^3 - z_i^3)[D_c]_i + \sum_{i=1}^{s} z_i^2 [D_s]_i t_i \qquad (3.21)$$

$$[D_{bm}] = [D_{mb}]^T = -\int z [D]\, dz$$

$$= -\sum_{i=1}^{c} \frac{1}{2}(z_{i+1}^2 - z_i^2)[D_c]_i - \sum_{i=1}^{s} z_i [D_s]_i t_i \qquad (3.22)$$

$$[D_{mm}] = \sum_{i=1}^{c} (z_{i+1} - z_i)[D_c]_i + \sum_{i=1}^{s} [D_s]_i t_i \qquad (3.23)$$

where $[D_c]_i$ is the material matrix of the i th concrete layer,

$[D_s]_i$ is the material matrix of the i th steel layer.

Thus the stiffnesses become

$$[K_{bb}] = \iint [B_b]^T [D_{bb}] [B_b]\, dx\, dy \qquad (3.24)$$

$$[K_{bm}] = \iint [B_b]^T [D_{bm}] [B_m]\, dx\, dy \qquad (3.25)$$

$$[K_{mm}] = \iint [B_m]^T [D_{mm}] [B_m]\, dx\, dy \qquad (3.26)$$

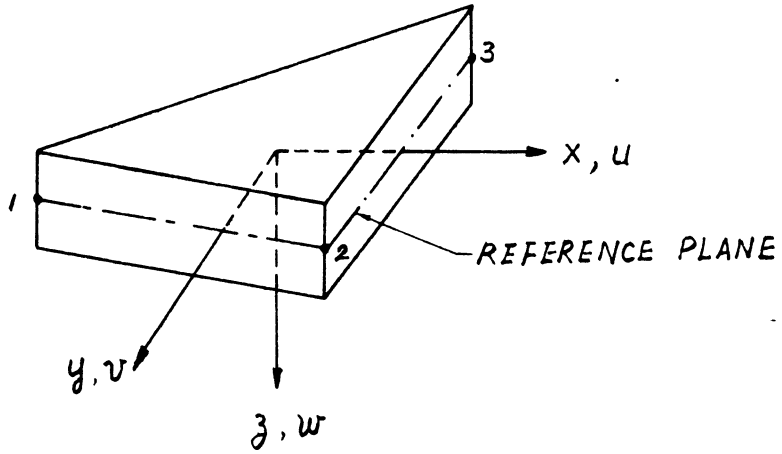

FIG. 3.3 COORDINATE SYSTEM IN A SHELL ELEMENT

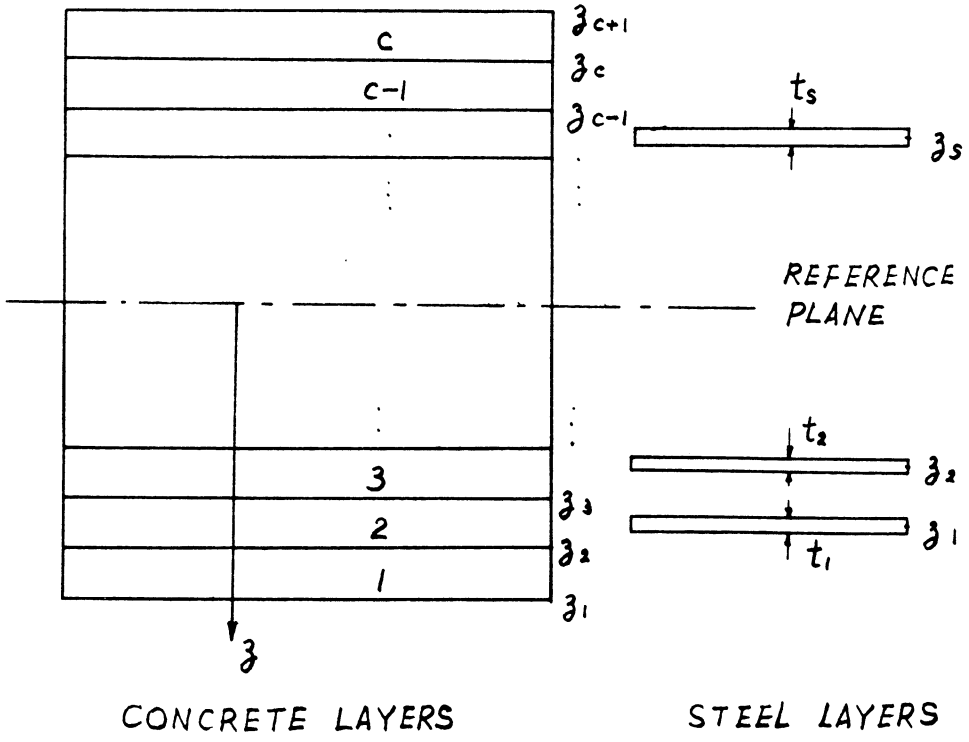

FIG. 3.4 CONSTRUCTION OF A TYPICAL LAYER SYSTEM

3.4.2 Evaluation of the Layer Strains and Stresses

Once the nodal displacements are known, the membrane strains on the reference plane $\{\epsilon_o\}$ and the curvatures $\{\chi\}$ can be obtained by Eqs. (3.13) and (3.14). The strains at the centers of layers can be computed from Eq. (3.12).

$$\{\epsilon_c\}_i = \{\epsilon_o\} - \frac{1}{2}(z_{i+1} + z_i)\{\chi\} \tag{3.27}$$

$$\{\epsilon_s\}_i = \{\epsilon_o\} - z_i\{\chi\} \tag{3.28}$$

The layer stresses are computed as follows.

$$\{\sigma_c\}_i = [D_c]_i \{\epsilon_c\}_i \tag{3.29}$$

$$\{\sigma_s\}_i = [D_s]_i \{\epsilon_s\}_i \tag{3.30}$$

where $\{\epsilon_c\}_i$ and $\{\sigma_c\}_i$ denote the stresses and strains at the center of the i th concrete layer; $\{\epsilon_s\}_i$ and $\{\sigma_s\}_i$ denote those at the center of the i th steel layer.

3.4.3 Evaluation of the Unbalanced Nodal Forces

In all structural analyses, aim is taken to find solutions which simultaneously satisfy continuity, equilibrium and constitutive relationship. For nonlinear problems, procedures are often devised to obtain trial solutions, satisfying one or two of the three conditions, and then corrections are successively made until the remaining conditions are also satisfied. In the numerical method adopted in this study, the nonlinear constitutive relationship will be satisfied by successive corrections. For each iteration, assuming

material properties constant a set of solutions $\{r_2\}$, $\{\varepsilon_2\}$ and $\{\sigma_2'\}$ are obtained (Fig. 3.5). In order to satisfy constitutive relations corrective stresses $\{\sigma_o\}$ are introduced to bring $\{\sigma_2'\}$ to the true stresses $\{\sigma_2\}$ corresponding to $\{\varepsilon_2\}$. $\{r_2\}$, $\{\varepsilon_2\}$ and $\{\sigma_2\}$ are chosen as the corrected set of solutions, and $\{\sigma_o\}$ are considered the stresses which do not satisfy equilibrium. The unbalanced stresses $\{\sigma_o\}$ can be transformed into nodal forces by Eq. (3.20) treating them as the initial stresses. The inner integrations are computed as follows.

$$\{\sigma_{ob}\} = -\int z\{\sigma_o\}\,dz = -\sum_{i=1}^{c} \frac{1}{2}(z_{i+1}^2 - z_i^2)\{\sigma_o\}_i - \sum_{i=1}^{s} z_i\{\sigma_o\}_i t_i \qquad (3.31)$$

$$\{\sigma_{om}\} = \int \{\sigma_o\}\,dz = \sum_{i=1}^{c} (z_{i+1} - z_i)\{\sigma_o\}_i + \sum_{i=1}^{s} \{\sigma_o\}_i t_i \qquad (3.32)$$

The unbalanced nodal forces become

$$\{F\}_{\sigma_o} = \begin{Bmatrix} \iint B_b^T \{\sigma_{ob}\}\,dx\,dy \\ \hline \iint B_m^T \{\sigma_{om}\}\,dx\,dy \end{Bmatrix} \qquad (3.33)$$

Computation of $\{\sigma_o\}$ will be discussed in detail in Section 4.4.

3.5 Selection of Elements

The intrinsic adaptability of the triangular geometry to the free-form shell surface and an arbitrary boundary geometry make it a desirable choice for the element shape for this study. The flat triangular element used here is

one with 15 degrees of freedom, 5 at each corner node, satisfying full compatibility, along inter-element boundaries when adjacent elements are on one plane. The element derives from incorporating a linear curvature triangular bending element (LCCT9) with a constant strain triangular membrane element (CST).

The triangular bending element was originally developed by Clough and Tocher [3.3], and reformulated by Felippa using triangular coordinates instead of Cartesian ones [3.4]. The element is divided into three subtriangles, as shown in Fig. 3.6 in which the internal point "0" is the centroid of the element area. Interpolation functions for the transverse displacement w are assumed independently with cubic variations for each subtriangle. However, slope compatibility along the internal common edges of the subtriangles is imposed. Thus the displacement field has a continuous first derivative over the whole element, and linearly varying curvature within each subelement. The end result is a compatible triangular bending element with 9 degrees of freedom, including transverse displacements and rotations about X and Y axes at three corner nodes.

The constant strain triangular membrane element possesses 6 degrees of freedom, translations in X and Y directions at three corner nodes (Fig. 3.7). The incorporation of LCCT9 and CST provides a good representation of the bending deformation, but poor approximation of the membrane deformation.

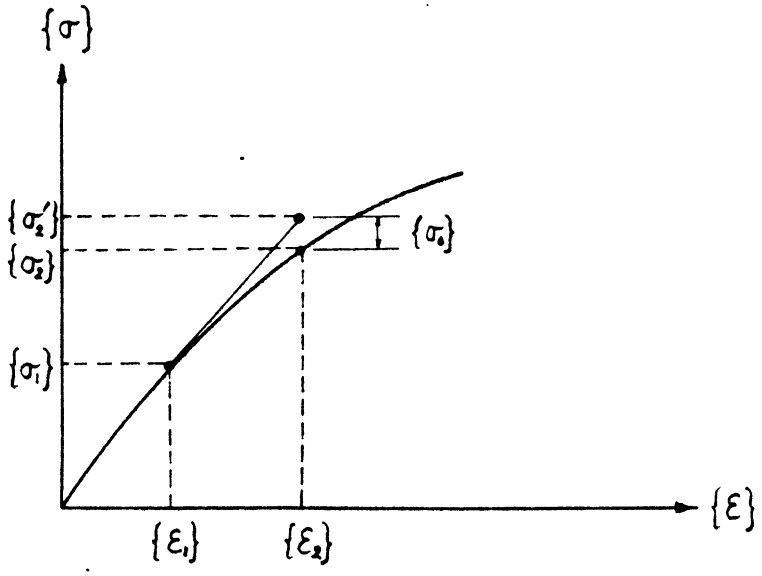

FIG. 3.5 UNBALANCED STRESSES

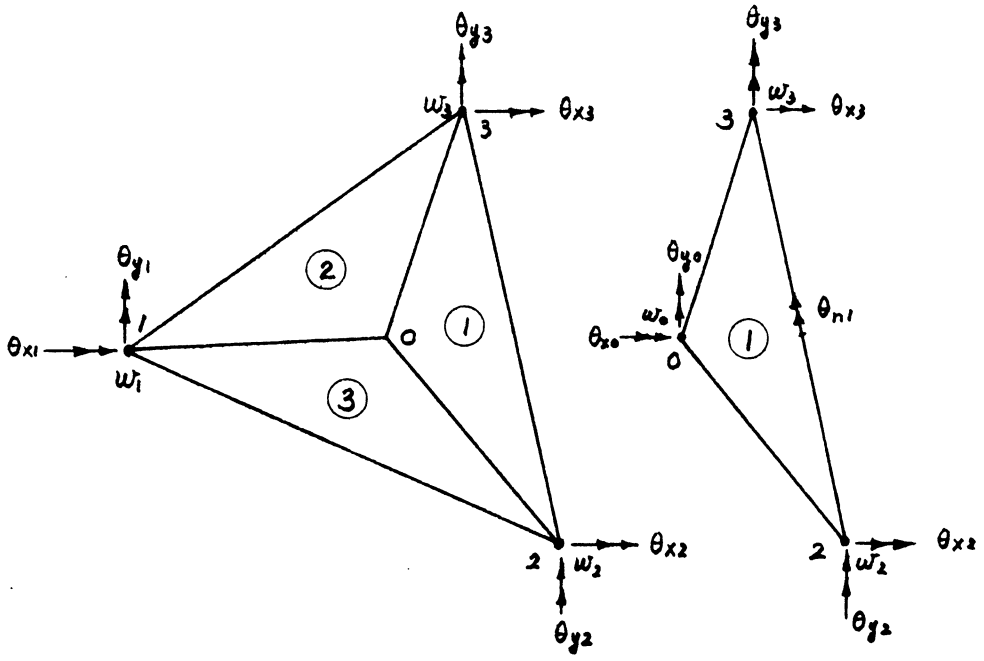

FIG. 3.6 LINEAR CURVATURE COMPATIBLE TRIANGULAR ELEMENT WITH 9 DEGREES OF FREEDOM

Carr [3.5] developed a refined triangular element, using the LCCT9 bending stiffness but employing a quadratic strain triangle to represent the membrane stiffness. The membrane deformations involve 6 degrees of freedom at each node; rotation about the normal to the surface, 2 translations in the surface plane, and 3 components of strain. Therefore there are a total of 9 degrees of freedom at each node. This results in a tremendous increase in computational effort. Clough and Felippa [3.4] developed a highly efficient quadrilateral element which provides improved membrane behavior while retaining the basic 5 degrees of freedom per node system. However, the computing time for forming the element stiffness is approximately 9 times as much as that for the simple triangular element. In view of the crude approximation of the material properties and the advantage of possible element mesh refinement by using simpler elements, the simple triangular element is adopted in this investigation.

3.6 Assemblage of Elements

3.6.1 Coordinate Transformation

The stiffness matrix for the total structure can be obtained most conveniently by the direct stiffness procedure. The two essential steps in the procedure are the coordinate transformations and the subsequent superposition of each element stiffness.

Let $\bar{x}\ \bar{y}\ \bar{z}$ be the element coordinate system, x y z denote the global coordinate system (Fig. 3.8). Define the nodal

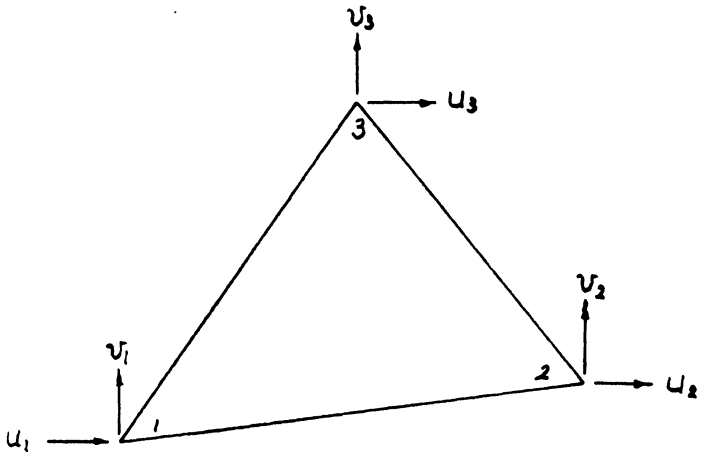

FIG. 3.7 CONSTANT STRAIN TRIANGULAR MEMBRANE ELEMENT

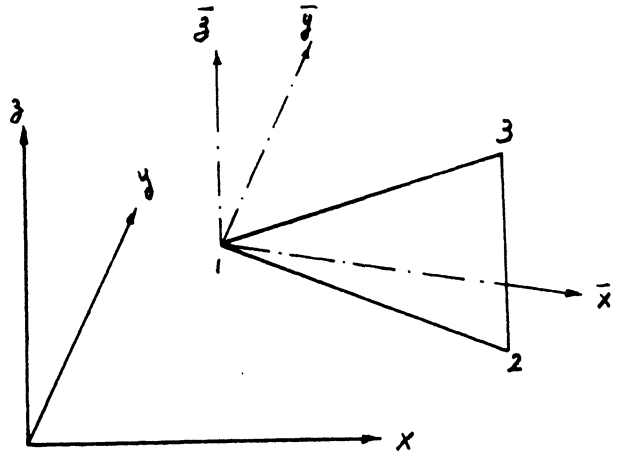

FIG. 3.8 GLOBAL AND ELEMENT COORDINATE SYSTEMS

displacements and nodal forces as follows

$$\{r_i\} = \begin{Bmatrix} u_i \\ v_i \\ w_i \\ \theta_{xi} \\ \theta_{yi} \\ \theta_{zi} \end{Bmatrix} = \begin{Bmatrix} \delta_i \\ \theta_i \end{Bmatrix} \tag{3.35}$$

$$\{R_i\} = \begin{Bmatrix} P_{xi} \\ P_{yi} \\ P_{zi} \\ M_{xi} \\ M_{yi} \\ M_{zi} \end{Bmatrix} = \begin{Bmatrix} P_i \\ M_i \end{Bmatrix} \tag{3.36}$$

Then their components in local and global coordinates will be related by the following relations:

$$\begin{Bmatrix} \bar{u}_i \\ \bar{v}_i \\ \bar{w}_i \end{Bmatrix} = \begin{bmatrix} T_{\bar{x}x} & T_{\bar{x}y} & T_{\bar{x}z} \\ T_{\bar{y}x} & T_{\bar{y}y} & T_{\bar{y}z} \\ T_{\bar{z}x} & T_{\bar{z}y} & T_{\bar{z}z} \end{bmatrix} \begin{Bmatrix} u_i \\ v_i \\ w_i \end{Bmatrix} \quad \text{or} \quad \{\bar{\delta}_i\} = [T]\{\delta_i\} \tag{3.37}$$

where $T_{\bar{x}y}$ = cosine of angle between $\bar{x}$ and y axes, etc.

Inversely, $$\{\delta_i\} = [T]^T \{\bar{\delta}_i\} \tag{3.38}$$

Similarly, $$\{\bar{P}_i\} = [T]\{P_i\} \tag{3.39}$$

and $$\{P_i\} = [T]^T\{\bar{P}_i\} \tag{3.40}$$

Since the rotation about an axis normal to the element surface $\bar{\theta}_{zi}$ is not included in defining the element deformation, it is assumed that the element stiffness corresponding to $\bar{\theta}_{zi}$ is negligible. Therefore $\bar{\theta}_{zi}$ and $\bar{M}_{zi}$ can be ignored in the coordinate transformation, and the following are justified:

$$\begin{Bmatrix} \bar{\theta}_{xi} \\ \bar{\theta}_{yi} \end{Bmatrix} = \begin{bmatrix} T_{\bar{x}x} & T_{\bar{x}y} & T_{\bar{x}z} \\ T_{\bar{y}x} & T_{\bar{y}y} & T_{\bar{y}z} \end{bmatrix} \begin{Bmatrix} \theta_{xi} \\ \theta_{yi} \\ \theta_{zi} \end{Bmatrix} \text{ or } \{\bar{\theta}_i\} = [t]\{\theta_i\} \tag{3.41}$$

$$\begin{Bmatrix} \bar{M}_{xi} \\ \bar{M}_{yi} \end{Bmatrix} = \begin{bmatrix} T_{\bar{x}x} & T_{\bar{x}y} & T_{\bar{x}z} \\ T_{\bar{y}x} & T_{\bar{y}y} & T_{\bar{y}z} \end{bmatrix} \begin{Bmatrix} M_{xi} \\ M_{yi} \\ M_{zi} \end{Bmatrix} \text{ or } \{\bar{M}_i\} = [t]\{M_i\} \tag{3.42}$$

also, $$\{\theta_i\} = [t]^T\{\bar{\theta}_i\} \tag{3.43}$$

$$\{M_i\} = [t]^T\{\bar{M}_i\} \tag{3.44}$$

The transformation relations for the displacements of the three nodes of an element can be written as:

$$\begin{Bmatrix} \bar{\delta}_1 \\ \bar{\theta}_1 \\ \bar{\delta}_2 \\ \bar{\theta}_2 \\ \bar{\delta}_3 \\ \bar{\theta}_3 \end{Bmatrix} = \begin{bmatrix} T & & & & & \\ & t & & & & \\ & & T & & & \\ & & & t & & \\ & & & & T & \\ & & & & & t \end{bmatrix} \begin{Bmatrix} \delta_1 \\ \theta_1 \\ \delta_2 \\ \theta_2 \\ \delta_3 \\ \theta_3 \end{Bmatrix} \tag{3.45}$$

or $$\{\bar{r}\} = [L]\{r\} \tag{3.46}$$

and

$$\{r\} = [L]^T\{\bar{r}\} \tag{3.47}$$

Similarly, for the corresponding nodal forces

$$\{\bar{R}\} = [L]\{R\} \tag{3.48}$$

$$\{R\} = [L]\{\bar{R}\} \tag{3.49}$$

The element equilibrium equation in local coordinate can be written as

$$[\bar{K}]\{\bar{r}\} = \{\bar{R}\} \tag{3.50}$$

Substitute Eq. (3.46) into Eq. (3.50) and premultiply both sides by $[L]^T$:

$$[L]^T[\bar{K}][L]\{r\} = [L]^T\{\bar{R}\}$$

therefore $$[K]\{r\} = \{R\} \tag{3.51}$$

where $$\underset{18\times18}{[K]} = \underset{18\times18}{[L]^T}\underset{18\times18}{[\bar{K}]}\underset{18\times18}{[L]} \tag{3.52}$$

is the element stiffness in global coordinates.

Note that the incomplete transformation, Eqs. (3.41) to (3.44), can be avoided by retaining $\bar{\theta}_{zi}$ and $\bar{M}_{zi}$ while inserting an appropriate number of zeros into the stiffness matrix, and the same final relation Eq. (3.52) will be obtained.

The $\bar{z}$ axis of the element coordinate system is normal to the element plane, while $\bar{x}$ and $\bar{y}$ axes lie on the plane.

In the computer program developed for this study, the directions of $\bar{x}$ and $\bar{y}$ are defined by assuming $\bar{x}$ is given by the direction from node 1 to node 2, or by specifying the direction of $\bar{x}$ or $\bar{y}$.

3.6.2 Boundary Element

In the transformation described above, the element stiffness corresponding to $\bar{\theta}_{zi}$ is assumed to be zero. This will yield a singular set of equilibrium equations when all elements meeting at a node are co-planar. This numerical difficulty can be eliminated by attaching to each node a boundary element with a specified high rotational stiffness about a normal to the shell surface. The boundary element is a one-dimensional element with an axial or torsional stiffness. The stiffness and the direction of the element are specified in the input data. The element stiffness coefficients are added directly to the total structural stiffness matrix. In addition, the boundary element can also be used in the idealization of the following boundary conditions:

(1) external elastic supports,

(2) skewed boundary conditions,

(3) non-zero displacement boundary conditions.

The concept of this versatile boundary element is borrowed from the well-known SAP program [3.6].

3.6.3 Remarks

Clough and Johnson [3.7, 3.8] avoided the difficulty of the "sixth" degree of freedom by neglecting the rotational

degree of freedom about the normal to shell surface at each node. In their approach, all translational degrees of freedom are transformed to a common global coordinate system. The rotational degrees of freedom at each node are transformed to a surface coordinate system with one axis normal to the shell surface, the other two tangent to the surface.

Another alternative suggested by Zienkiewicz [2.11] is to add a fictitious set of rotational stiffness coefficients to each element. As these rotations, normal to the element but not to the shell surface, have components tangent to the surface, the results will be affected by the added fictitious stiffness.

In the author's opinion, the application of the boundary element is superior to the above mentioned two approaches in terms of simplicity and versatility.

Some investigators [3.5, 3.9, 3.10] have attempted to include $\bar{\theta}_{zi}$ as an additional degree of freedom in plane analysis with some success.

3.7 Summary

The shell surface is approximated as an assemblage of flat triangular surfaces. Each triangle is represented by a flat triangular finite element with 5 degrees of freedom at each node. The element is derived from combining a linear curvature compatible triangular bending element with a constant strain triangular membrane element. The coupling effect

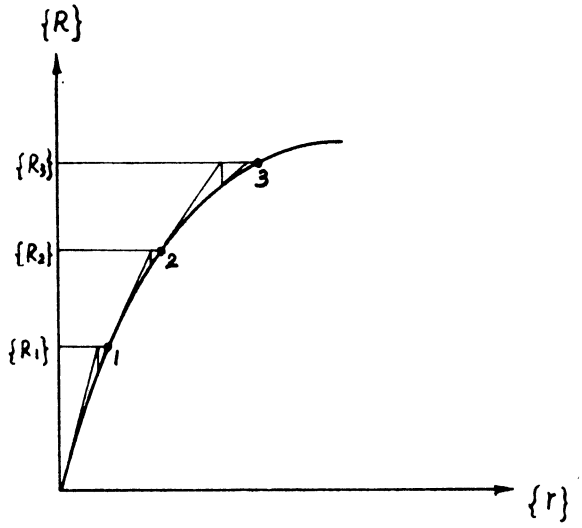

FIG. 4.2 INCREMENTAL ITERATIVE METHOD

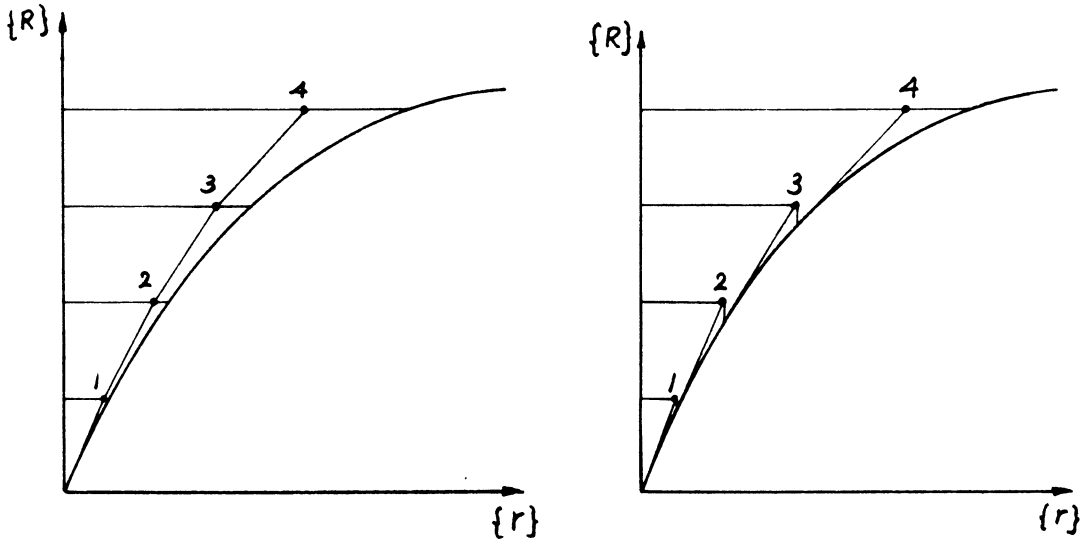

FIG. 4.3 EULER-CAUCHY METHOD

The procedure starts with dividing the loading into finite number of increments. For each load increment, iterations are performed until the equilibrium and constitutive relations are satisfied within a certain allowable limit. The following steps are carried out for each load increment.

(1) Analyze the structure to obtain the increments of nodal forces using the updated stiffness existing at the end of the iterations for the previous load increment. For the first load increment, the initial uncracked linear elastic stiffness is used.

(2) Find the total nodal displacements by adding the new increments to the previous totals.

Do the following steps (3) to (6) for each element.

(3) Calculate the increments and the total values of curvatures and membrane strains at the centroid of the reference plane.

(4) Compute the increments and the total values of the strains and stresses for each layer using the material properties used in forming the current structure stiffness.

(5) Check the stress or strain state of each layer against applicable transition criteria, calculate the unbalanced stresses and update the constitutive properties according to the corrected stresses.

(6) Convert the unbalanced stresses into unbalanced

nodal forces through proper integration. Calculate the new element stiffness if any of the layers change their constitutive properties.

(7) Assemble the unbalanced nodal forces.

(8) Check the unbalanced forces or displacement increments for convergence and divergence. If they have converged, or the prescribed maximum number of iterations has been exceeded, go to step (1) for the next load increment. If they have diverged, stop the solution.

(9) Form new structure stiffness, and analyze for the unbalanced nodal forces to obtain the increments of nodal displacements.

(10) Go to step (2).

Recall the constitutive properties in Chapter 2. The stress-strain relations for uncracked elastic concrete and elastic steel are linear, so the moduli can be considered as tangent moduli. The constitutive relations defined for plastic concrete and plastic steel are incremental, thus are tangent in nature. For the cracked concrete (Fig. 2.11), the modulus in one direction is reduced to zero, but the unbalanced stresses are allowed to release stepwise gradually. In effect, the material stiffness is almost tangent. For the crushed concrete, the stiffness defined is tangent stiffness with a discontinuity at the onset of crushing. In summary, the procedure used can be classified as an incremental tangent stiffness method.

4.4 Evaluation of the Unbalanced Nodal Forces

The unbalanced nodal forces can be obtained by carrying out the integration of Eq. (3.33), once the unbalanced stresses are known. The unbalanced stresses can be found as follows:

$$\{\sigma_i\} = \{\sigma\}' - \{\sigma\} \tag{4.4}$$

where $\{\sigma\}'$ are the total stresses obtained in step (4) of Section 4.3,

$\{\sigma\}$ are the true stresses for the obtained total strains satisfying the constitutive relations.

The true stresses can be easily found for all material states except the plastic concrete. Therefore the following two cases will be further discussed.

(1) Concrete in the plastic state: The incremental stress-strain relations for plastic concrete can be written as:

$$d\{\sigma\} = [D(\sigma)]\, d\{\epsilon\} \tag{4.5}$$

where $[D(\sigma)]$ is a function of stress. Fig. 4.4 shows the changes of stresses and strains in a two dimensional stress space and a n-dimensional stress-strain diagram. $\{\sigma\}_1$, $\{\epsilon\}_1$ are stresses and strains at the beginning of the increment respectively; $\Delta\{\sigma\}'$ and $\Delta\{\epsilon\}$ are stress and strain increments obtained from the linearized solution; $\{\sigma\}'_2$ and $\{\epsilon\}_2$ are obtained total stresses and strains. If the true stress increment $\Delta\{\sigma\}$ corresponding to $\Delta\{\epsilon\}$ can be found, then the

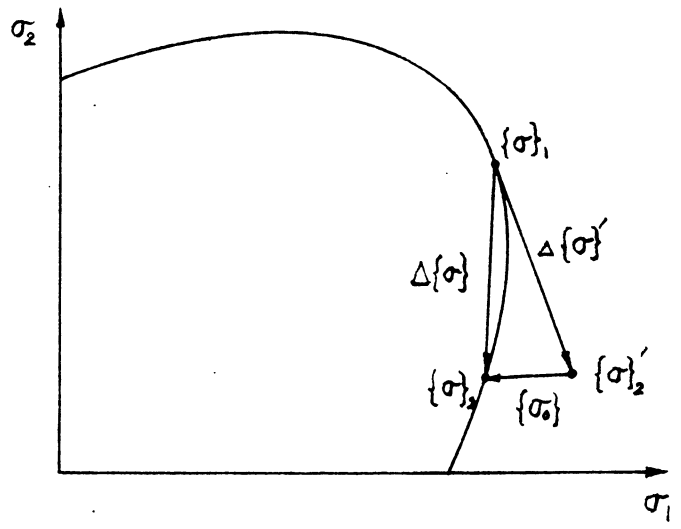

(a) 2-DIMENSIONAL STRESS SPACE

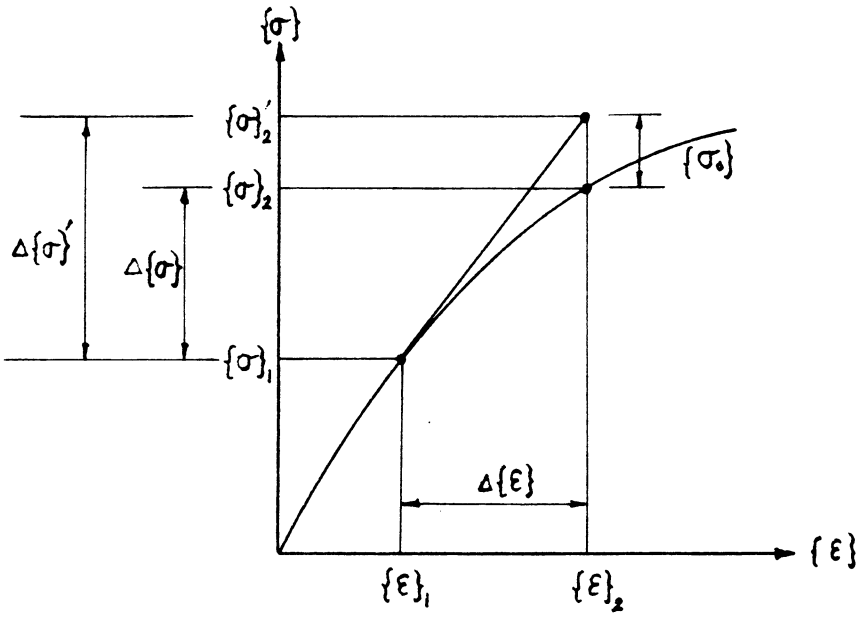

(b) N-DIMENSIONAL STRESS-STRAIN DIAGRAM

FIG. 4.4 EVALUATION OF UNBALANCED STRESSES FOR PLASTIC STATE

unbalanced stress can also be computed as follows.

$$\{\sigma_c\} = \Delta\{\sigma\}' - \Delta\{\sigma\} \tag{4.6}$$

Exact value of $\Delta\{\sigma\}$ cannot be found, but one can resort to numerical solutions of Eq. (4.5), which is a first order matrix differential equation. In this work, the equation is solved by the refined Runge-Kutta method, which involves the following sequence of calculations:

$$\{k_1\} = [D(\sigma_1)]\Delta\{\epsilon\} = \Delta\{\sigma\}'$$

$$\{k_2\} = [D(\sigma_1 + \tfrac{1}{2}k_1)]\Delta\{\epsilon\}$$

$$\{k_3\} = [D(\sigma_1 + \tfrac{1}{2}k_2)]\Delta\{\epsilon\}$$

$$\{k_4\} = [D(\sigma_1 + k_3)]\Delta\{\epsilon\}$$

$$\Delta\{\sigma\}^* = \tfrac{1}{6}(\{k_1\} + 2\{k_2\} + 2\{k_3\} + \{k_4\}) \tag{4.7}$$

The truncation error is of order $(\Delta\epsilon)^5$. Thus Eq. (4.6) is replaced by

$$\{\sigma_c\} = \Delta\{\sigma\}' - \Delta\{\sigma\}^* \tag{4.8}$$

(2) Concrete in elastic-plastic transition state: As shown in Fig. 4.5, during the transition from elastic state to plastic state, the obtained total stresses $\{\sigma\}'_2$

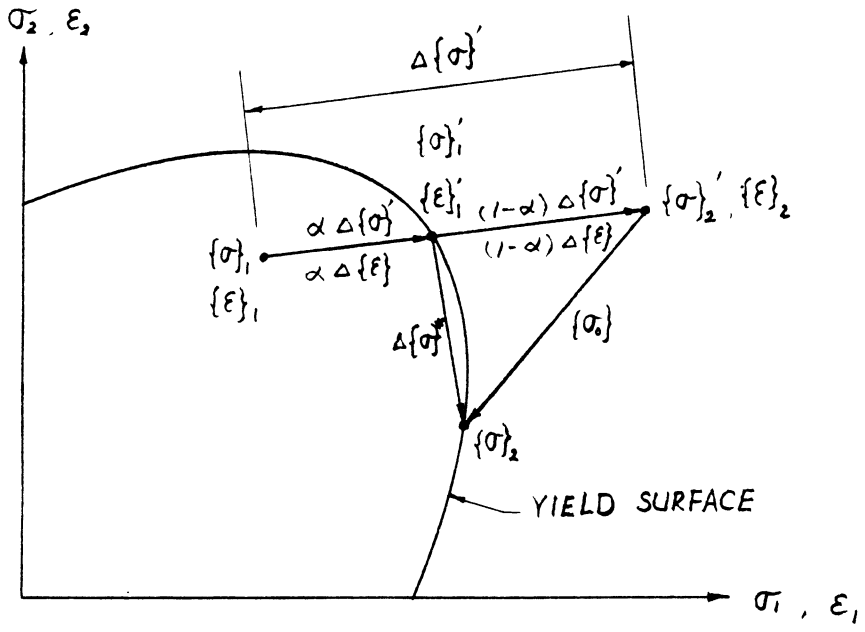

(a) 2-DIMENSIONAL STRESS (STRAIN) SPACE

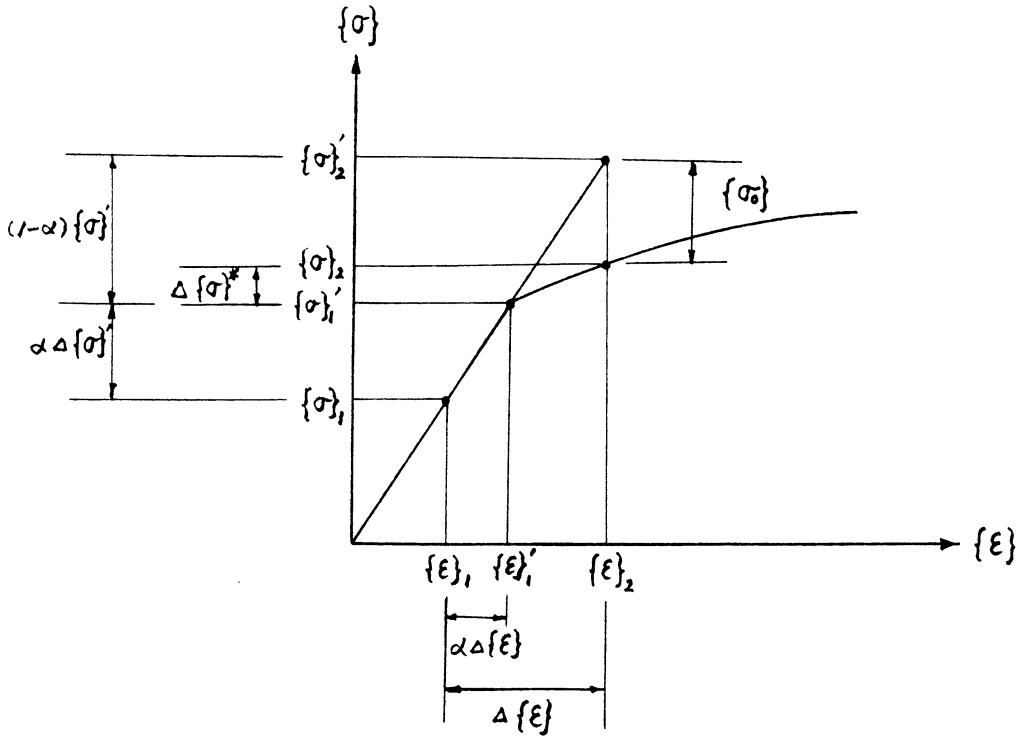

(b) N-DIMENSIONAL STRESS-STRAIN DIAGRAM

FIG. 4.5 EVALUATION OF UNBALANCED STRESSES FOR TRANSITION STATE

will end up beyond the yield surface. The intermediate stresses $\{\sigma\}'_1$ and strains $\{\epsilon\}'_1$ touching the yield surface can be obtained by scaling down the increment by a factor α such that Eq. (2.1) is satisfied.

$$(\sigma_x + \alpha\Delta\sigma_x)^2 + (\sigma_y + \alpha\Delta\sigma_y)^2 - (\sigma_x + \alpha\Delta\sigma_x)(\sigma_y + \alpha\Delta\sigma_y) + 3(\tau_{xy} + \alpha\Delta\tau_{xy})^2 = \bar{\sigma}^2 \tag{4.9}$$

where $\bar{\sigma}$ is the uniaxial yield strength,

and $$\begin{Bmatrix}\sigma_x\\ \sigma_y\\ \tau_{xy}\end{Bmatrix} = \{\sigma\}_1 \qquad \begin{Bmatrix}\Delta\sigma_x\\ \Delta\sigma_y\\ \Delta\tau_{xy}\end{Bmatrix} = \Delta\{\sigma\}'$$

α can be obtained by solving Eq. (4.9), then

$$\{\sigma\}'_1 = \{\sigma\}_1 + \alpha\Delta\{\sigma\}' \tag{4.10}$$

$$\{\epsilon\}'_1 = \{\epsilon\}_1 + \alpha\Delta\{\epsilon\} \tag{4.11}$$

The true stress increments $\Delta\{\sigma\}^*$ for the strain increments $(1-\alpha)\Delta\{\epsilon\}$ can be obtained by the same procedure as in the last case. The unbalanced stresses are then

$$\{\sigma_i\} = (1-\alpha)\Delta\{\sigma\}' - \Delta\{\sigma\}^* \tag{4.12}$$

4.5 Convergence Criteria

In the proposed iteration procedure, the equilibrium equation is operated on to solve the nodal displacements. The two most obvious criteria of measuring the convergence at the end of an iteration are the magnitude by which

equilibrium is violated or the accuracy of the total displacements. The violation of the equilibrium can be measured by the magnitude of the residual unbalanced nodal forces. The accuracy of the nodal displacements can be measured by the magnitudes of the additional increment of displacements.

In the computer program developed for this study, either one of the above mentioned two criteria can be used according to the prescription in the input data. The six components of the nodal forces or nodal displacements corresponding to six degrees of freedom are treated independently. The maximum vector norm is used to measure the error for each component. Let the Δr_{in}, ΔR_{in} denote the increment of displacement and the unbalanced force respectively for the i th component at node n. Then, for the unbalanced force criterion the errors

$$\| \varepsilon \|_i = \max_n | \Delta R_{in} | \quad ;$$

for the displacement increment criterion the errors

$$\| \varepsilon \|_i = \max_n | \Delta r_{in} | \quad ;$$

where i = 1, ---, 6. When all six components of the errors become smaller than their convergence criteria, the computer will stop the iteration and go on to the next load increment. The residual unbalanced nodal forces will be carried over and added to the next load increment.

Usually the failure of a structure is symptomatically indicated by the divergence of the iteration. In order to

prevent the computer from wasteful computation, a divergence criterion is also specified together with the adopted convergence criterion. The solution will stop whenever any component of the errors exceeds its divergence criterion.

To further guard the solution from overstringent convergence criteria, a ceiling has to be specified in the input data to limit the number of iterations for one load increment. The solution will go on to the next load increment if the number of iterations for a particular increment exceeds the limit.

4.6 Computer Program

4.6.1 Input and Output

A computer program called NARCS (Nonlinear Analysis of Reinforced Concrete Shells) has been developed to implement the proposed method of analysis. The program was coded in FORTRAN IV language and has been tested on the CDC 6400 computer at the University of California, Berkeley. It can analyze free-form reinforced concrete shells subjected to constant dead loads and monotonically increasing arbitrary live loads. A brief description of the input and output is given below.

The required input data includes:

(1) Control data such as number of joints, number of types of material properties, number of layer systems, number of load increments, convergence

control code, output control code, definition of local coordinate systems, etc.

(2) Convergence and divergence criteria.

(3) Concrete and steel material properties.

(4) Construction of layer systems.

(5) Nodal point coordinates and boundary conditions.

(6) Element data for each shell element.

(7) Boundary elements.

(8) Concentrated joint loads.

(9) Load increments.

The output consists of:

(1) Input and generated data as a check.

The following data for each load increment or each iteration.

(2) Load factor (multiple of the input live load).

(3) Unbalanced nodal forces.

(4) Nodal displacements in global coordinates.

(5) Centroidal curvatures and/or nodal displacements in local coordinates for each shell element if requested.

(6) Stresses and material state indices for concrete and steel layers for each shell element.

(7) Strains for concrete and steel layers for each shell element if requested.

(8) Stresses in the boundary elements. Note that reactions can be obtained by proper interpretation of these stresses.

If the gravity load (dead load) is not included, the input loading will be considered merely as a load pattern. The first linear elastic solution will be scaled up or down to a point where one of the layers first starts cracking or yielding, the corresponding load will be termed the proportional limit. The input increments will be considered as fractions of the proportinal limit. On the other hand, if the gravity load is included, no proportional limit will be computed, and the input increments are taken as fractions of the input live load.

4.6.2 Flow Charts

The flow chart of the incremental iterative procedure is shown in Fig. 4.6. As supplements, flow charts for subroutines PROP and CHECK are shown in Figs. 4.7 and 4.8. Subroutine PROP finds the proportional limit, subroutine CHECK checks the stress state, updates the stiffness and calculates the unbalanced forces.

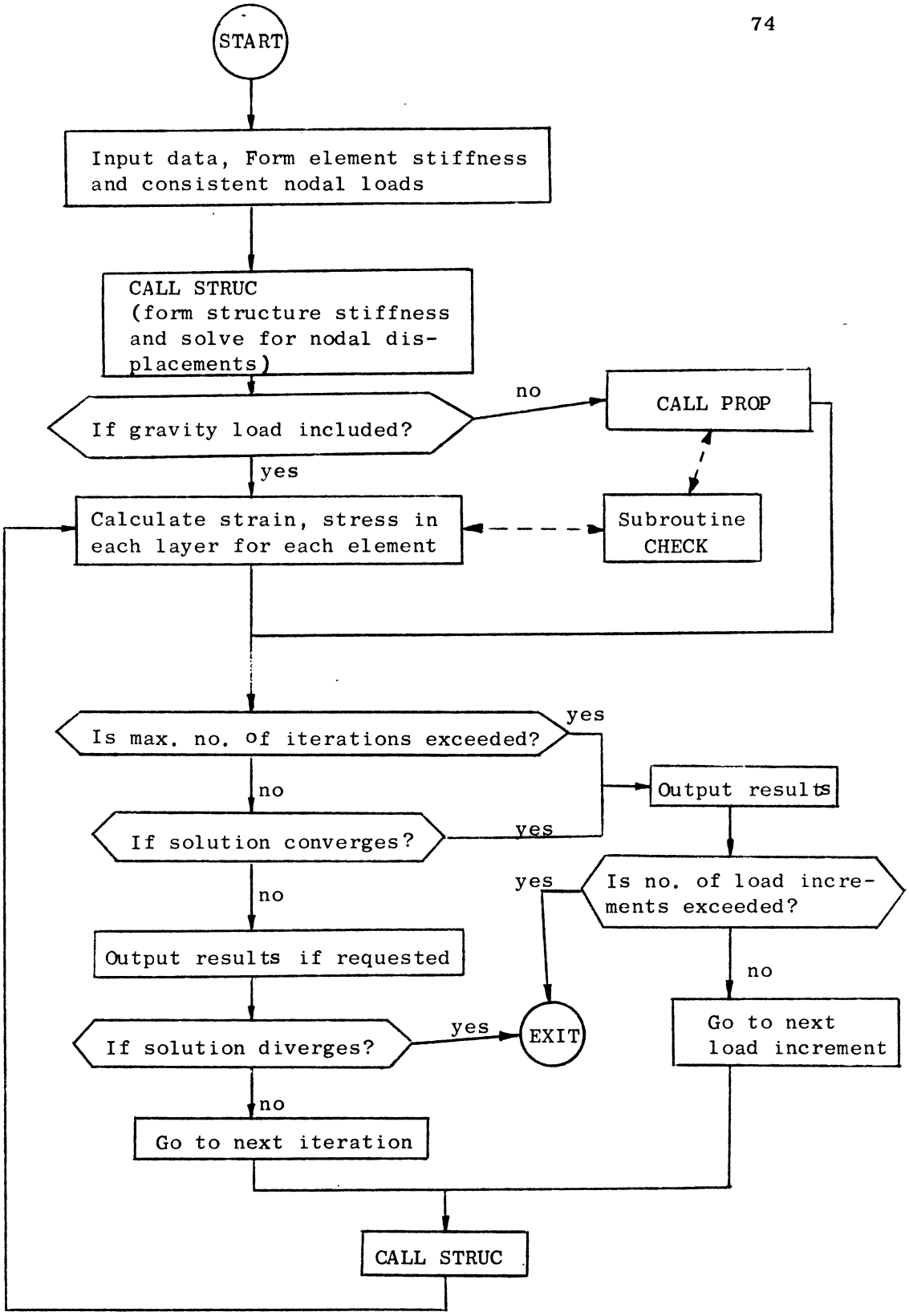

Fig. 4.6 Flow Chart for NARCS

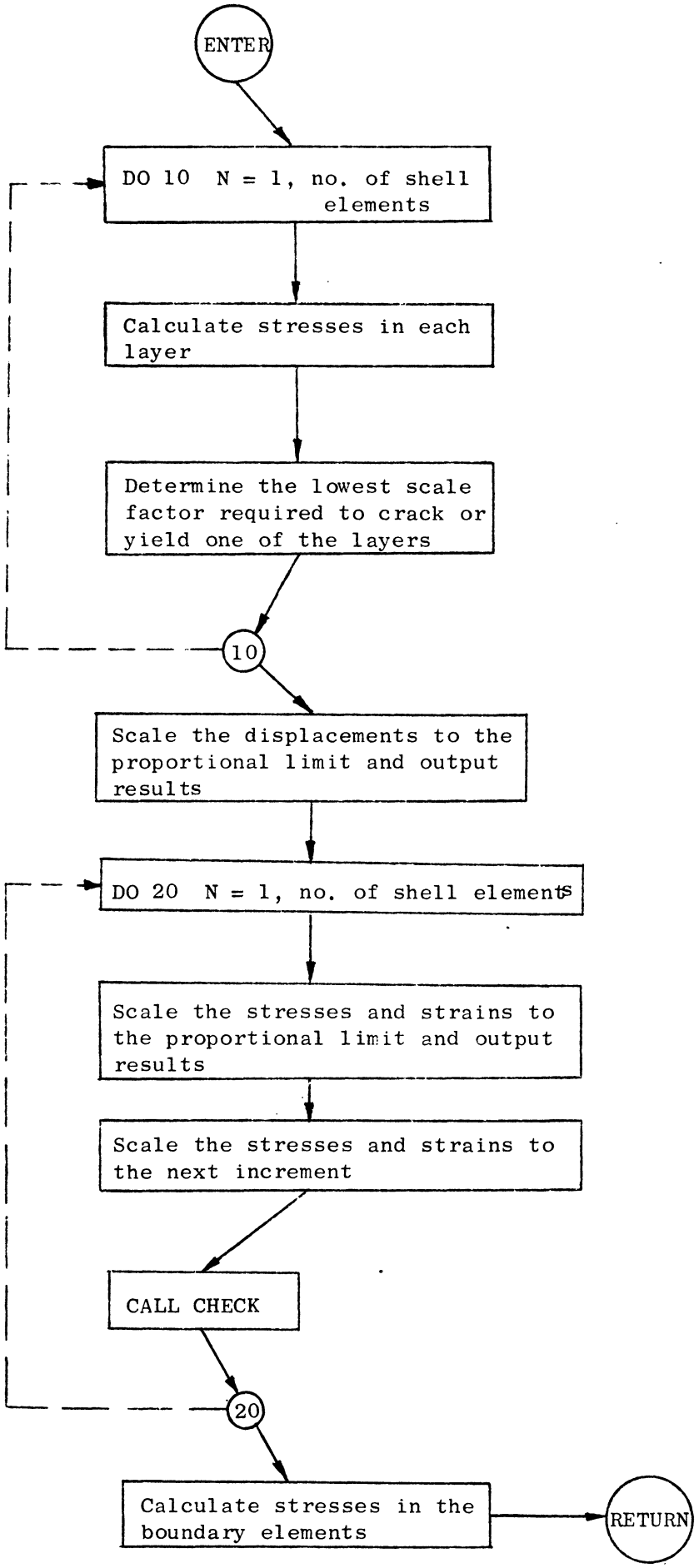

Fig. 4.7 Flow Chart for Subroutine PROP

analyzed through the nonlinear stage till failure to demonstrate the applicability of the proposed method of analysis.

5.2 Reinforced Concrete Beams

Reinforced concrete beams can be treated as strips of one-way slabs. As described in Chapter 3, the transverse shear deformation is neglected in the basic kinematic assumptions, so any point in the shell is in a plane stress state. Consequently diagonal tension cracks resulting from a combination of shearing and flexural tension stresses can not be taken into account in this analysis. In the following beam examples, it is assumed that all of the beams are adequately reinforced with web reinforcement, such that shear type failures are excluded.

5.2.1 Example 1 -- Hypothetical Beams

Three simply supported beams with identical configuration, loading condition and material properties, but with different reinforcement ratios are analyzed (Fig. 5.1). Each of the beams represents a distinct reinforcement condition (Fig. 5.2a). The balanced design case is the condition in which the concrete and the reinforcing steel reach the ultimate yield stress at the same time. The under-reinforced case is the condition with a smaller amount of steel in which the steel yields before the concrete. For the over-reinforced case, the reverse is true, with the concrete reaches its ultimate strength before the steel yields. The same finite element mesh layout, layer system construction

and material properties are used for all three beams (Fig. 5.1).

No experimental data are available to determine quantitatively the tension stiffening effect. At this initial stage, three unloading curves (Fig. 5.2b) are assumed to study the influence of the effect on the solution for each of the reinforcement conditions. Type O assumes that once one of the concrete principal stresses exceeds the tensile strength cracks form in the perpendicular direction and the principal stress drops abruptly to zero, which is equivalent to totally ignoring the tension stiffening effect. Types A and B are two intuitively assumed unloading curves. Type A represents the more rapid unloading of the concrete stress, and thus includes less stiffening effect from the concrete between cracks than Type B. Both A and B release the concrete stress completely at a strain about five times of that corresponding to the tensile strength.

The resulting load-deflection curves are shown in Figs. 5.3 to 5.5, and failure mechanisms at the ultimate loads in Fig. 5.6. It can be seen that the influence of the tension stiffening on the post-cracking load-deflection response is quite significant for the under-reinforced case (Fig. 5.3). This is consistent with the wide spreading of the cracked region in Fig. 5.6(a). However all three curves converge eventually because ultimately most of the cracked concrete reaches the zero stress state in Fig. 5.2(b). For the balanced

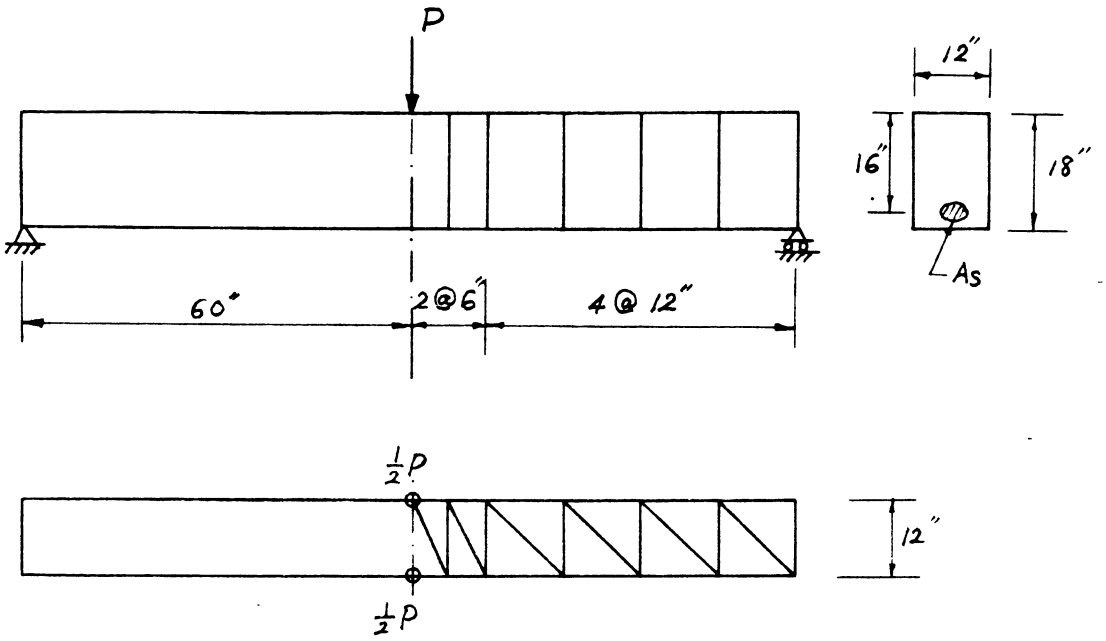

(a) ELEVATION AND PLAN OF FINITE ELEMENT MESH LAYOUT

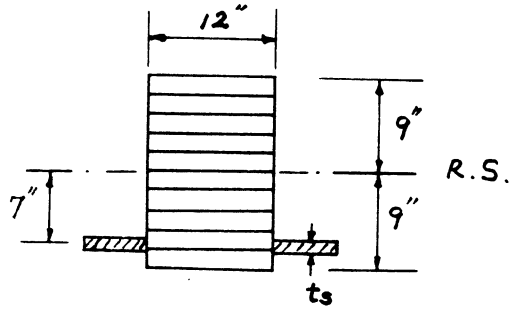

(b) LAYER SYSTEM

E_c	=	4150	ksi
ν	=	0.15	
f_t'	=	0.77	ksi
f_c'	=	5.5	ksi
ε_u	=	0.002	
α	=	1.0	
E_s	=	29,000	ksi
f_y	=	45	ksi

(c) MATERIAL PROPERTIES

FIG. 5.1 EXAMPLE 1 -- HYPOTHETICAL BEAMS

CASE	STEEL AREA (in^2)	SMEARED THICKNESS (in)	STEEL RATIO (%)	REMARK
A	2	0.167	1.04	UNDER-REINFORCED
B	10	0.833	5.2	BALANCED DESIGN
C	30	2.500	15.6	OVER-REINFORCED

(a) REINFORCEMENT

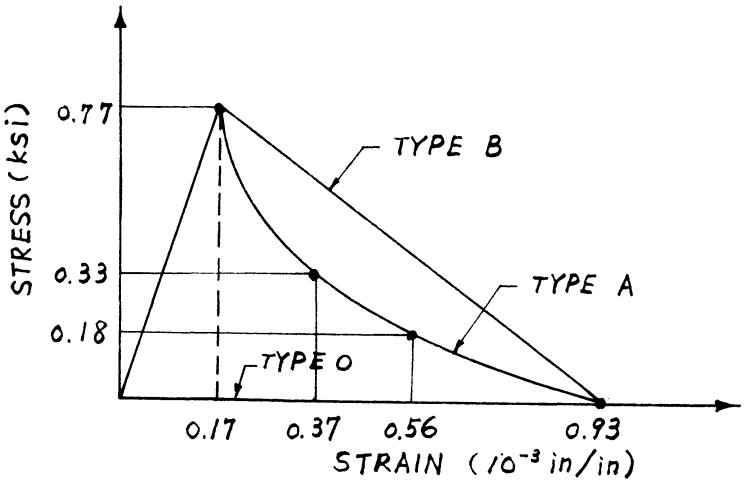

(b) ASSUMED TENSION STIFFENING EFFECT

FIG. 5.2 REINFORCEMENT & TENSION STIFFENING FOR EXAMPLE 1

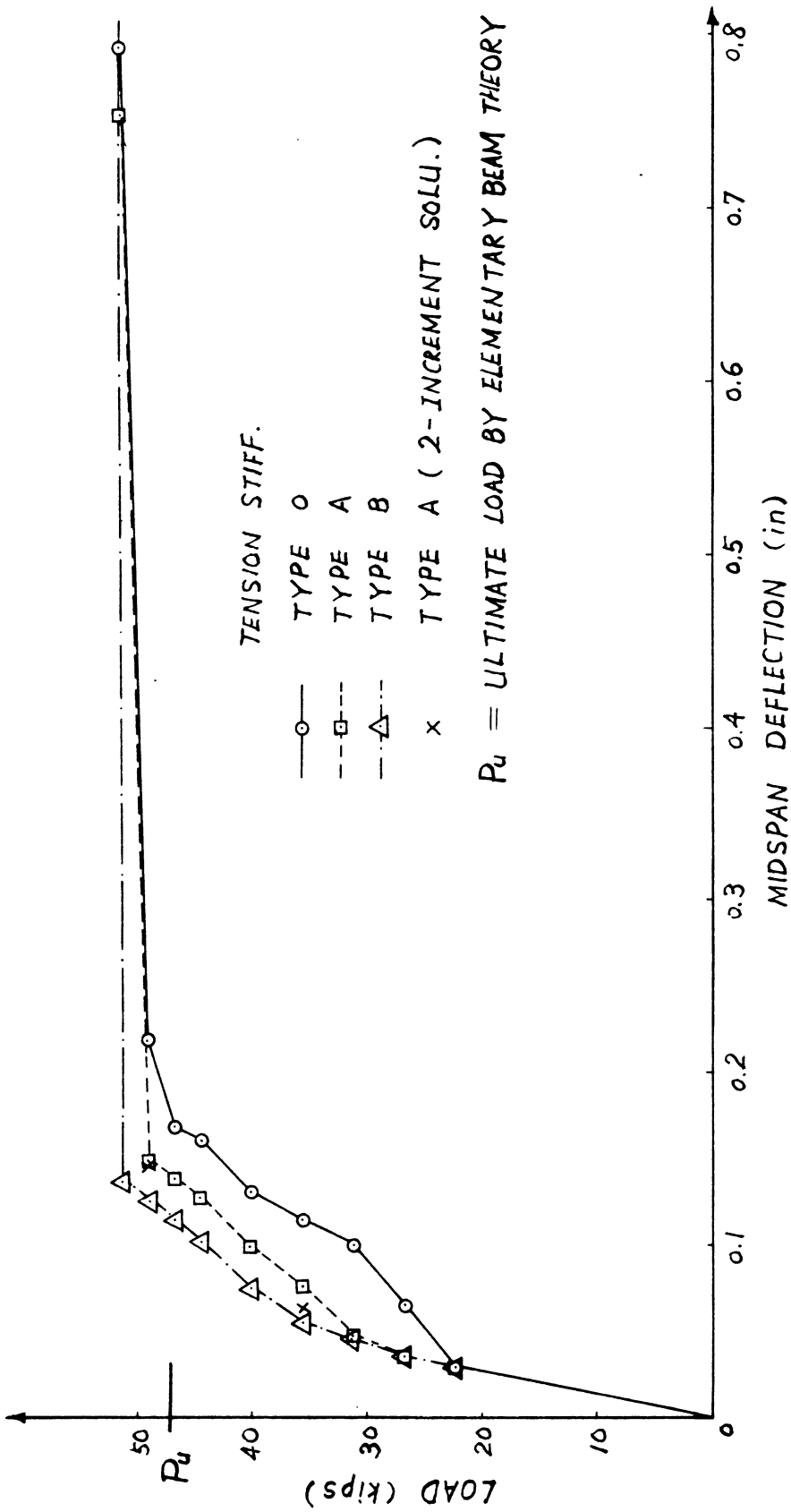

FIG. 5.3 LOAD-DEFLECTION CURVE FOR EXAMPLE 1A

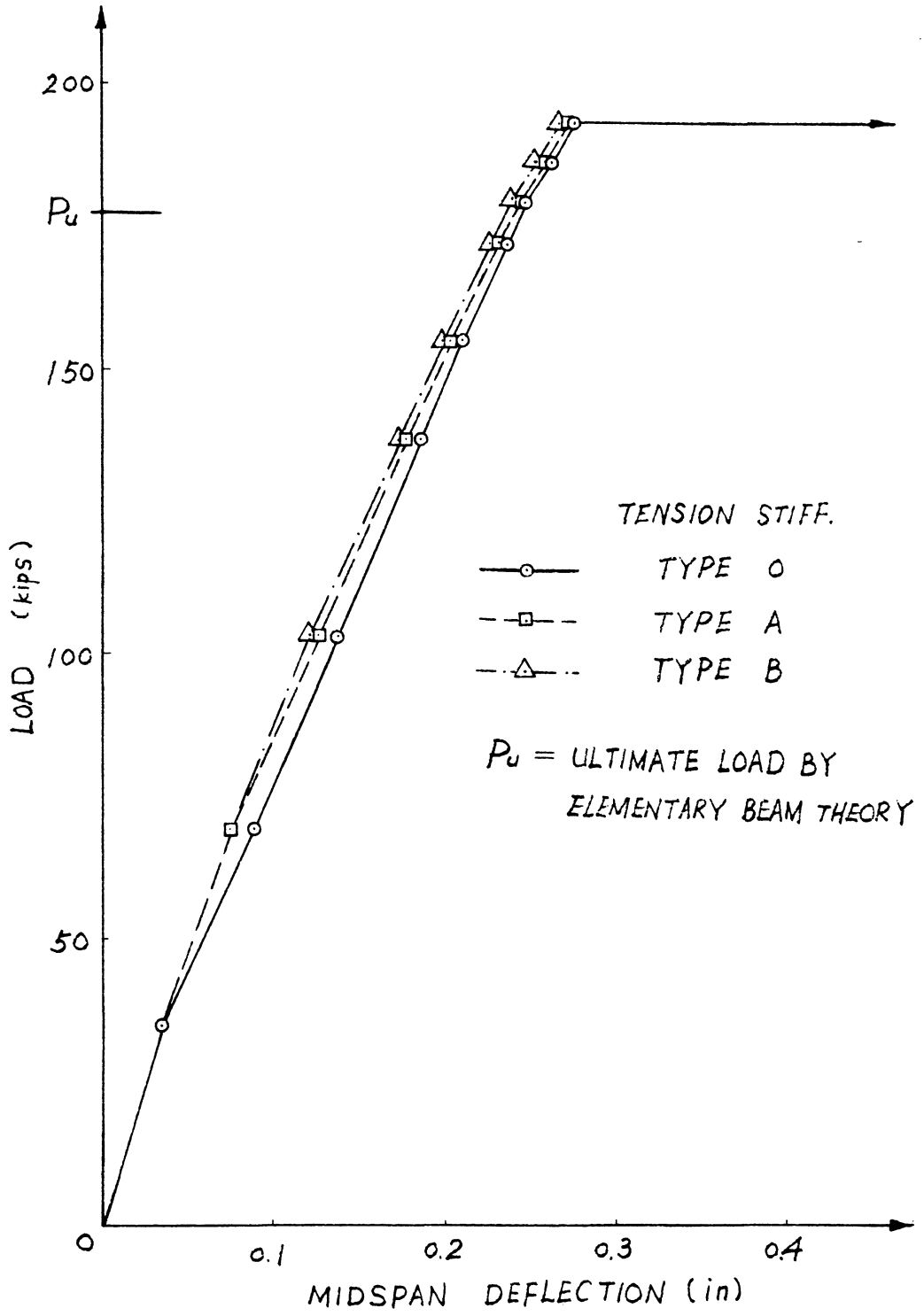

FIG. 5.4 LOAD-DEFLECTION CURVE FOR EXAMPLE 1B

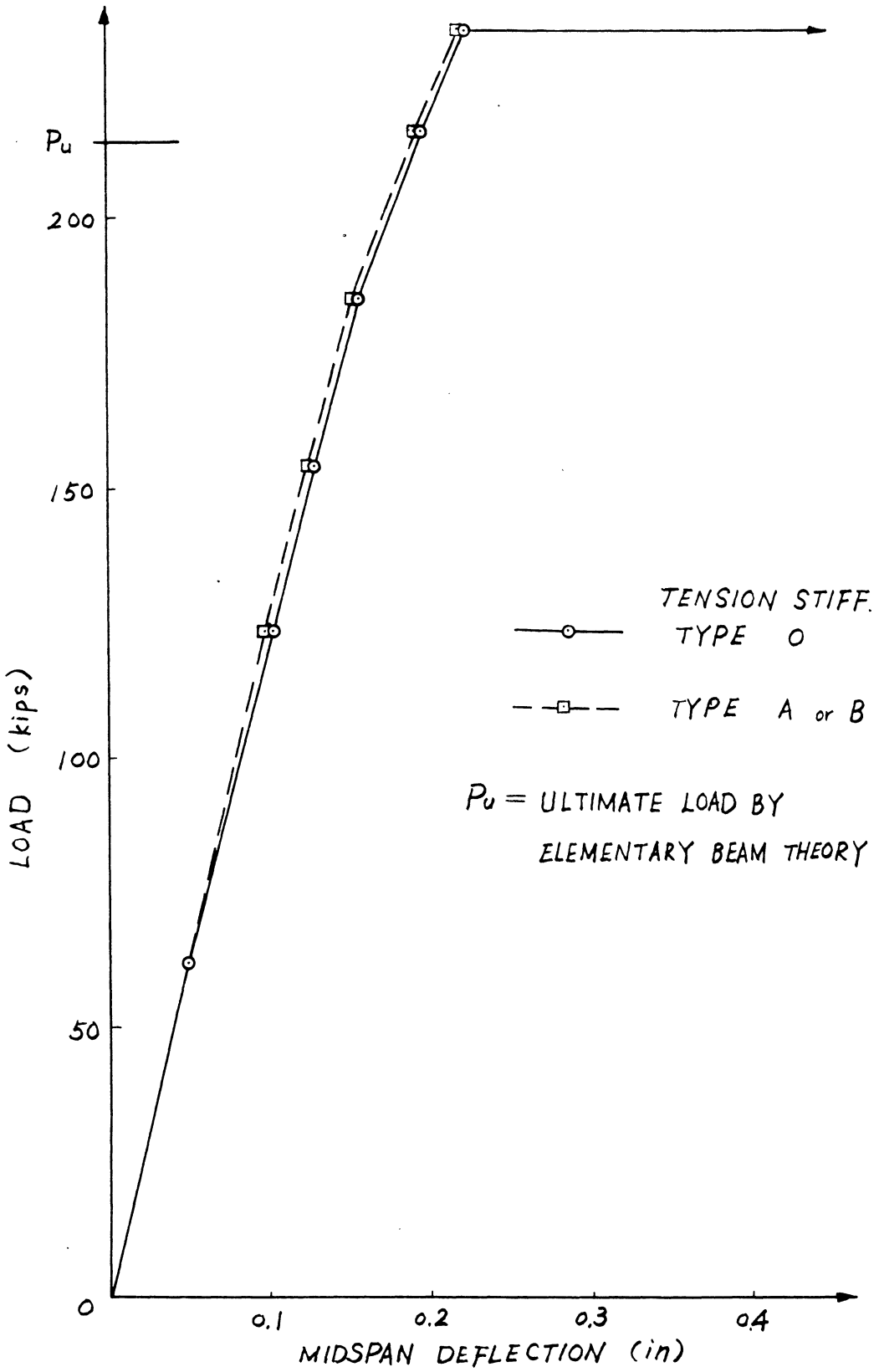

FIG. 5.5 LOAD-DEFLECTION CURVE FOR EXAMPLE 1C

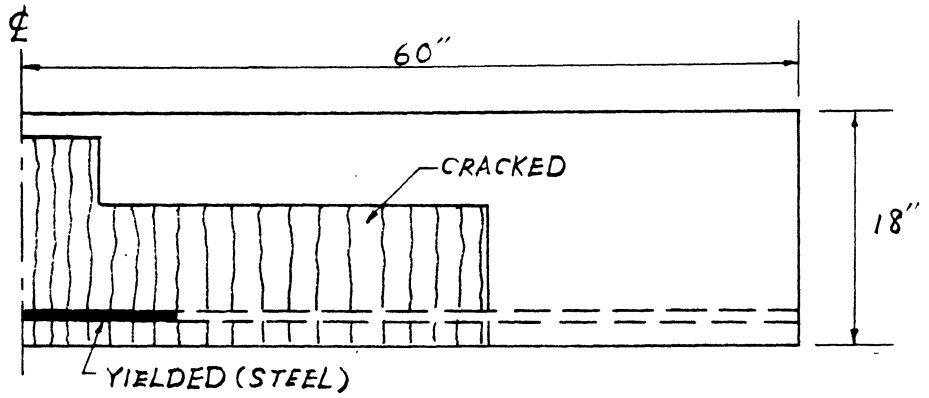

(a) UNDER-REINFORCED

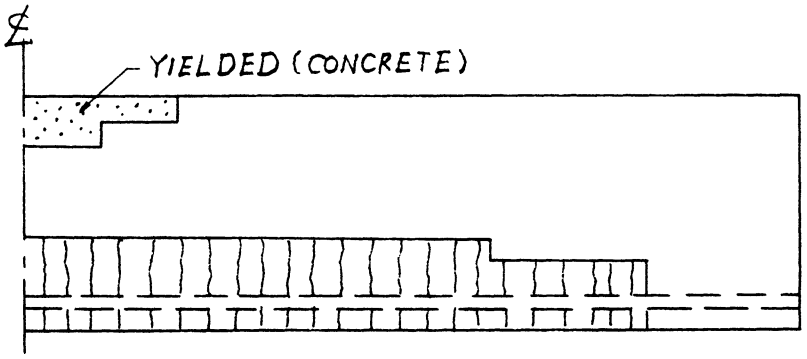

(b) BALANCED DESIGN

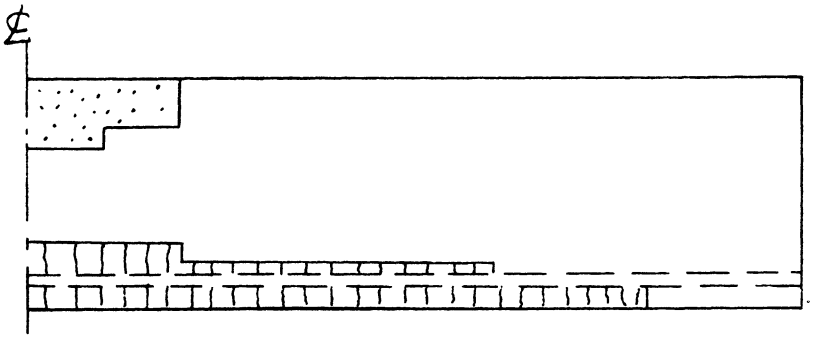

(c) OVER-REINFORCED

FIG. 5.6 FAILURE MECHANISMS FOR EXAMPLE 1

design case, the influence of the tension stiffening is small (Fig. 5.4), and the extent of the cracked region is limited (Fig. 5.6b). The effect becomes negligible for the over-reinforced case (Fig. 5.5 and 5.6c). It is concluded that the significance of the tension stiffening effect decreases with the increase of the reinforcement ratio.

Also shown on the load-deflection diagrams are the ultimate loads (Pu's) calculated from the elementary beam theory, assuming a linear strain distribution over the depth, trapezoidal compressive concrete stress blocks, and neglecting the tensile concrete stresses. The differences of the Pu's and the ultimate loads from the computer solution are due to the contribution of the tensile concrete stresses. The contribution increases with the extent of the uncracked regions of the concrete in tension. Consequently, it is found that the effect of the tensile concrete stresses on the ultimate loads increases with the reinforcement ratio.

Finally, in order to study the effect of the magnitude of load increment, Example 1A with Type A stiffening was reanalyzed with two increments between the proportional load and the ultimate load (Fig. 5.3). These results show the path-dependency of the solution.

5.2.2 Example 2 -- Bresler-Scordelis Beam B3

Among a series of reinforced concrete beams tested by Bresler and Scordelis [5.1, 5.2], one designated as B3 was selected for study. The simple span beam had web-reinforcement and a long span length, such that a flexural

failure occured. A concentrated load is applied at the middle of the span. The beam elevation, cross-section and the finite element mesh used are shown in Fig. 5.7. The layer systems, material properties and the assumed tension stiffening relation are shown in Fig. 5.8.

Fig. 5.9 shows the load-deflection curves obtained from both the experiment and the analysis. In the experiment the beam was first loaded to about 30% of ultimate in two or three increments and then the load was removed. The load was reapplied in 10 kip increments to a point near failure and then in 5 kip increments until failure occured. The experimental curve shown in Fig. 5.9 was obtained from the deflections recorded during the final cycle of loading from zero to ultimate. On the analytical curve the load corresponding to the first point is the proportional load limit - the load when the tensile cracking first starts. Comparing the two curves, the slight discrepancy in the lower load range is attributed to the above mentioned unloading and reloading in the experiment. The difference in the higher load range is due to the bilinear approximation of the concrete stress-strain relation in the analysis which over-estimates the concrete modulus at high stresses. Nevertheless, excellent agreement is found for the ultimate loads.

Shown in Fig. 5.10 are the crack patterns at the ultimate load for both the experiment and the analysis. In the experiment a few diagonal tension cracks did appear in certain regions, but never constituted a failure mechanism. The actual failure mode is a flexure-compression failure. It can be seen from the figure that the average cracked region from the analytical solution

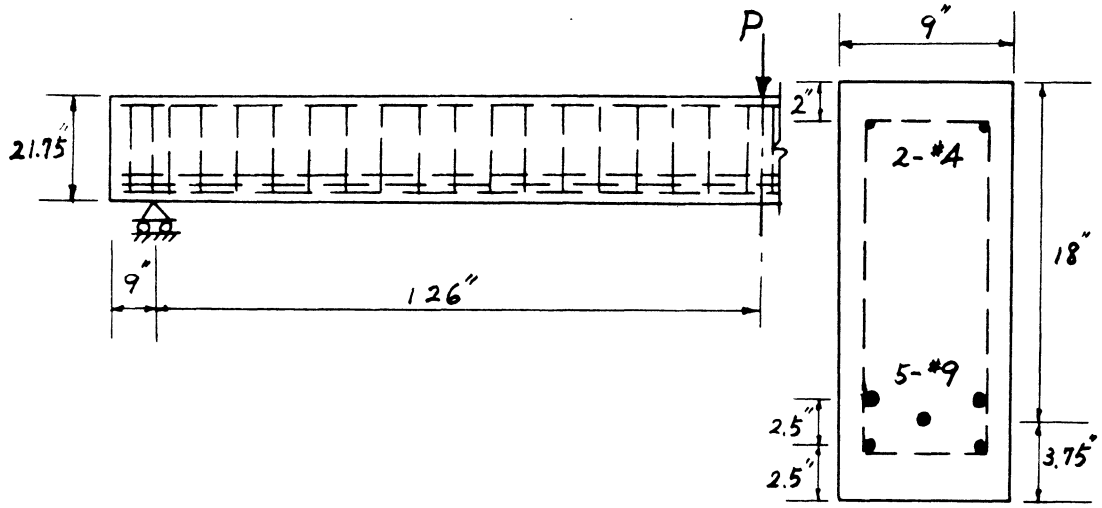

(a) ELEVATION AND CROSS-SECTION

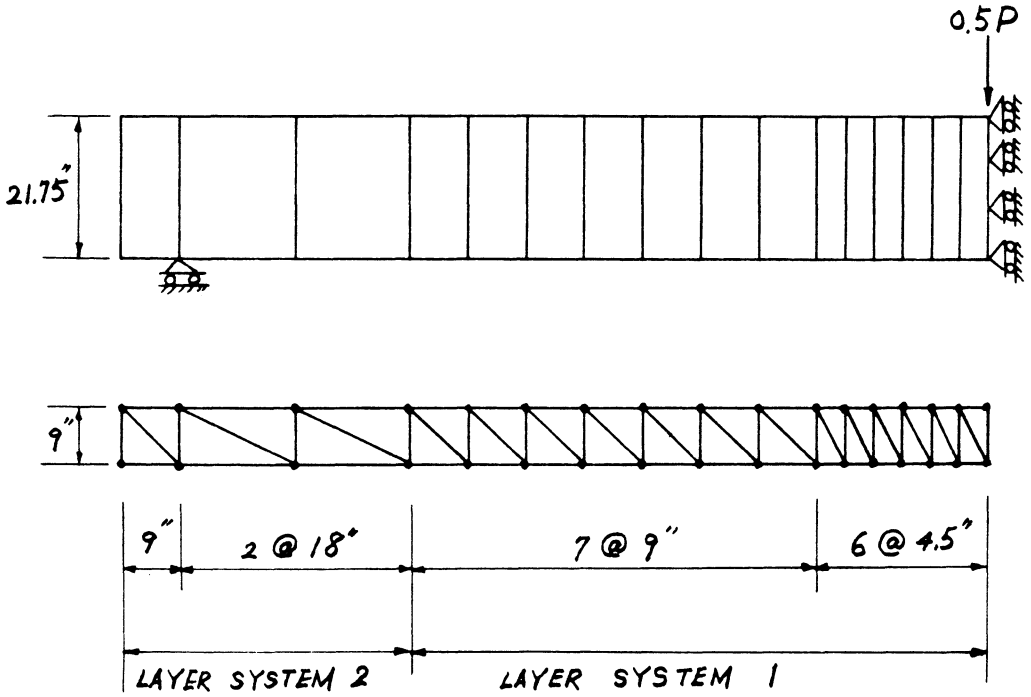

(b) FINITE ELEMENT MESH

FIG. 5.7 EXAMPLE 2 -- BRESLER-SCORDELIS BEAM B3

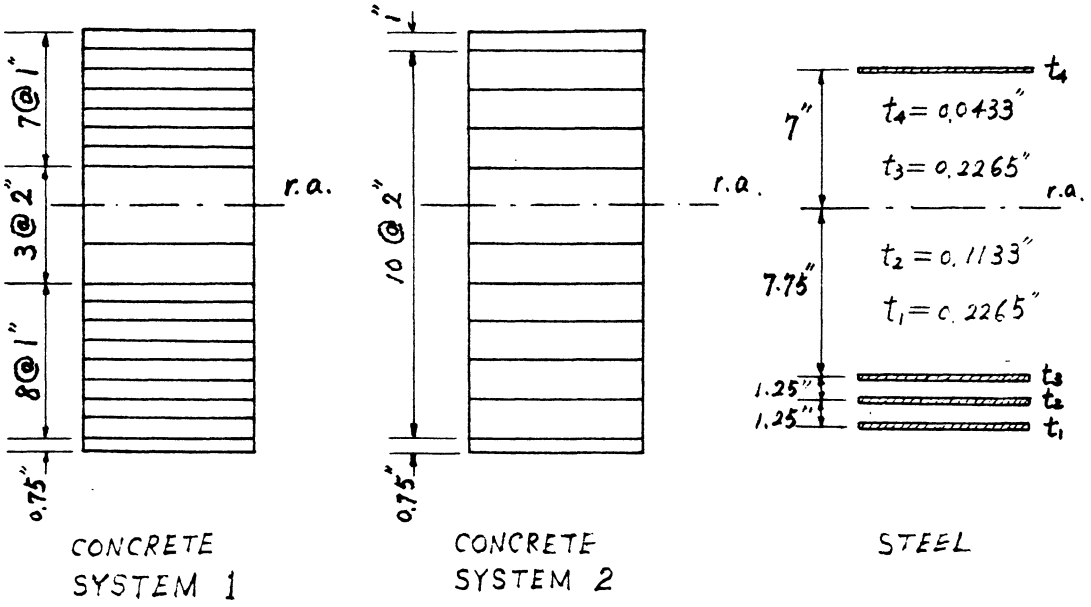

(a) LAYER SYSTEMS

CONCRETE :

$E_c = 4640$ ksi

$f_c' = 5.62$ ksi

$f_t' = 0.611$ ksi

$\nu = 0.15$

$\epsilon_u = 0.002$

STEEL :

9 BARS :

$E_s = 30,700$ ksi

$f_y = 80.1$ ksi

4 BARS :

$E_s = 29,200$ ksi

$f_y = 50.0$ ksi

(b) MATERIAL PROPERTIES

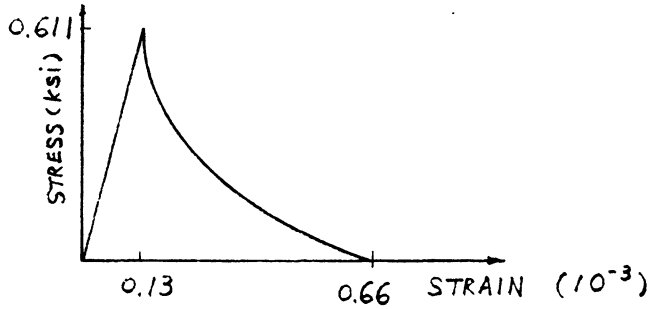

(c) ASSUMED TENSION STIFFENING

FIG. 5.8 LAYER SYSTEMS & MATERIAL PROPERTIES FOR EXAMPLE 2

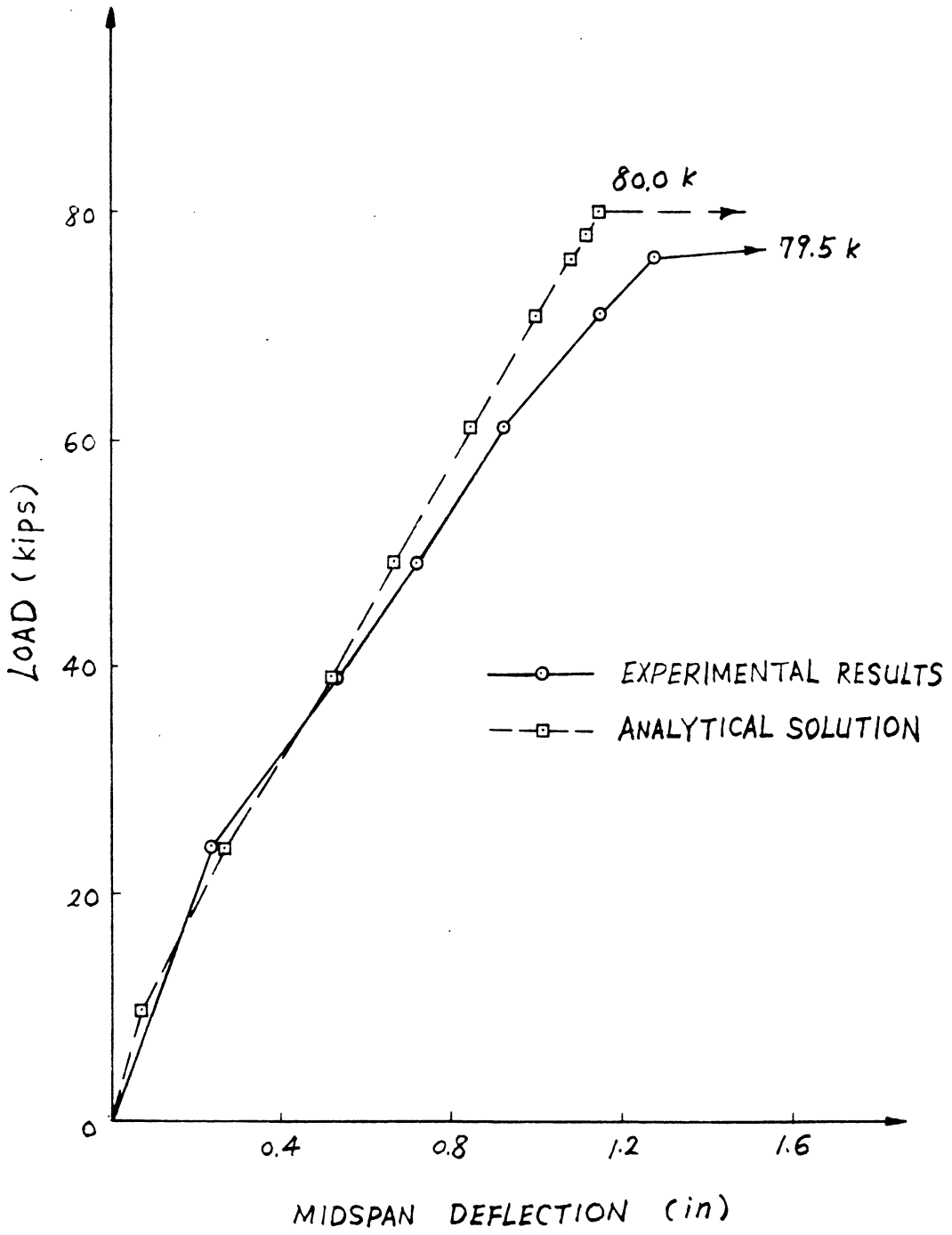

FIG. 5.9 LOAD-DEFLECTION CURVES FOR EXAMPLE 2

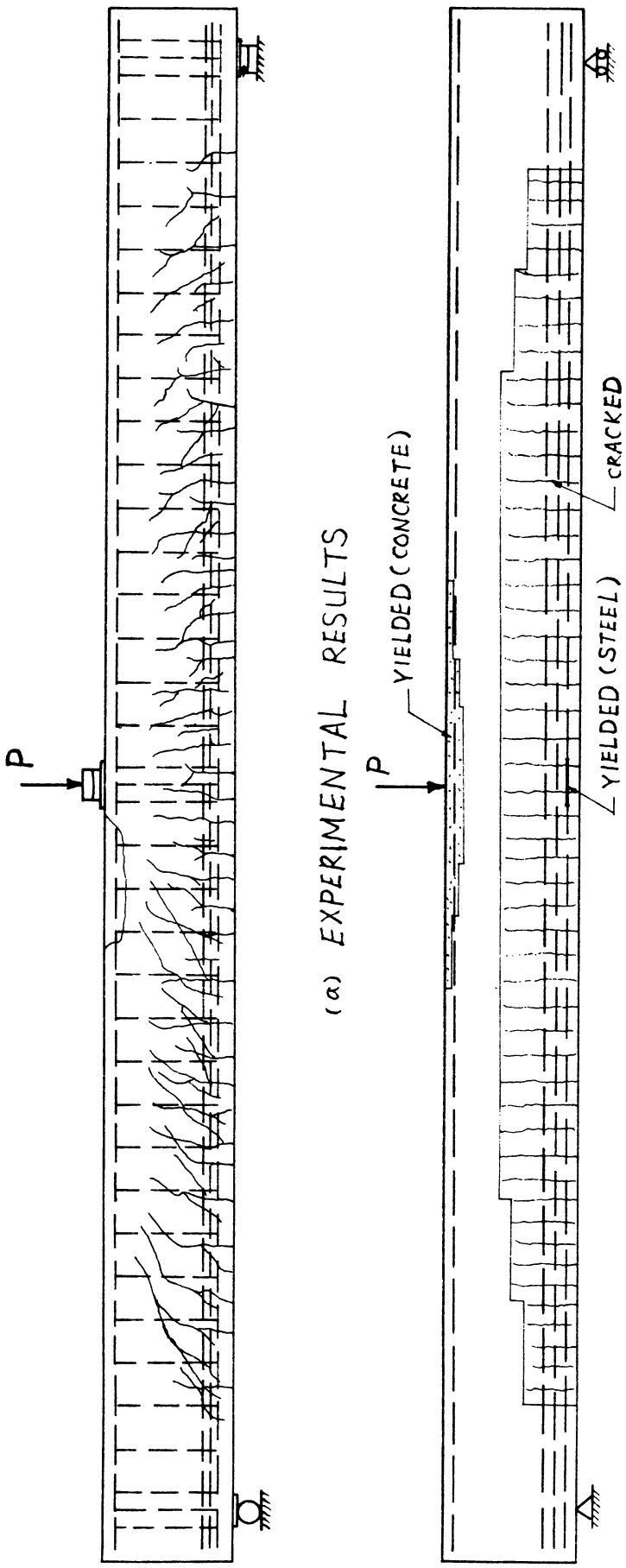

FIG. 5.10 CRACK PATTERNS AT ULTIMATE LOADS FOR EXAMPLE 2

coincides with that observed in the experiment. The yielded region of concrete in the analytical results also concurs with the compressive crushed region in the experimental results.

5.3 Reinforced Concrete Slabs

5.3.1 Example 3 -- Cardenas Circular Slab C2

An isotropically reinforced concrete circular slab tested by Cardenas and Sozen [5.3] is selected for analysis. The shape of the specimen is chosen to demonstrate the adaptability of the triangular finite element. The slab is simply supported and subjected to a uniformly distributed moment all around the periphery. It should be realized that in this example, unlike the beam examples, the concrete is in a state of biaxial stresses. Therefore the proposed method of analysis can be further verified for two-dimensional cases.

The dimensions, reinforcement, loading condition, finite element mesh and layer systems are shown in Fig. 5.11. Since the slab is in a constant curvature state, only two elements are needed to satisfactorily approximate one quadrant of the structure. Using the axisymmetrical condition of the problem, only one quadrant of the slab need to be analyzed. The applied distributed moment is replaced by statically equivalent nodal moments. The material properties and the assumed tension stiffening relation are given in Fig. 5.12.

Figs. 5.13 through 5.15 show the plots of the applied moment vs. curvature, concrete strain and steel strain obtained from both the experiment and the analysis. Reasonably good agreement is found for all of the plots. The discrepancy in the moment-steel strain plots (Fig. 5.15) may be attributed to the possible difference between the assumed reinforcement position in the

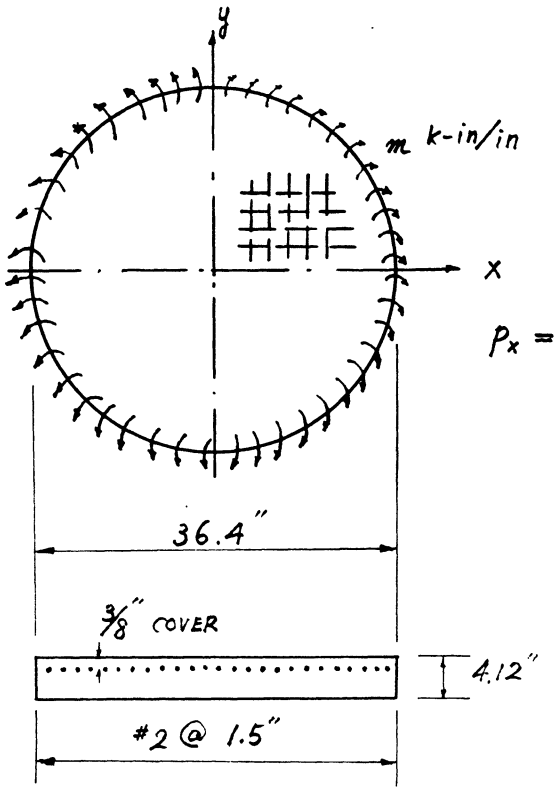

(a) PLAN VIEW AND CROSS-SECTION

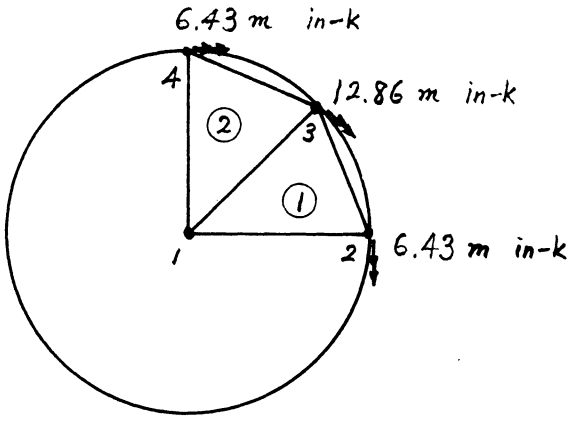

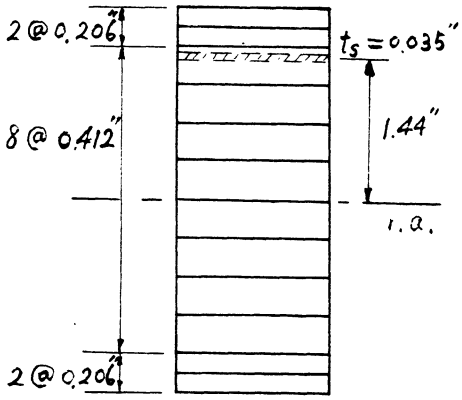

(b) FINITE ELEMENT MESH (c) LAYER SYSTEMS

FIG. 5.11 EXAMPLE 3 -- CARDENAS SLAB C2

$E_c = 4080$ ksi $\qquad E_s = 30,000$ ksi

$\mu_t = 0.15$ $\qquad f_y = 50$ ksi

$f_c' = 4.58$ ksi

$f_t' = 0.474$ ksi

$\alpha = 1.0$

$\epsilon_u = 0.003$

(a) MATERIAL PROPERTIES

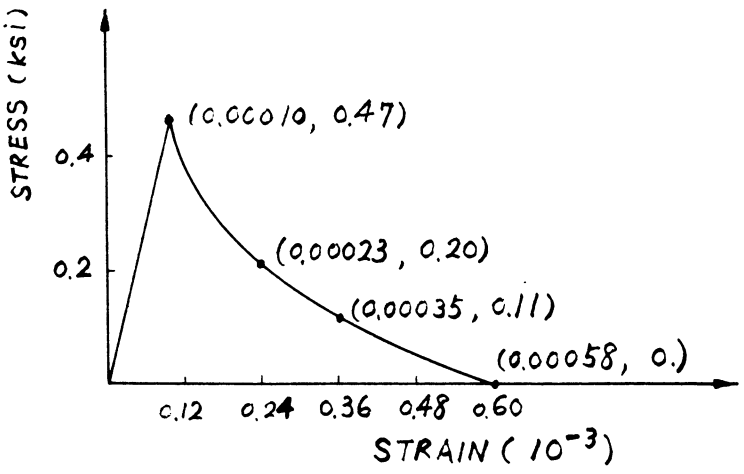

(b) ASSUMED TENSION STIFFENING

FIG 5.12 MATERIAL PROPERTIES FOR EXAMPLE 3

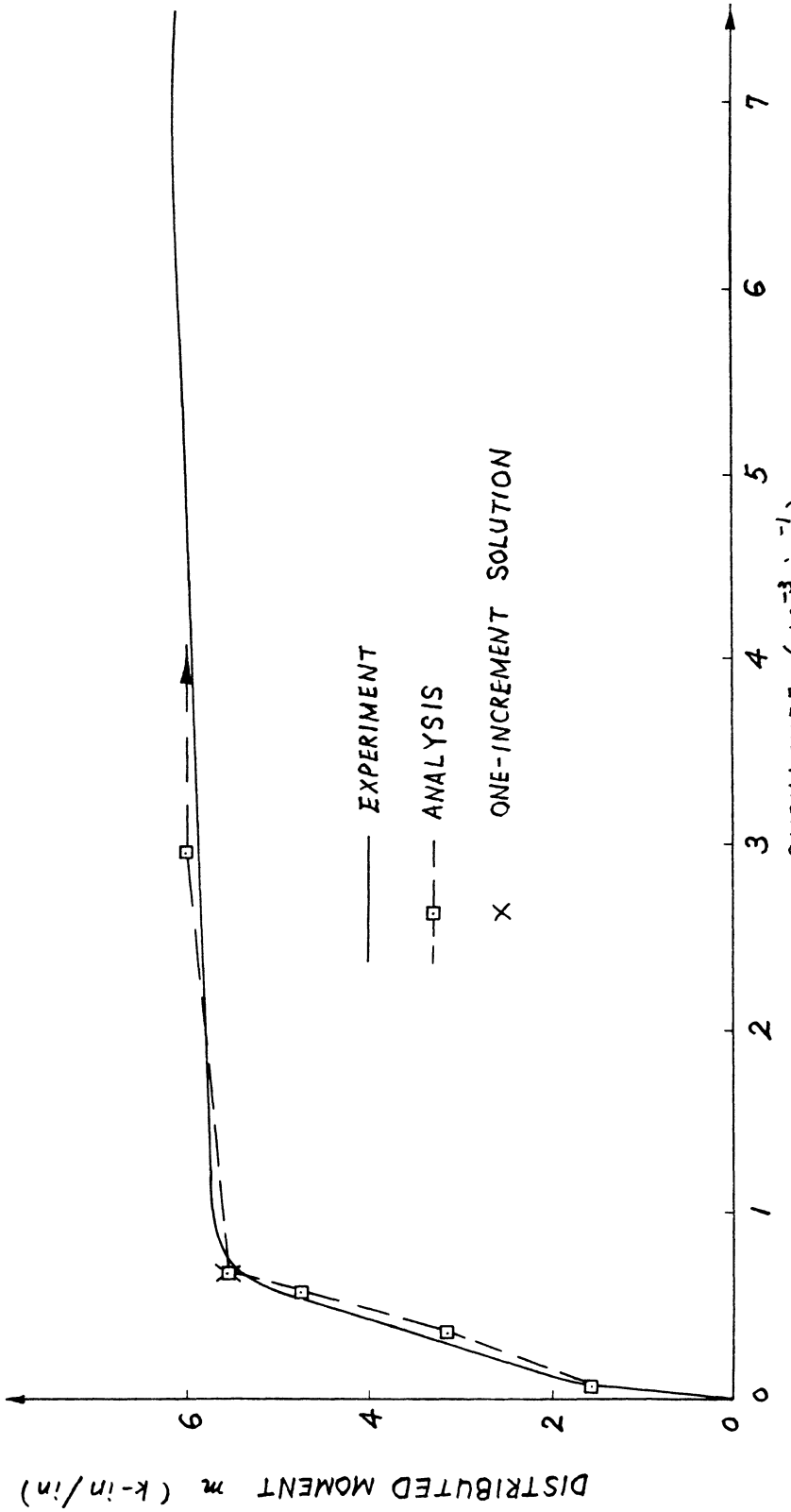

FIG. 5.13 MOMENT-CURVATURE CURVES FOR EXAMPLE 3

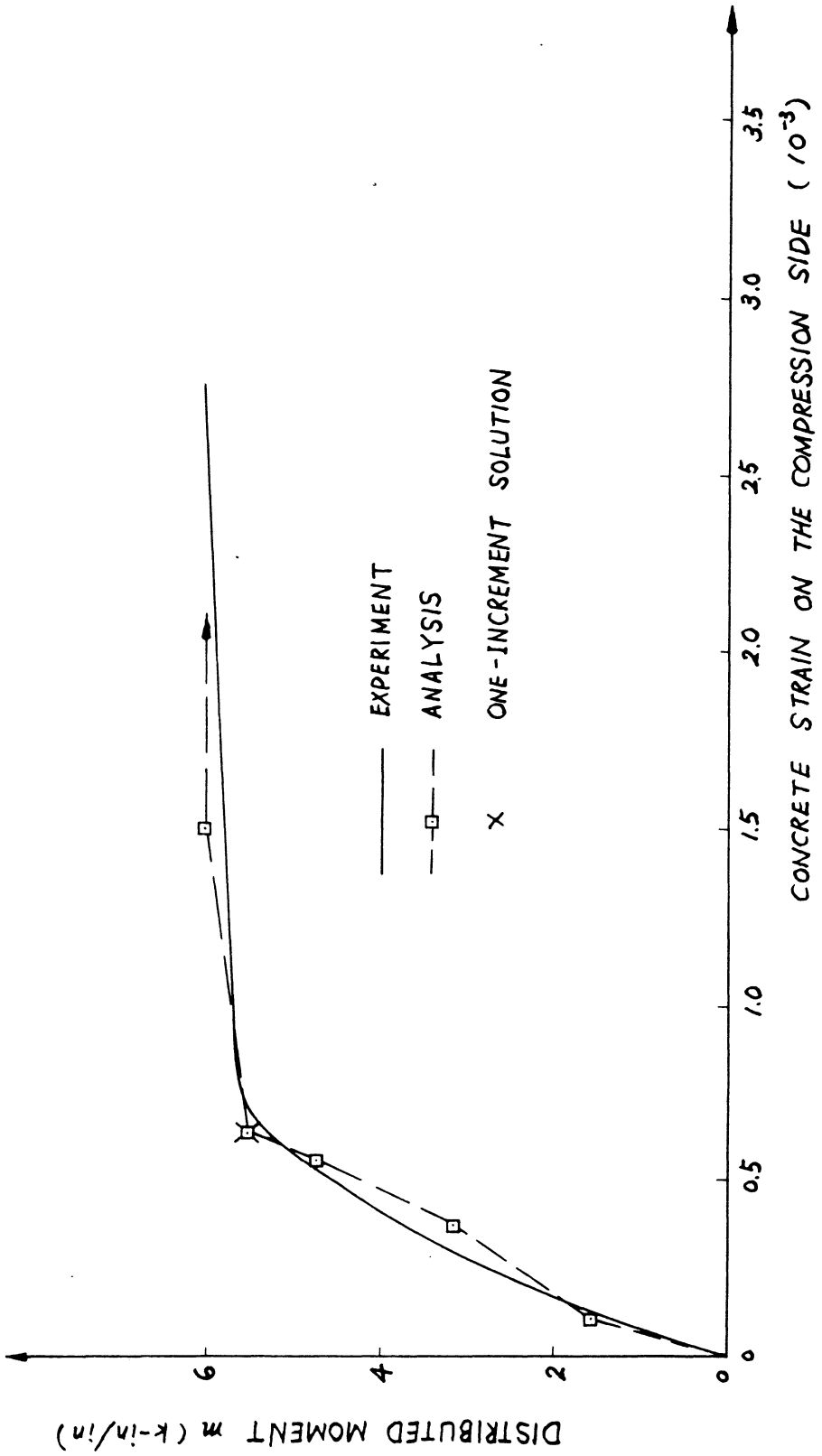

FIG. 5.14 MOMENT-CONCRETE STRAIN PLOTS FOR EXAMPLE 3

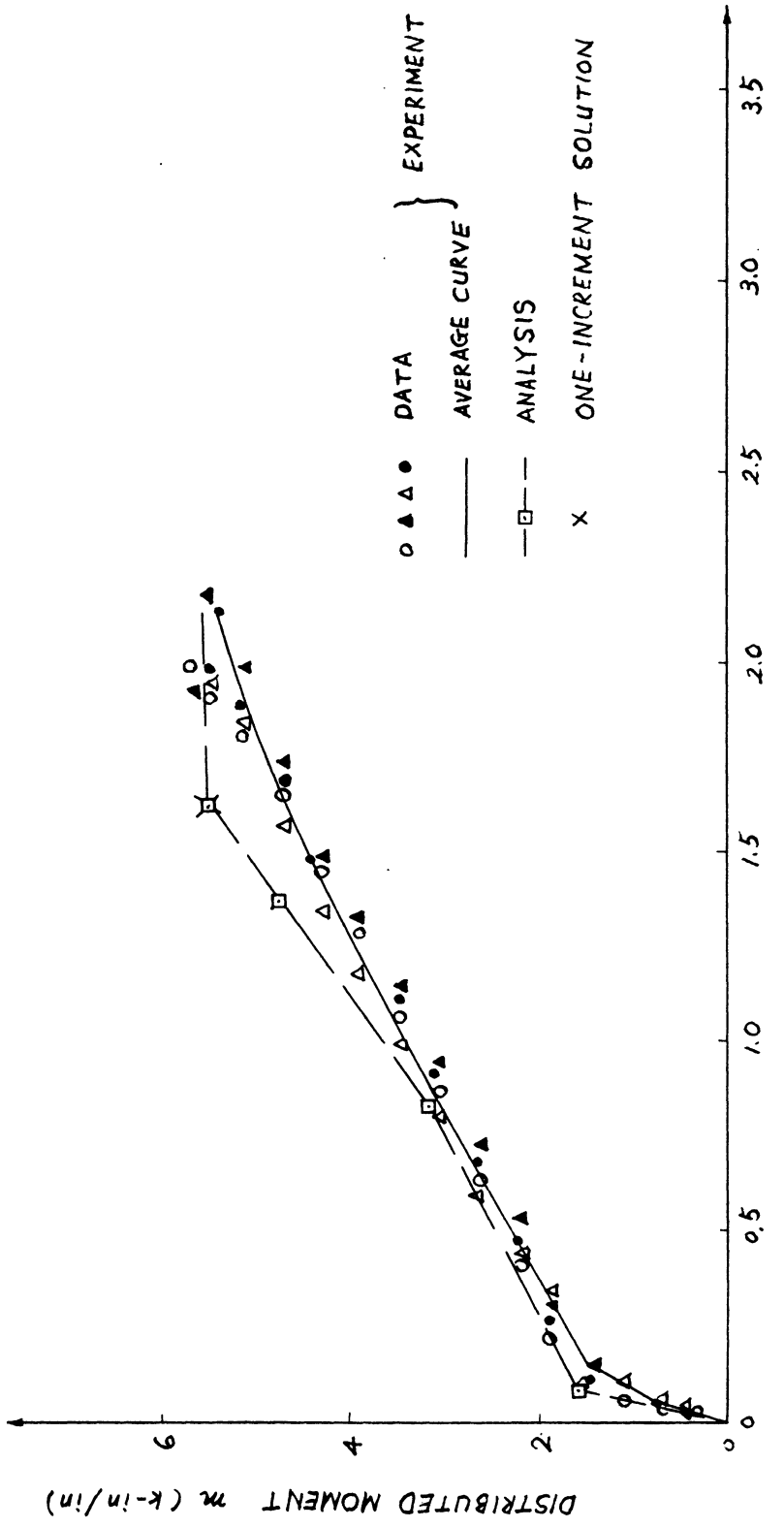

FIG. 5.15 MOMENT-STEEL STRAIN CURVES FOR EXAMPLE 3

cross-section and the actual position, and to the difference between the steel modulus of elasticity used and the actual modulus.

The slab was also analyzed with a single large increment from the proportional load limit. The results were virtually identical to those previously obtained.

5.3.2 Example 4 -- Cardenas Rectangular Slab B7

A rectangular slab also tested by Cardenas and Sozen is selected as another example. The slab is simply supported on two opposite edges and free on the other two edges (Fig. 5.16a). Uniformly distributed moments are applied on the two simply supported edges. The slab is isotropically reinforced with reinforcement oriented at 45° to the edges. This may serve to demonstrate the capability of the proposed method to accomodate arbitrary orientation of the reinforcement.

The dimensions, smeared reinforcement, loading condition, finite element mesh and layer systems are given in Fig. 5.16. Material properties and the assumed tension stiffening relation are given in Fig. 5.17.

Figs. 5.18 through 5.20 show the plots of the moment vs. curvature, concrete strain and steel strain resulting from the experiment and the analysis. The agreement between experimental results and the analytical solution is satisfactory, considering the possible experimental inaccuracy and the finite element approximation. The discrepancy in the higher load range of the moment-concrete strain plots can be attributed to the possible over-estimation of the concrete compressive strength f_c' and the concrete modulus at higher stresses.

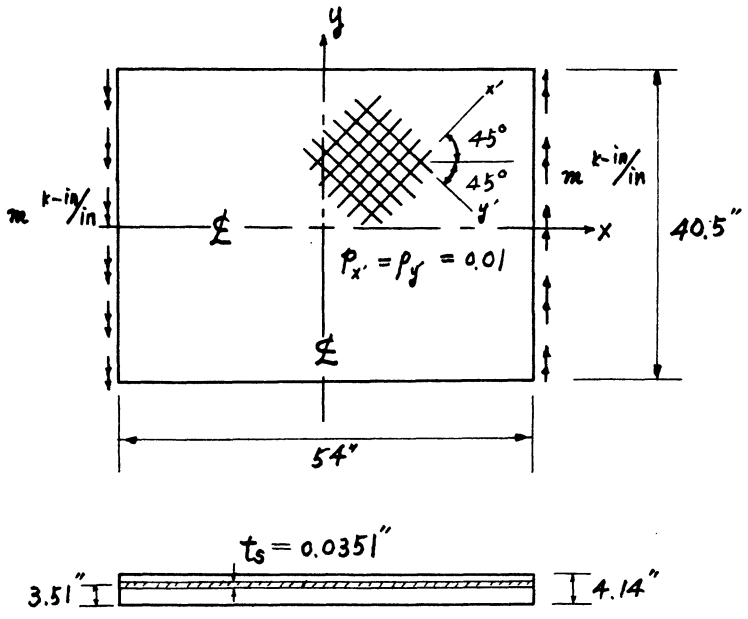

(a) PLAN VIEW AND CROSS-SECTION

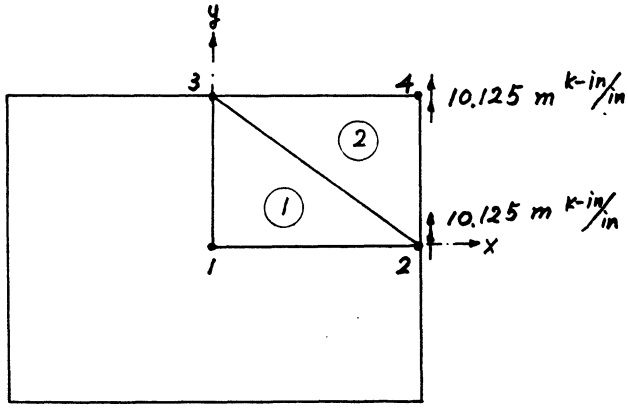

(b) FINITE ELEMENT MESH

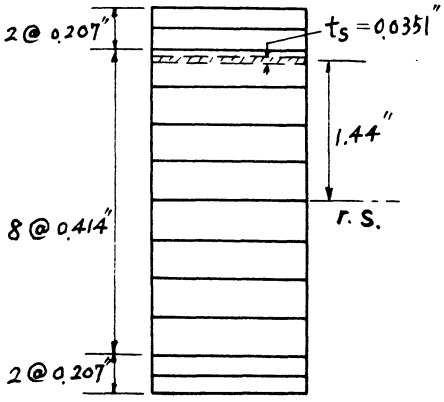

(c) LAYER SYSTEMS

FIG. 5.16 EXAMPLE 4 -- CARDENAS SLAB B7

$E_c = 4330$ ksi $\qquad E_s = 30,000$ ksi

$\nu = 0.15$ $\qquad f_y = 50$ ksi

$f_c' = 5.15$ ksi

$f_t' = 0.502$ ksi

$\epsilon_u = 0.003$

$\alpha = 1.0$

(a) MATERIAL PROPERTIES

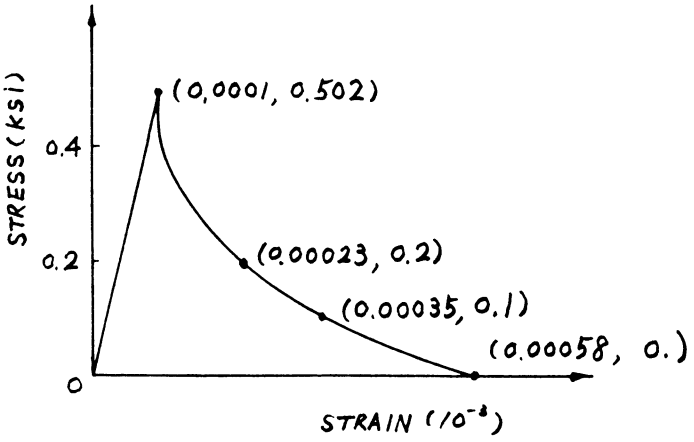

(b) ASSUMED TENSION STIFFENING

FIG. 5.17 MATERIAL PROPERTIES FOR EXAMPLE 4

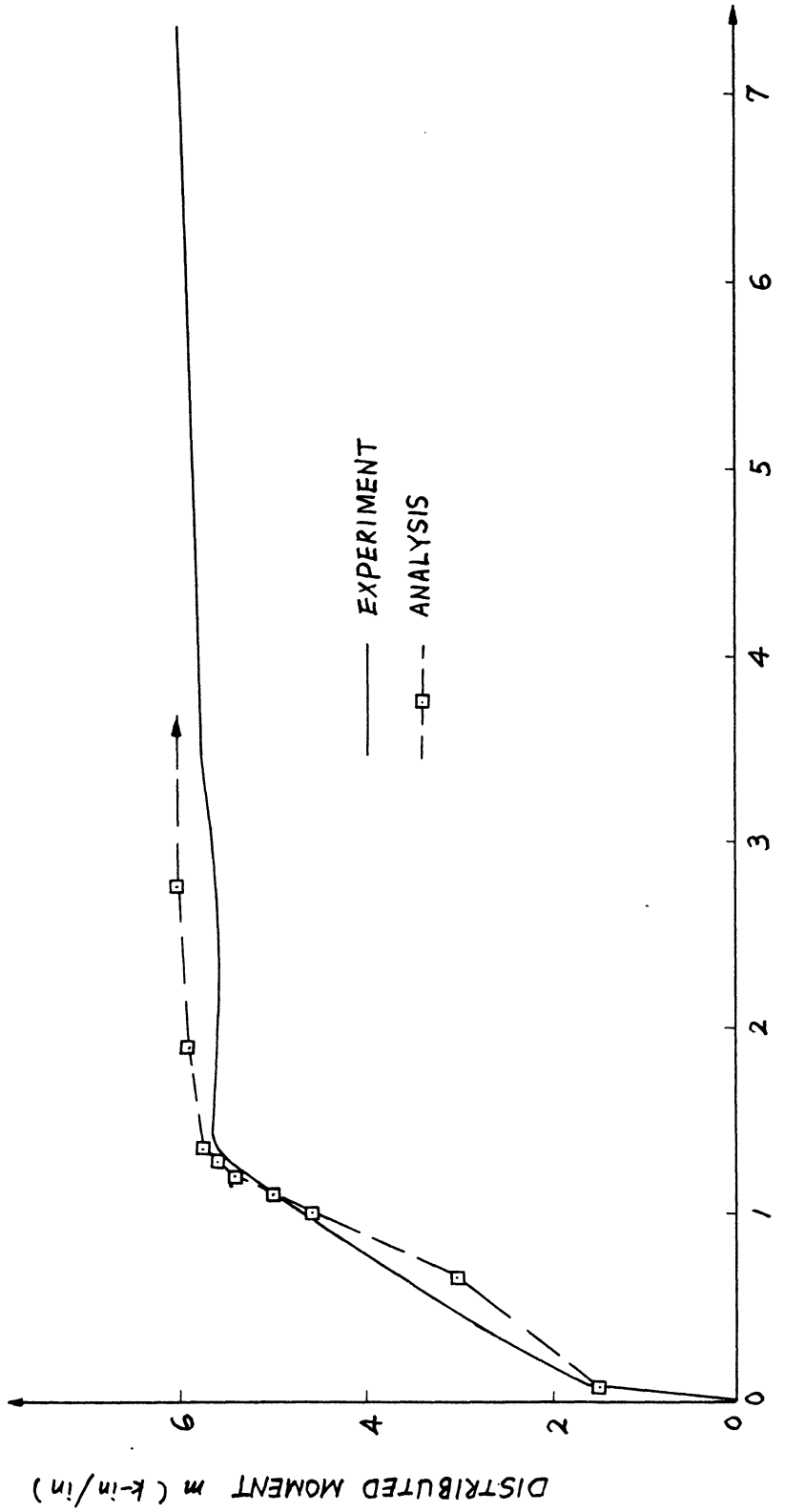

FIG. 5.18 MOMENT-CURVATURE PLOTS FOR EXAMPLE 4

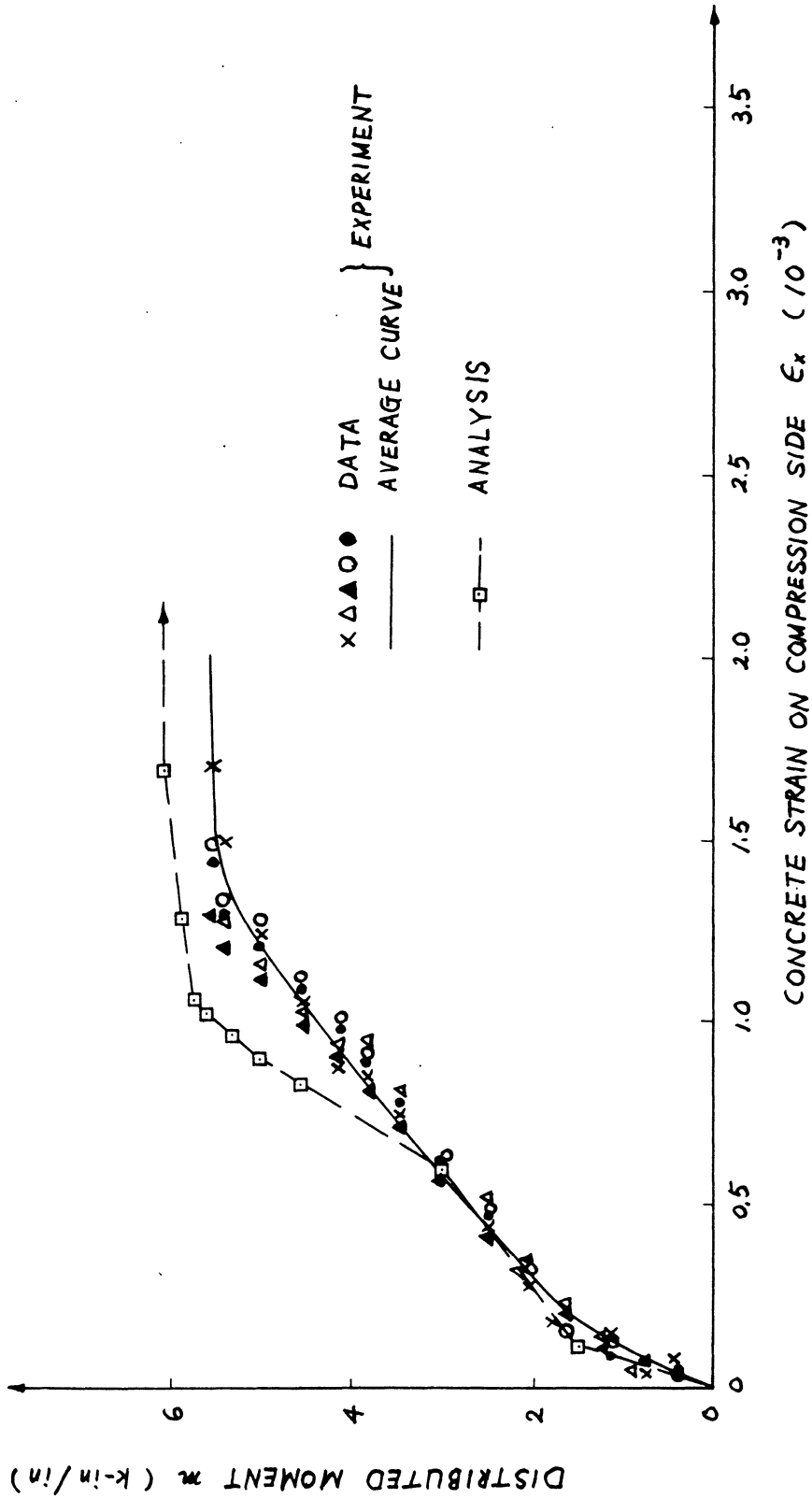

FIG. 5.19 MOMENT-CONCRETE STRAIN PLOTS FOR EXAMPLE 4

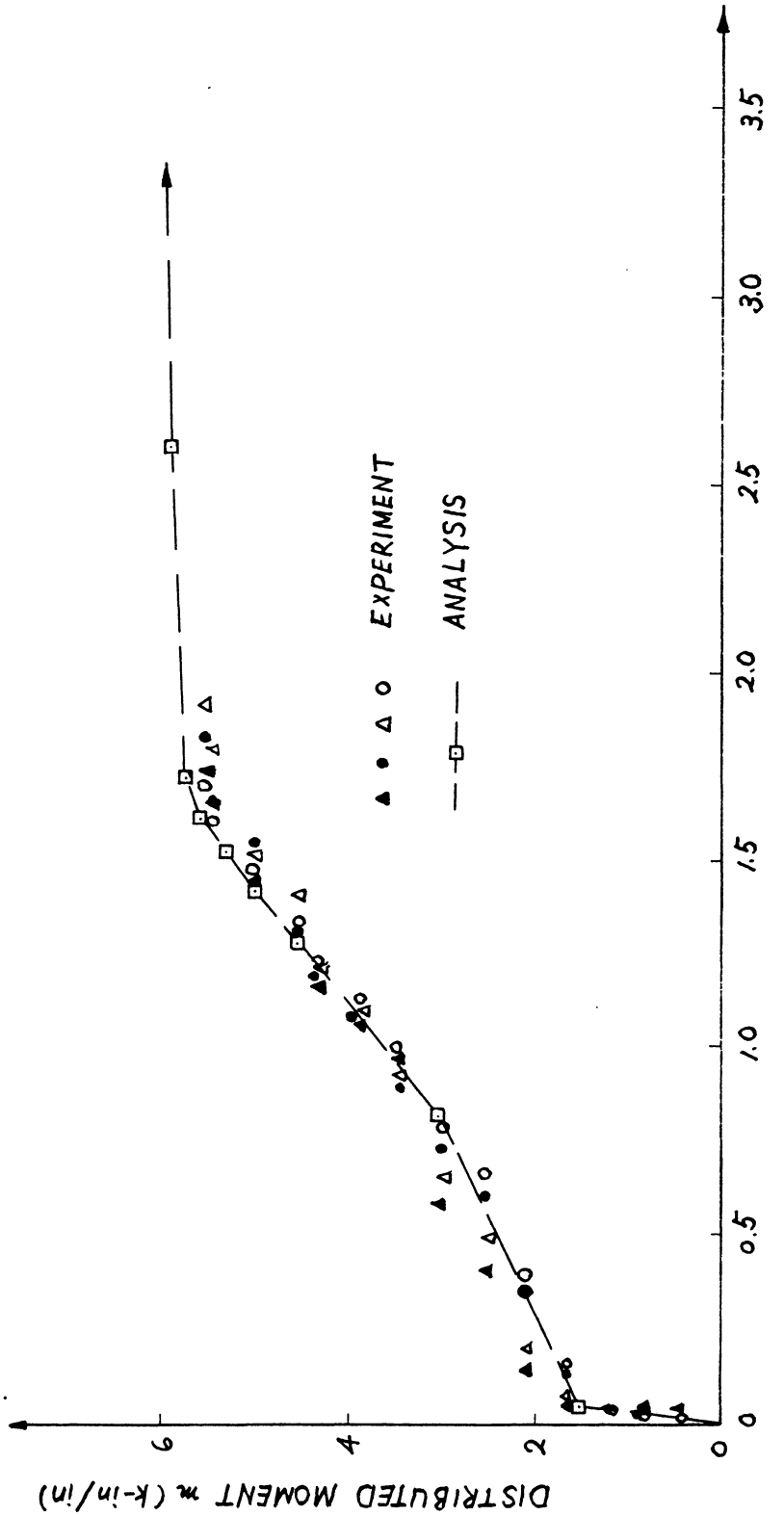

FIG. 5.20 MOMENT-STEEL STRAIN PLOTS FOR EXAMPLE 4

The break in the three analytical curves at 50% of the ultimate load can be smoothed to a certain extent by increasing the tension stiffening effect, noting that the slab is under-reinforced. The sharp increase of the slope on the analytical moment-concrete strain curve (Fig. 5.19) for loads above 50% of the ultimate also indicates a rapid shifting of the neutral surface.

5.3.3 Example 5 -- McNeice Slab

An isotropically reinforced square slab tested by McNeice [5.4] was also analyzed. The slab is simply supported at four corners, and is subjected to a concentrate load at the center (Fig. 5.21). Unlike the last two examples, the slab can serve as a realistically complicated example. Unfortunately, there is a lack of report on the detailed test results, it appears that the slab was not loaded up to failure, and the provided information on the material properties are insufficient. The dimensions, cross-section properties, finite element meshes, layer systems are all shown in Fig. 5.21. The given and assumed material properties are shown in Fig. 5.22.

The resulting load-deflection curves are shown in Fig. 5.23. The slab was first analyzed using 3 x 3 mesh and 0.77 ksi for concrete tensile strength and neglecting the tension stiffening effect. The resulting initial uncracked slope of the obtained load-deflection curve agrees with that of the experimental curve, but the proportional load limit is over-estimated. Therefore the tensile strength of concrete was reduced to 0.55 ksi.

Then the proportional load limit concurs with the experimental result, but there is a general over-estimation of displacement in the post-cracking range. Subsequently the tension stiffening effect was included with an assumed crack unloading curve (Fig. 5.22b). The agreement of the resulting curve with the experiment was considerably improved, but the deflections were under-estimated at the earlier post-cracking stage and over-estimated at the later stage. Finally, the refined 6 x 6 mesh was used, and a smooth load-deflection curve was obtained. The deflections are still over-estimated at the earlier post-cracking stage, but conforms with the experimental curve at the later stage.

The refinement of element mesh has two effects: one is refinement of the displacement field approximation, the other is refinement of the material discretization. In this example, it appears that the improvement of solution is mainly attributed to the latter, because the solution for the uncracked and the early post-cracking ranges is hardly changed by the refinement of mesh. This shows the accuracy of the linear curvature finite element in approximating the true displacement field. In accordance with the previous finding for beams, it can be observed that the influence of the tension stiffening on the post-cracking response is very significant for the under-reinforced slab. It is felt that the analytical solution can be further improved by adjusting the tension stiffening effect. However, there are many factors

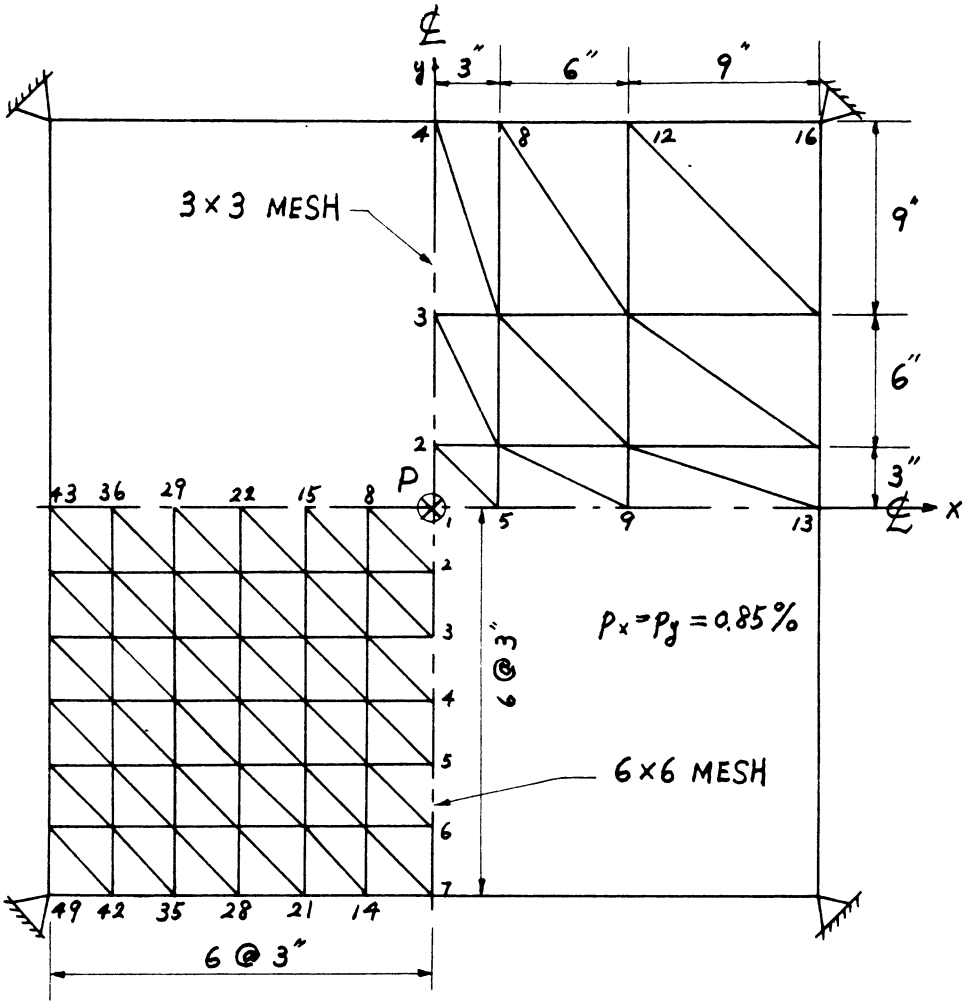

(a) PLAN VIEW AND CROSS-SECTION

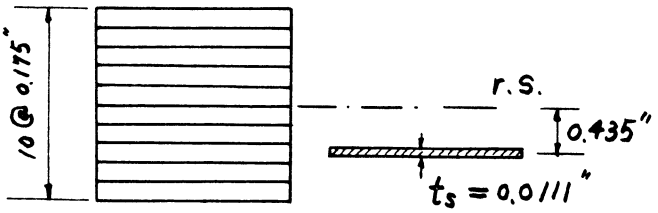

(b) LAYER SYSTEMS

FIG. 5.21 EXAMPLE 5 -- McNEICE SLAB

GIVEN:		ASSUMED:	
E_c =	4150 ksi	f_t' =	0.77 ksi or 0.55 ksi
E_s =	29,000 ksi	ε_u =	0.002
ν =	0.15	f_y =	60 ksi
f_c' =	5.5 ksi	α =	1.0

(a) MATERIAL PROPERTIES

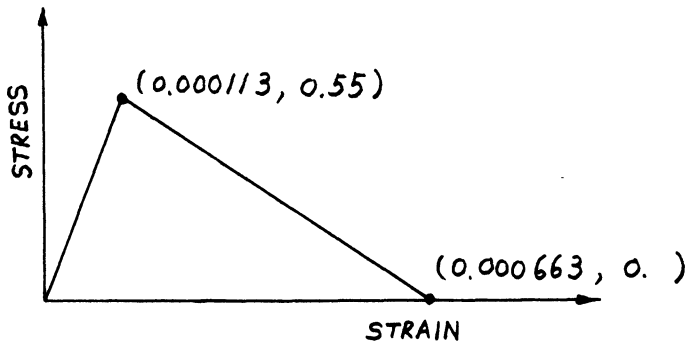

(b) ASSUMED TENSION STIFFENING

FIG. 5.22 MATERIAL PROPERTIES FOR EXAMPLE 5

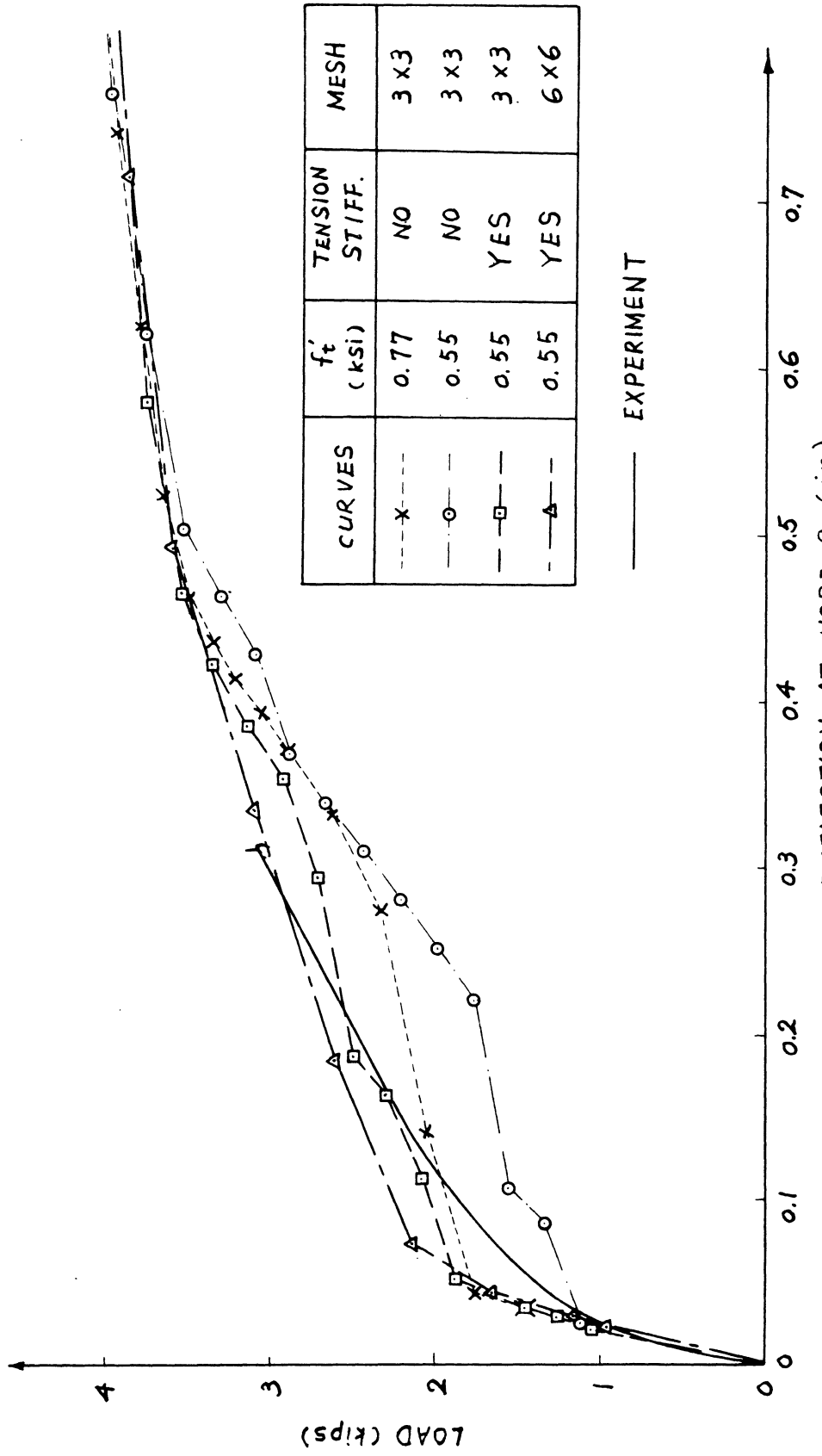

FIG. 5.23 LOAD DEFLECTION CURVES FOR EXAMPLE 5

which may affect the tension stiffening effect, such as the size and spacing of the reinforcing bars, bond characteristics between steel and concrete etc. To be more precise, each concrete layer should have different tension stiffening effect because of their different relative position with respect to the reinforcement. In the absence of the quantitative knowledge of the effect of each individual factor, it seems wiser to make an estimation of the over-all average of the effect for all layers. Further discussion on the tension stiffening effect will be given in Chapter 6. Finally, it is noteworthy that all the analytical curves converge toward the same curve at the ultimate range, which indicates that the ultimate response is not affected by the magnitude of the concrete tensile strength and the tension stiffening effect. In conclusion, the comparison of the analytical solution and the experimental result is satisfactory in the sense that the experimental curve is bounded by the analytical curves with some of the unknown parameters varied.

5.4 Reinforced Concrete Shells

5.4.1 Example 6 -- Hedgren Cylindrical Shell

A microconcrete, 1/8 scale model of cylindrical shell tested by Hedgren [5.4] was selected to study the validity of the method of analysis for shells. The parabolic cylindrical shell (Fig. 5.24) was supported on end diaphragms and had free longitudinal edges. The rise to span ratio was

1:5.3 and the width to length ratio was 1: 1.75. The longitudinal edges of the shell was thickened over a 5 inch horizontal distance, according to the variation

$$h = 0.5 + \left(\frac{y'}{5}\right)^{1.5}$$

where h is the thickness and y' is the horizontal distance. The reinforcement of the shell is shown in Figs. 5.25 and 5.26. The shell was tested under a uniformly distributed normal pressure using a vacuum loading system. In the analysis, the shell was assumed to be simply supported on both ends, and one quadrant of it is divided into a 8 x 8 finite element mesh (Fig. 5.27). The material properties and the assumed tension stiffening effect are given in Fig. 5.28. The concrete was divided, through the thickness, into 8 equal layers and two very thin layers, one on each of the top and bottom surfaces, so that the surface stresses can be approximated by the stresses in the special thin layers. The actual reinforcement, including longitudinal, transverse, diagonal and edge reinforcing bars, was closely approximated by 24 types of steel layer systems. Each type had 4 to 7 steel layers of different smeared thickness and orientation. The cover of the reinforcement was uniformly assumed to be 1/8" to the center of the reinforcing bars. The design load of the shell was 0.52 lb/in^2. In the following presentation of the analytical and experimental results, the applied load will be expressed in terms of a load factor F, which is defined as the ratio of the applied load to the

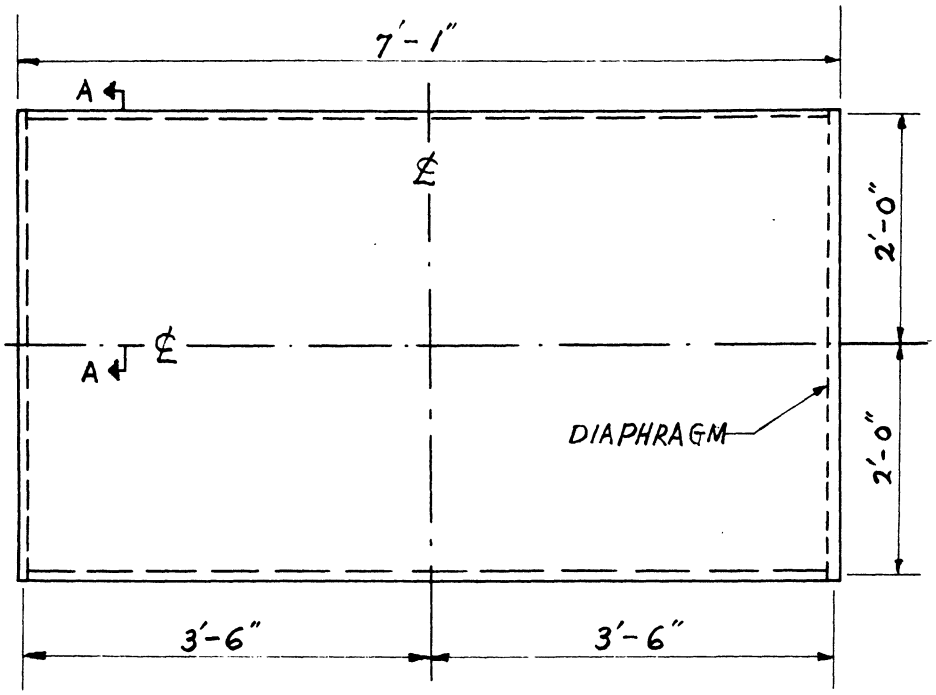

(a) PLAN

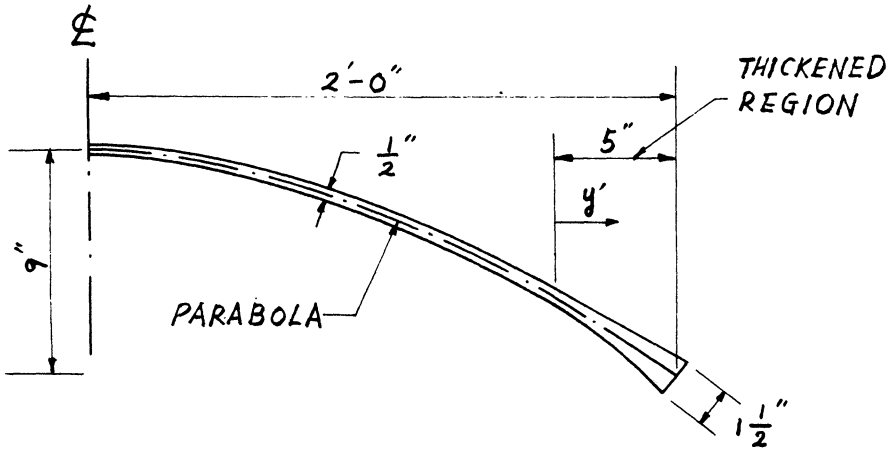

(b) SECTION A-A

FIG. 5.24 EXAMPLE 6 -- HEDGREN CYLINDRICAL SHELL

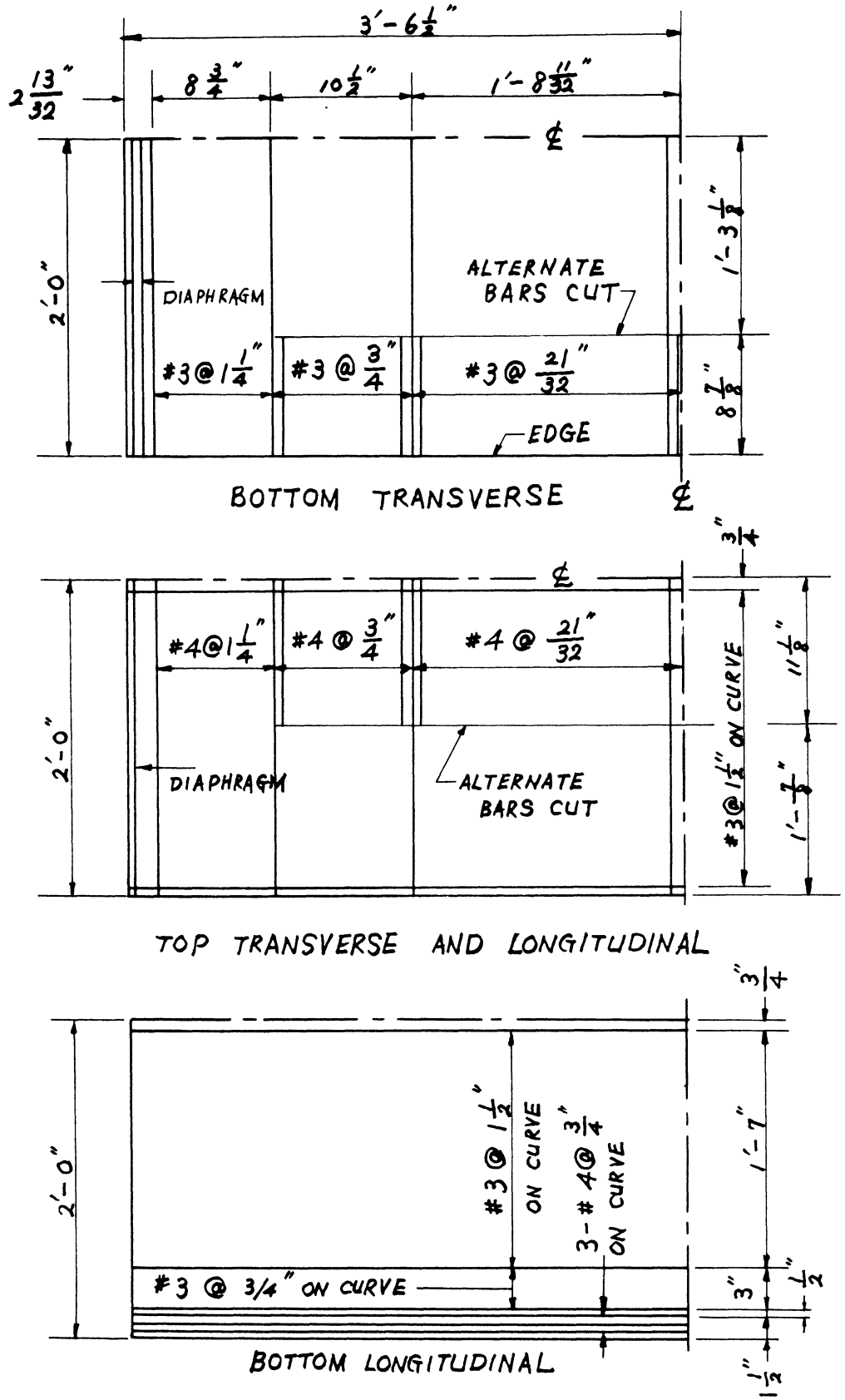

FIG. 5.25 LONGITUDINAL AND TRANSVERSE REINFORCEMENT FOR EXAMPLE 6

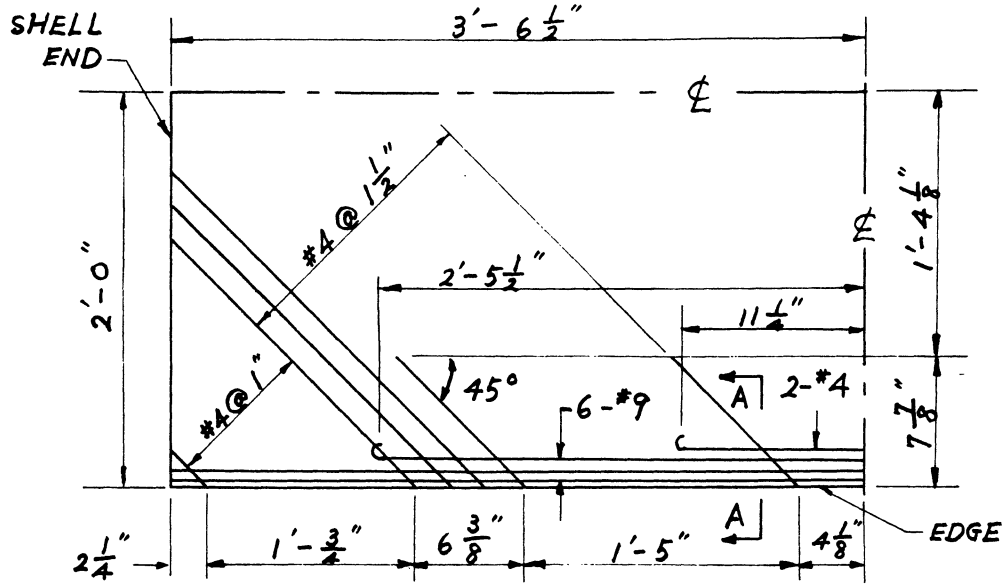

DIAGONAL AND EDGE

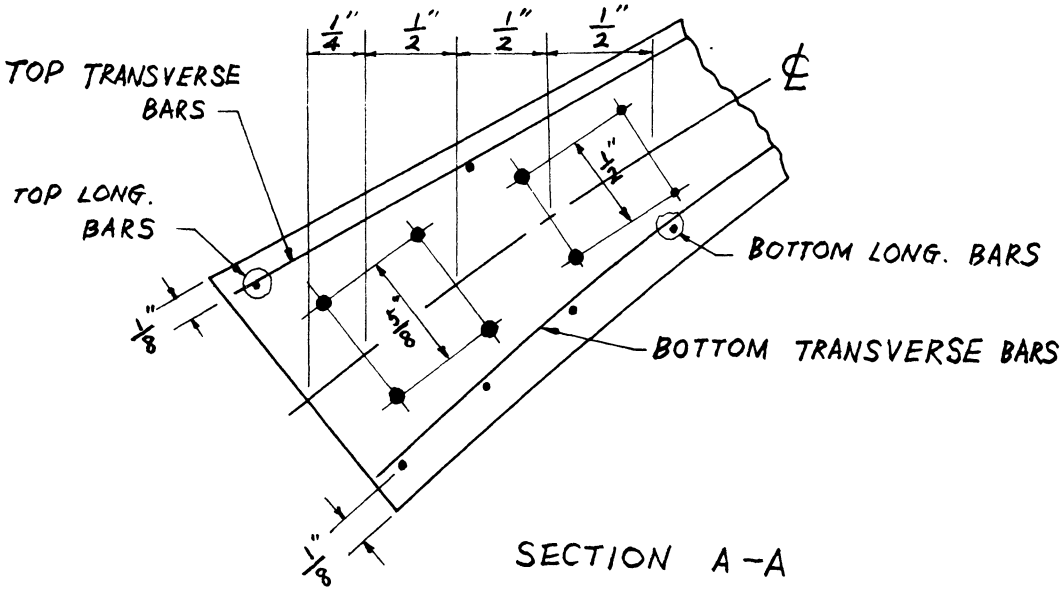

SECTION A-A

FIG. 5.26 DIAGONAL & EDGE REINFORCEMENT FOR EXAMPLE 6

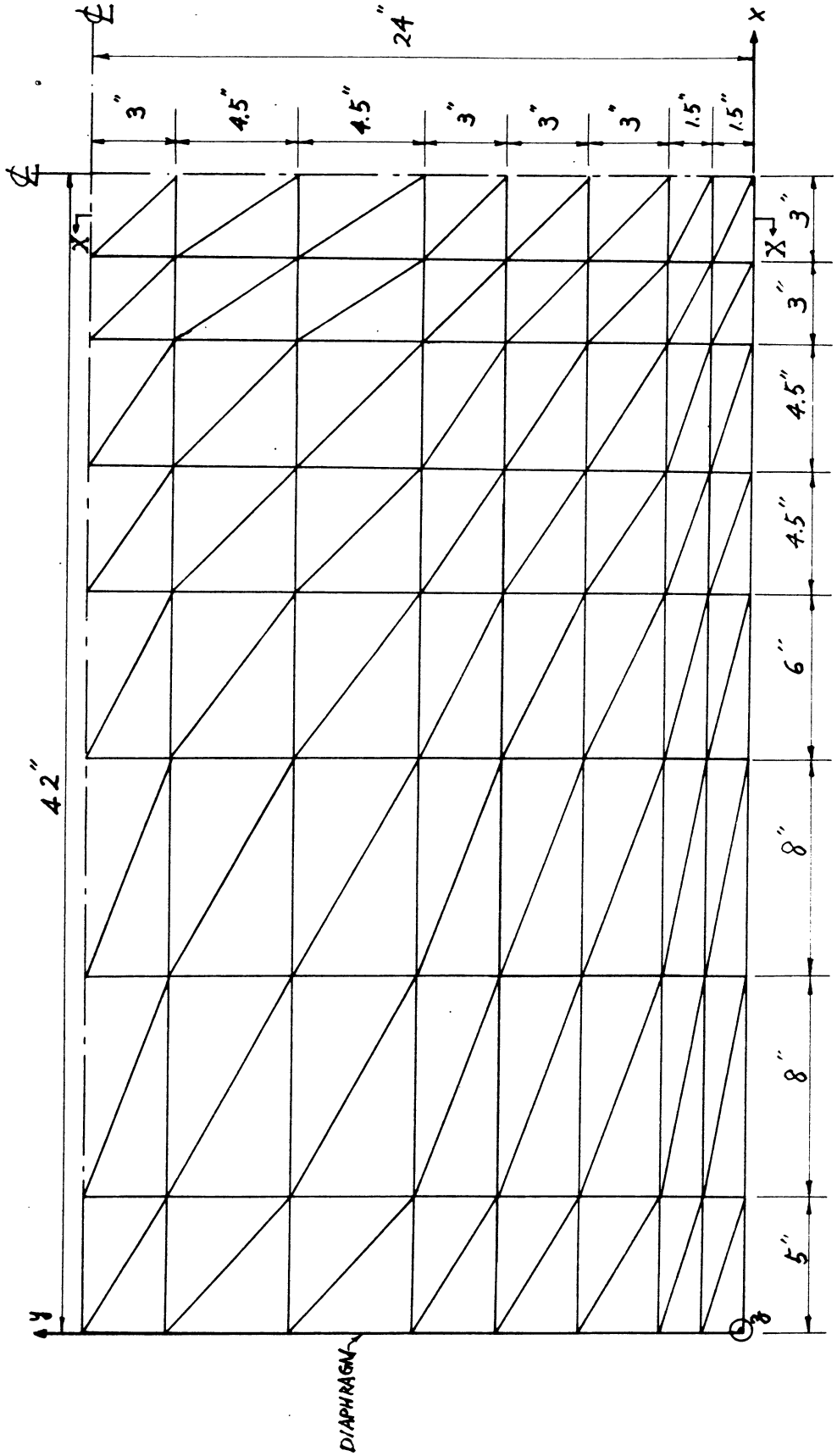

FIG. 5.27 FINITE ELEMENT MESH FOR EXAMPLE 6

REINFORCEMENT :

$E_s = 29,000$ ksi

Designation	Diameter (in)	Area (in^2)	f_y (ksi)	f_{ult} (ksi)
#3	0.048	0.00181	36.7	52.8
#4	0.062	0.00302	31.8	50.0
#9	0.135	0.0143	44.5	60.9

CONCRETE :

$E_c = 3,000$ ksi

$\nu = 0.145$

$f_c' = 4.39$ ksi

$f_t' = 0.696$ ksi

$\alpha = 1.0$ (ASSUMED)

(a) MATERIAL PROPERTIES

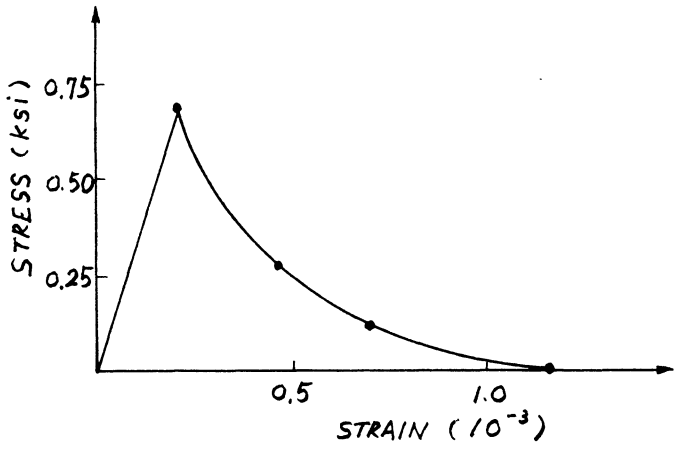

(b) ASSUMED TENSION STIFFENING

FIG. 5.28 MATERIAL PROPERTIES FOR EXAMPLE 6

design load.

The shell was first analyzed using the given yield strength for the reinforcement. A premature failure occurred at F = 2.4 which was far below the experimental ultimate load (Fig. 5.29). The failure mechanism consisted of extensive cracking at the edges and the top of the crown, and yielding of the edge reinforcement and the top lateral reinforcement at the crown.

A rough estimation of the ultimate load carrying capacity of the shell was obtained by computing the T-C couple assuming a beam type failure mechanism. Supposing the tensile region of the shell cracked and all longitudinal edge steel at its yield point, a resultant tensile force of 8.16 kips was found. Neglecting the change of the structural configuration due to finite deflection, the moment arm of the T-C couple was assumed to be 8 inches. An upper bound of the ultimate load factor F = 2.97 was obtained. Even if the secondary longitudinal reinforcement was included, only F = 3.33 could be found. The extra load carrying capacity in the experiment might be derived from the constraint of the monolithically casted end diaphragms, the strain hardening of steel during yielding, and the finite deflection prior to collapse. None of these factors can be accounted for in the present method of analysis.

In order to study the effect of the strain hardening and finite deformation, the shell was reanalyzed using the ultimate

strength of steel as the yield strength. The resulting load-deflection curves are shown in Fig. 5.29. In agreement with the experimental results, an ultimate load factor of 4.0 was obtained. The distribution of normal displacement at the midspan section and along the crown of the shell are shown respectively in Figs. 5.30 and 5.31. It can be seen that the analytical results were consistently more flexible than the experimental results. It should be noted that in the experiment the dial indicators measuring the edge deflections became out of contact with the shell for loading beyond F = 2.4. Therefore the experimental curve for the edge deflection in Fig. 5.29 was completed by extrapolation of the experimental deflection profile in Fig. 5.30. For F = 4.0 the analysis gave a vertical uplift of 0.33 in. at the crown and a downward vertical displacement of 2.69 in. at the edge at the midspan cross-section. If the effect of the finite deflection is included in the estimation of the ultimate load, the moment arm of the T-C couple could be increased to 11 in. With the original given yield strength, an upper bound of the ultimate load factor F = 4.08, or F = 4.58 including the secondary longitudinal reinforcement could be obtained. It was concluded that in this particular example there was considerable stiffening effect due to the finite deflection of the shell. This suggests that for certain cases of flexible shells the inclusion of the geometric non-linear effect should be considered in computing ultimate strengths.

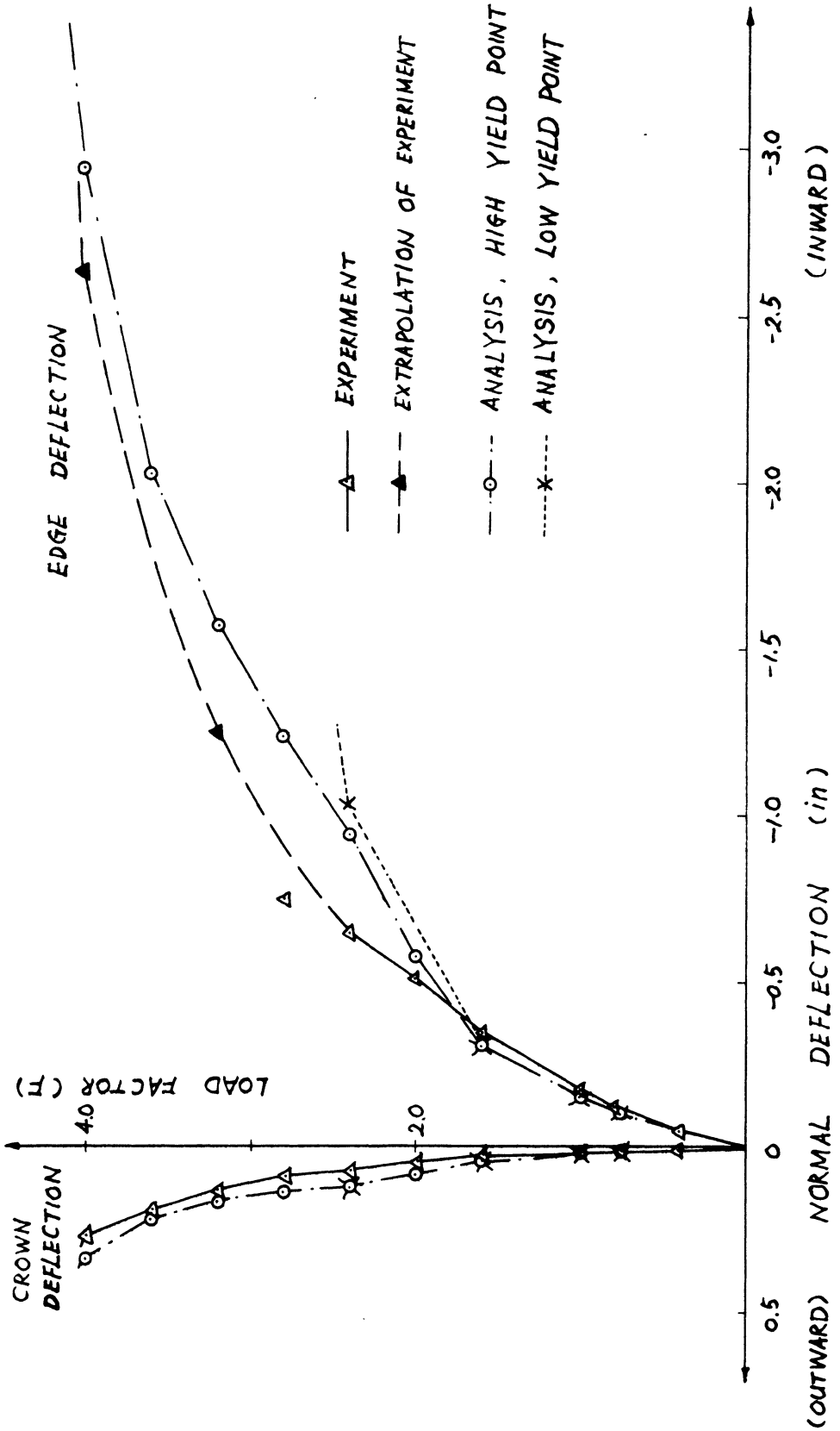

FIG. 5.29 LOAD-DEFLECTION CURVES FOR EXAMPLE 6

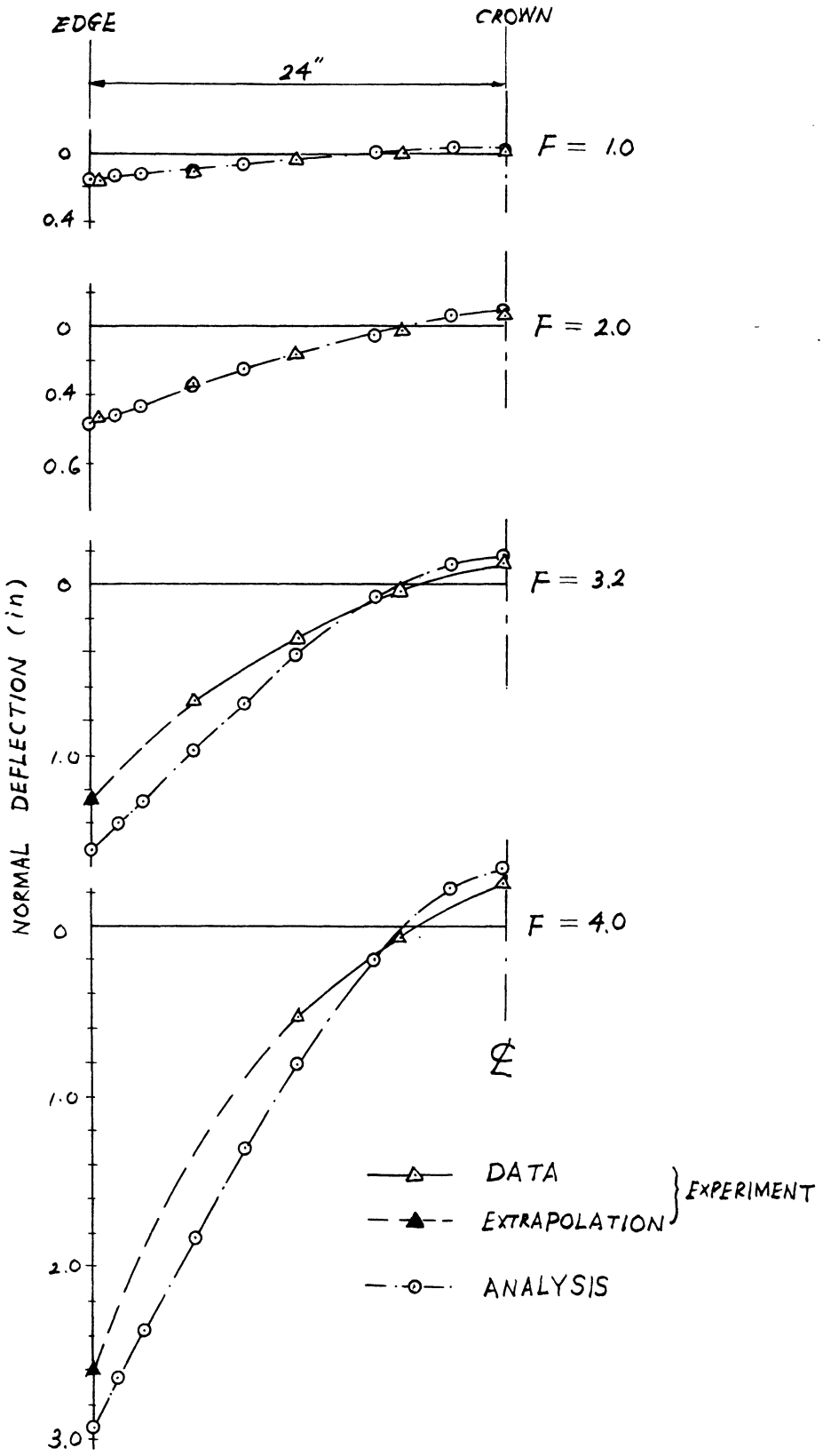

FIG. 5.30 NORMAL DEFLECTION AT MIDSPAN SECTION FOR EXAMPLE 6

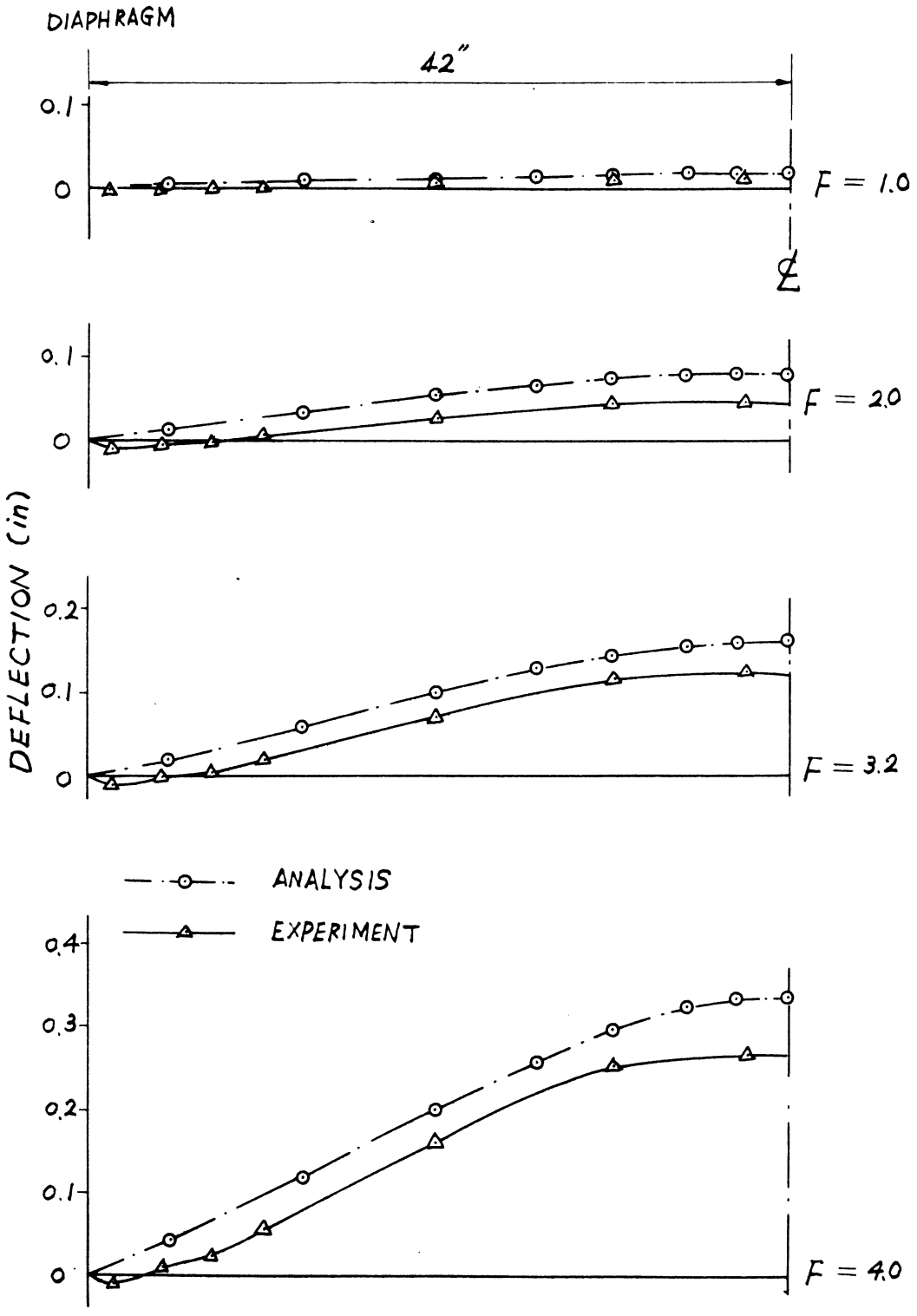

FIG. 5.31 LONGITUDINAL VARIATION OF NORMAL DEFLECTION ALONG THE CROWN FOR EXAMPLE 6

Despite the above mentioned differences, it was considered informative to discuss some of the internal concrete and steel stresses obtained from the analysis. Figs. 5.32 and 5.33 show the longitudinal distribution of longitudinal stresses in the edge reinforcement and the crown concrete respectively for different load levels. It was observed that there was little longitudinal bending action taking place along the edges, and virtually none at the ultimate stage. On the other hand, there was considerable longitudinal bending action along the crown of the shell throughout all load levels. Fig. 5.34 shows the load vs. longitudinal stresses curves for the edge reinforcement and the crown concrete at the midspan.

Shown in Figs. 5.35 and 5.36 are the distribution of transverse steel and concrete stresses at the midspan section. The yielding of the top steel and the crack propagation of the concrete can be observed from these figures. It is of interest to note that there was a stress reversal in the bottom steel after the cracks penetrated deep into the thickness. The validity of the solution, however, was not affected, because the reversal occurred well within the elastic limit. Figure 5.37 shows the load vs. transverse stresses curves for the steel and concrete at the crown of midspan.

Figures 5.38 and 5.39 show the crack patterns on the top and bottom surfaces respectively at the ultimate load. Transverse cracking occurred in all the elements along the

edges, a negative longitudinal yield line formed at the crown, and a positive yield line initiated near the edge. The trend and direction of the crack patterns agreed with the experimental results.

To test the self-consistency of the analytical solution, a static check was made at a cross-section near the midspan, section X-X in Fig. 5.27, for F = 4.0. The internal stresses were integrated. The resultant tensile force was compared with the resultant compressive force, and the resultant internal resisting moment was checked with the external moment due to the applied load. The calculation can be summarized as follows.

Forces:	Tensile	7.62 kips	} should be equal
	Compressive	8.08 kips	
	Error	5.7%	
Moments:	Internal	45.23 in-k	} should be equal
	External	45.95 in-k	
	Error	1.6%	

A similar check was also made for F = 2.4. The results were equally satisfactory.

In conclusion, the analytical solution agreed with the experimental results at the linear and the early nonlinear stages. For the later nonlinear and ultimate stages the analysis gave a more flexible and weaker solution because of the inability to include the geometric nonlinearity.

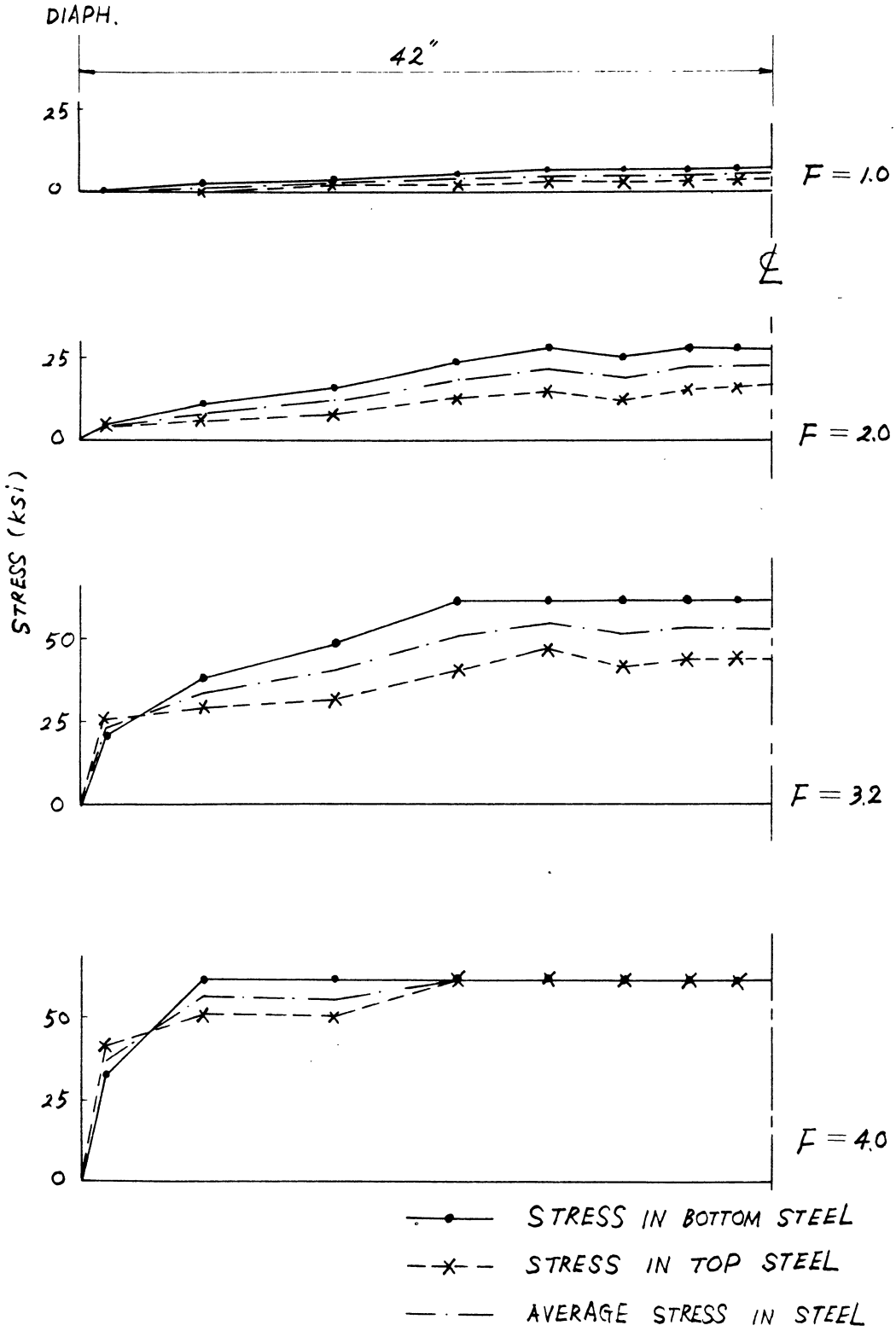

FIG. 5.32 LONGITUDINAL VARIATION OF LONGITUDINAL STRESS IN THE MAIN EDGE REINFORCEMENT FOR EXAMPLE 6

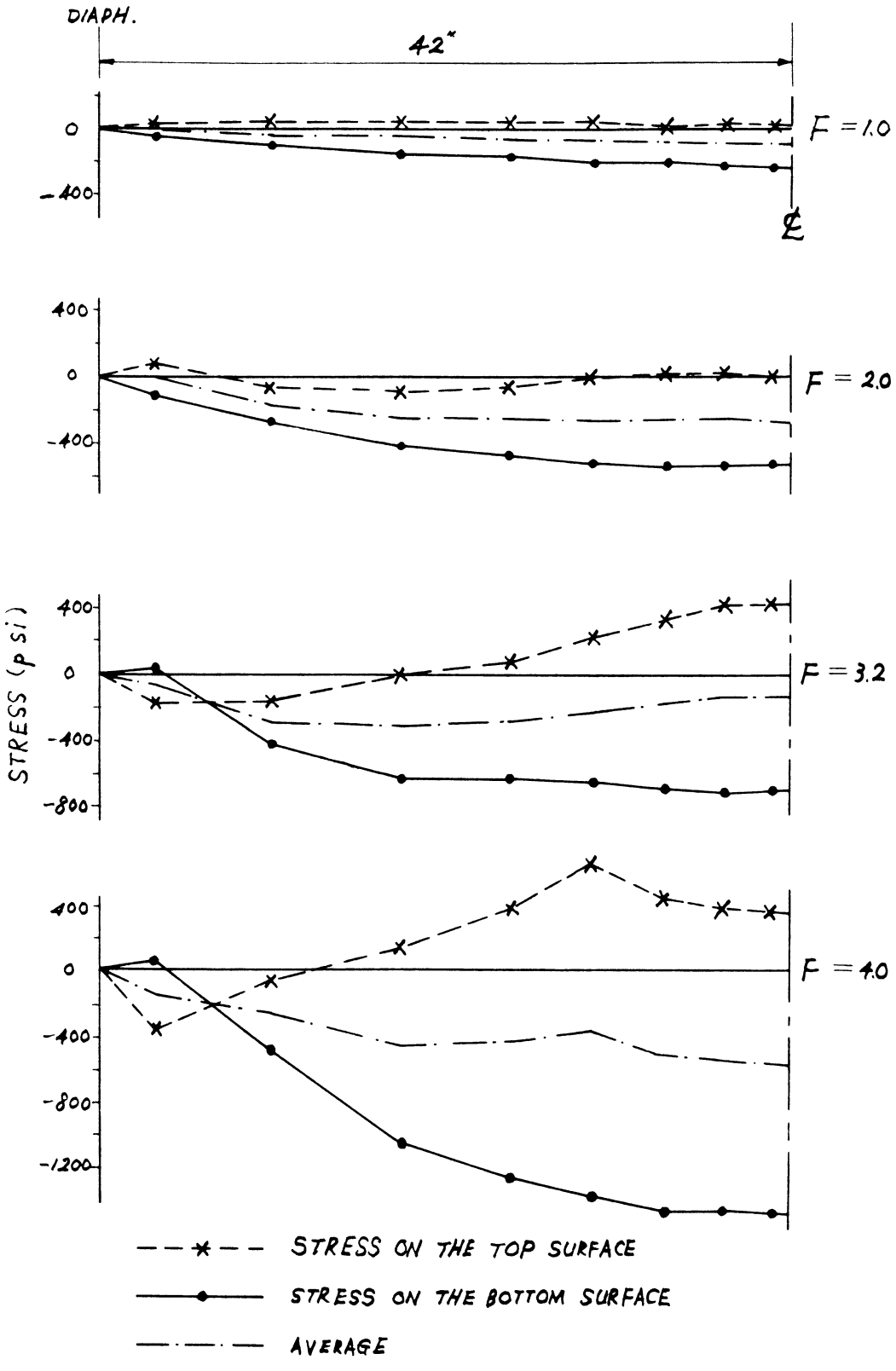

FIG. 5.33 LONGITUDINAL VARIATION OF LONGITUDINAL CONCRETE STRESSES ALONG THE CROWN FOR EXAMPLE 6

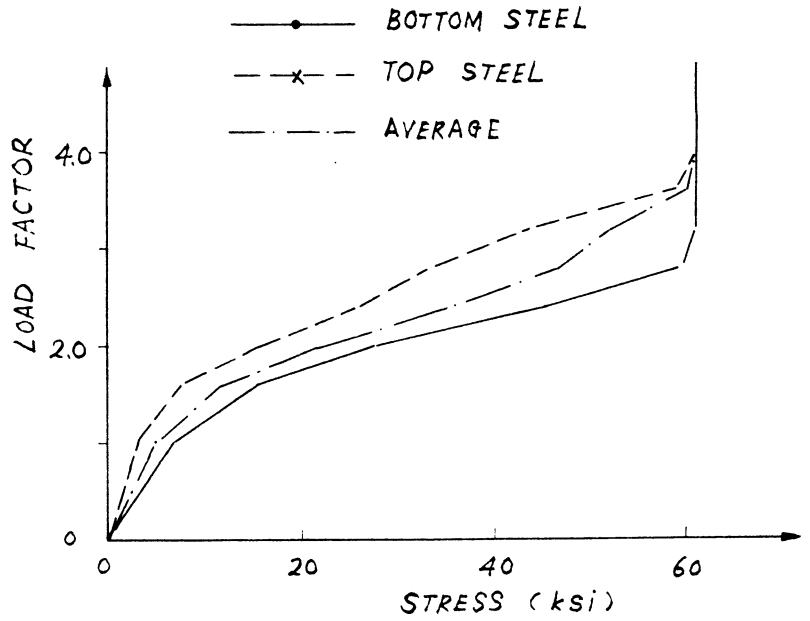

(a) STRESSES IN THE EDGE REINFORCEMENT AT MIDSPAN

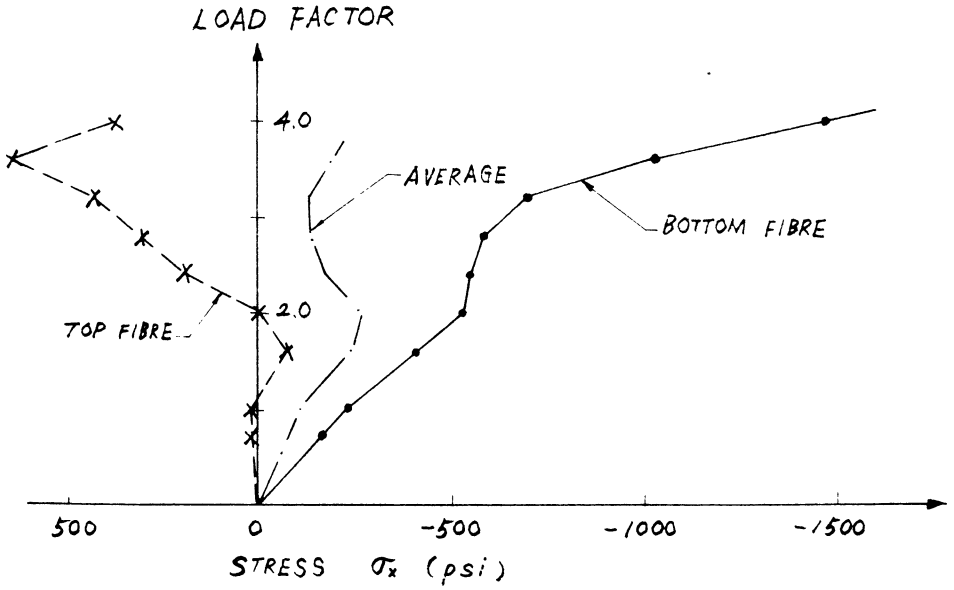

(b) CONCRETE STRESSES AT THE CENTER OF SHELL

FIG. 5.34 LONGITUDINAL STEEL & CONCRETE STRESSES FOR EXAMPLE 6

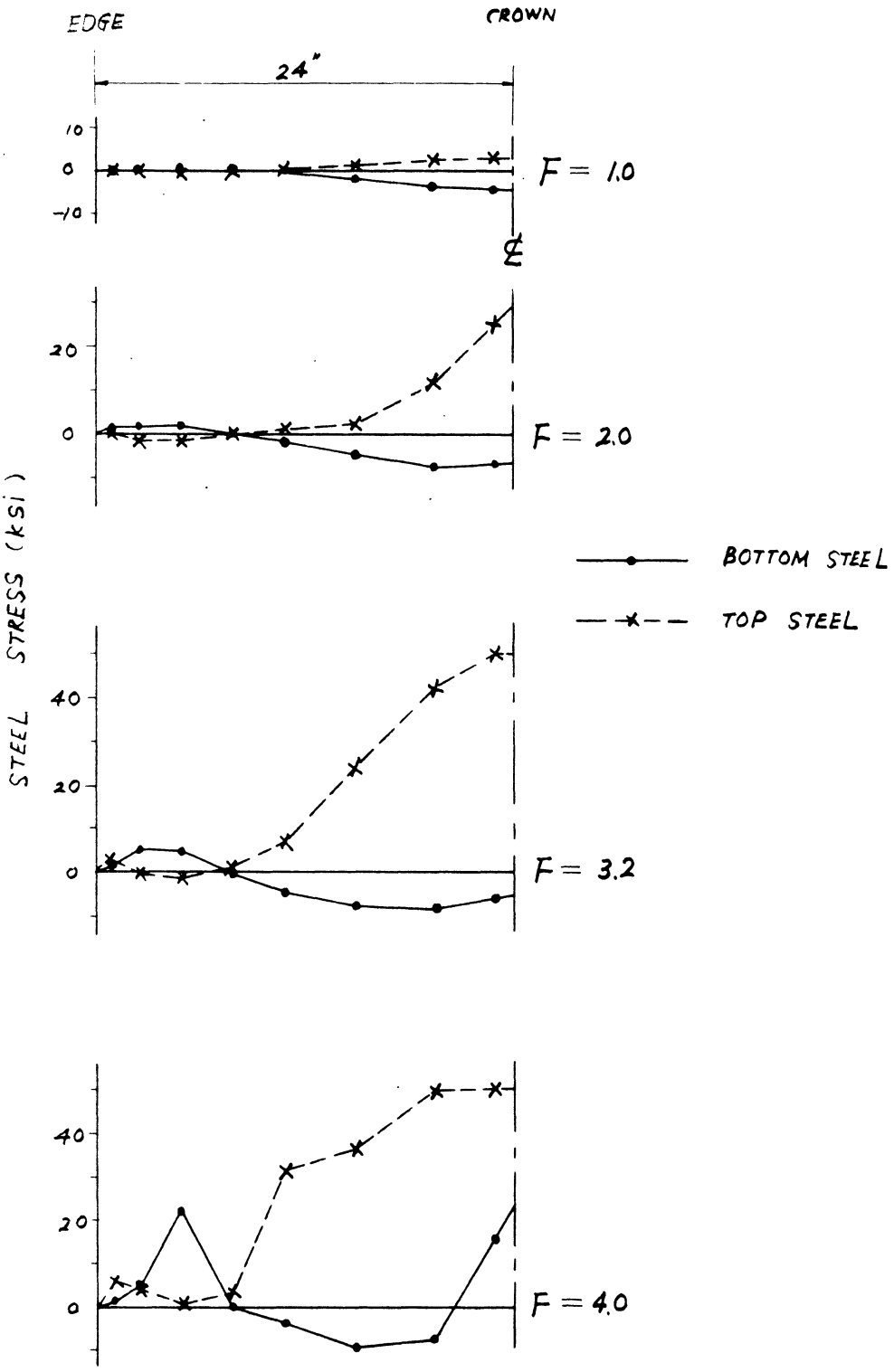

FIG. 5.35 STRESSES IN TRANSVERSE REINFORCEMENT AT MIDSPAN SECTION FOR EXAMPLE 6

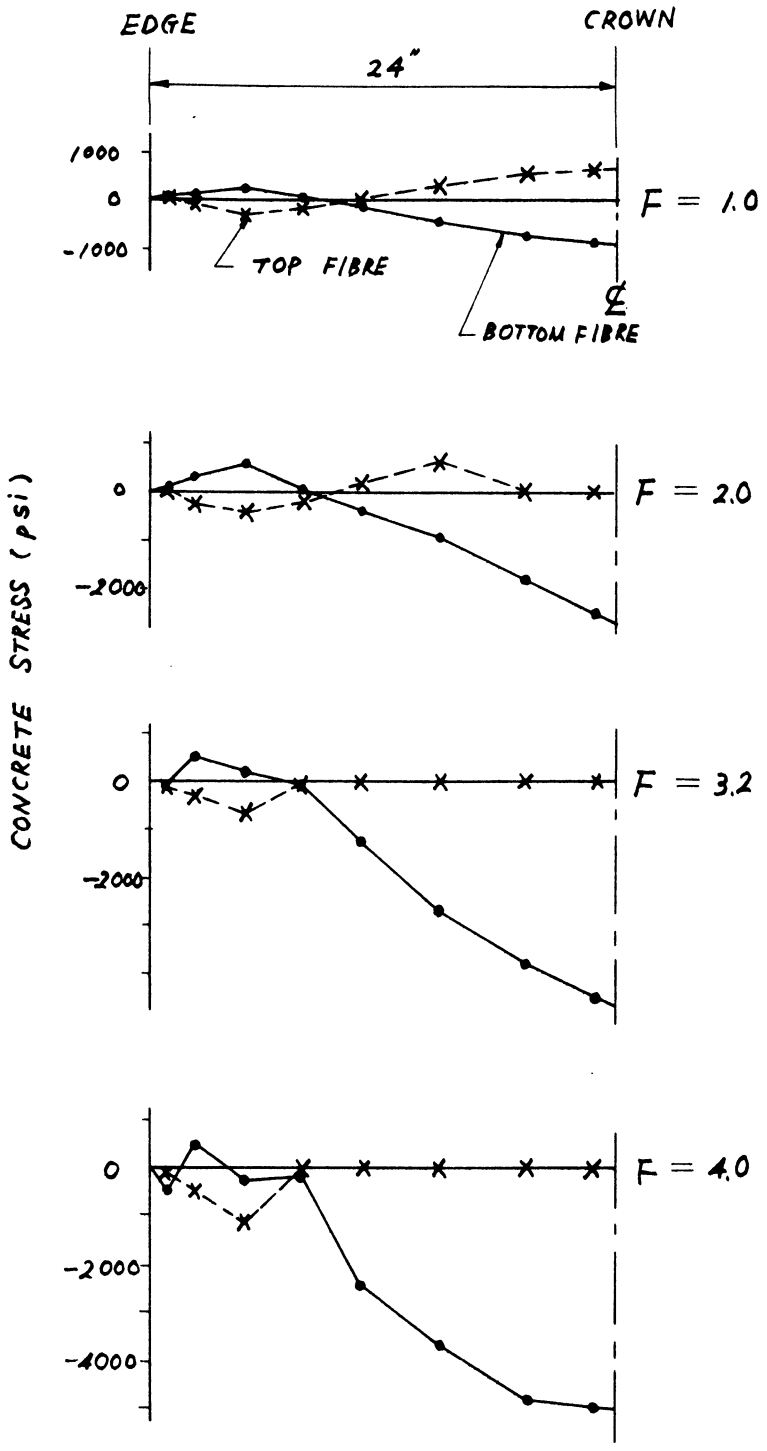

FIG. 5.36 TRANSVERSE CONCRETE STRESSES AT MIDSPAN SECTION FOR EXAMPLE 6

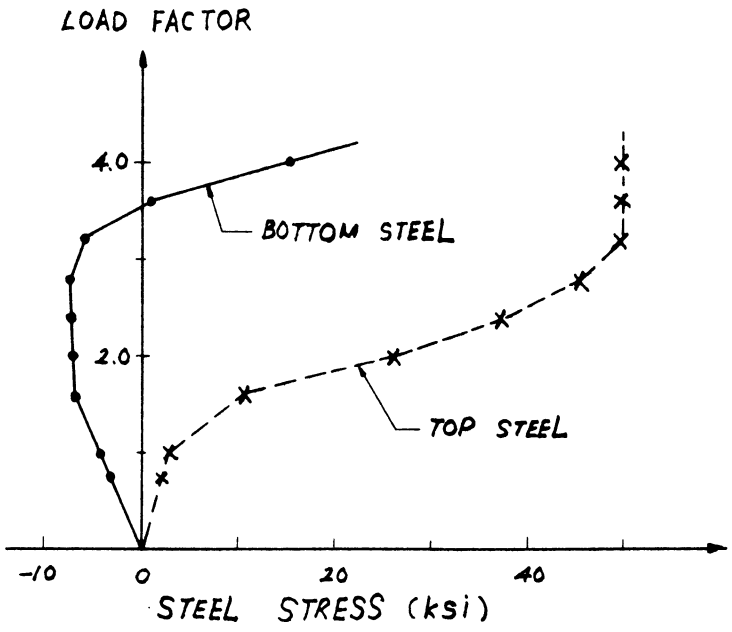

(a) TRANSVERSE STEEL STRESSES AT THE CROWN OF MIDSPAN SECTION

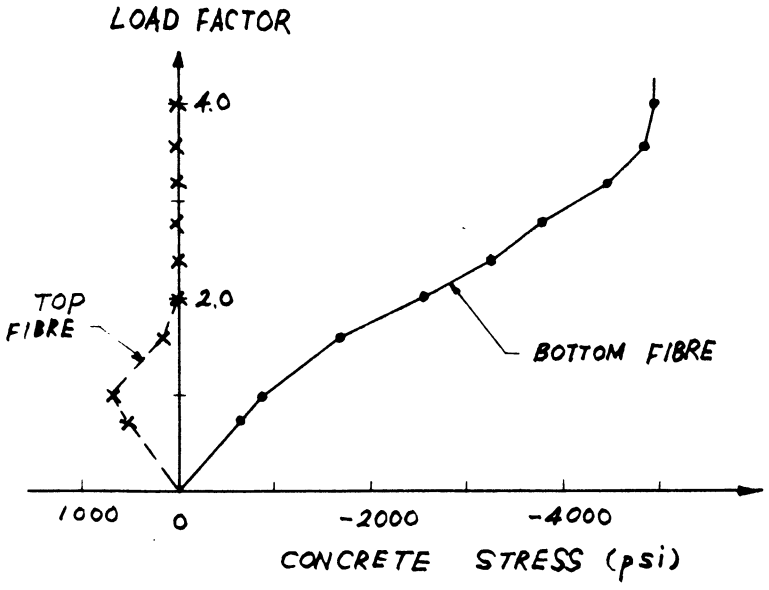

(b) TRANSVERSE CONCRETE STRESSES AT THE CROWN OF MIDSPAN SECTION

FIG. 5.37 TRANSVERSE STEEL & CONCRETE STRESSES FOR EXAMPLE 6

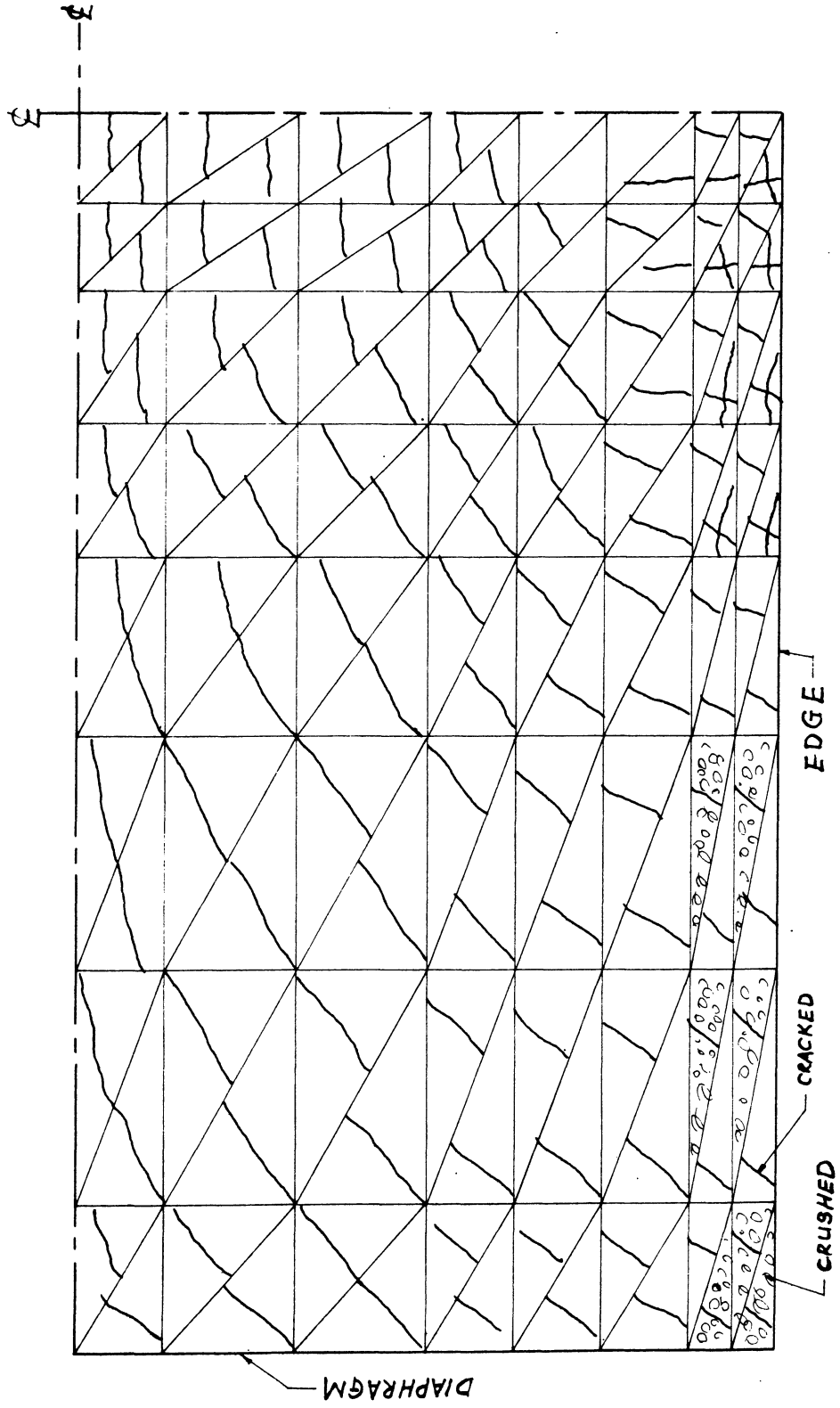

FIG. 5.38 CRACK PATTERN ON THE TOP SURFACE FOR F = 4.0

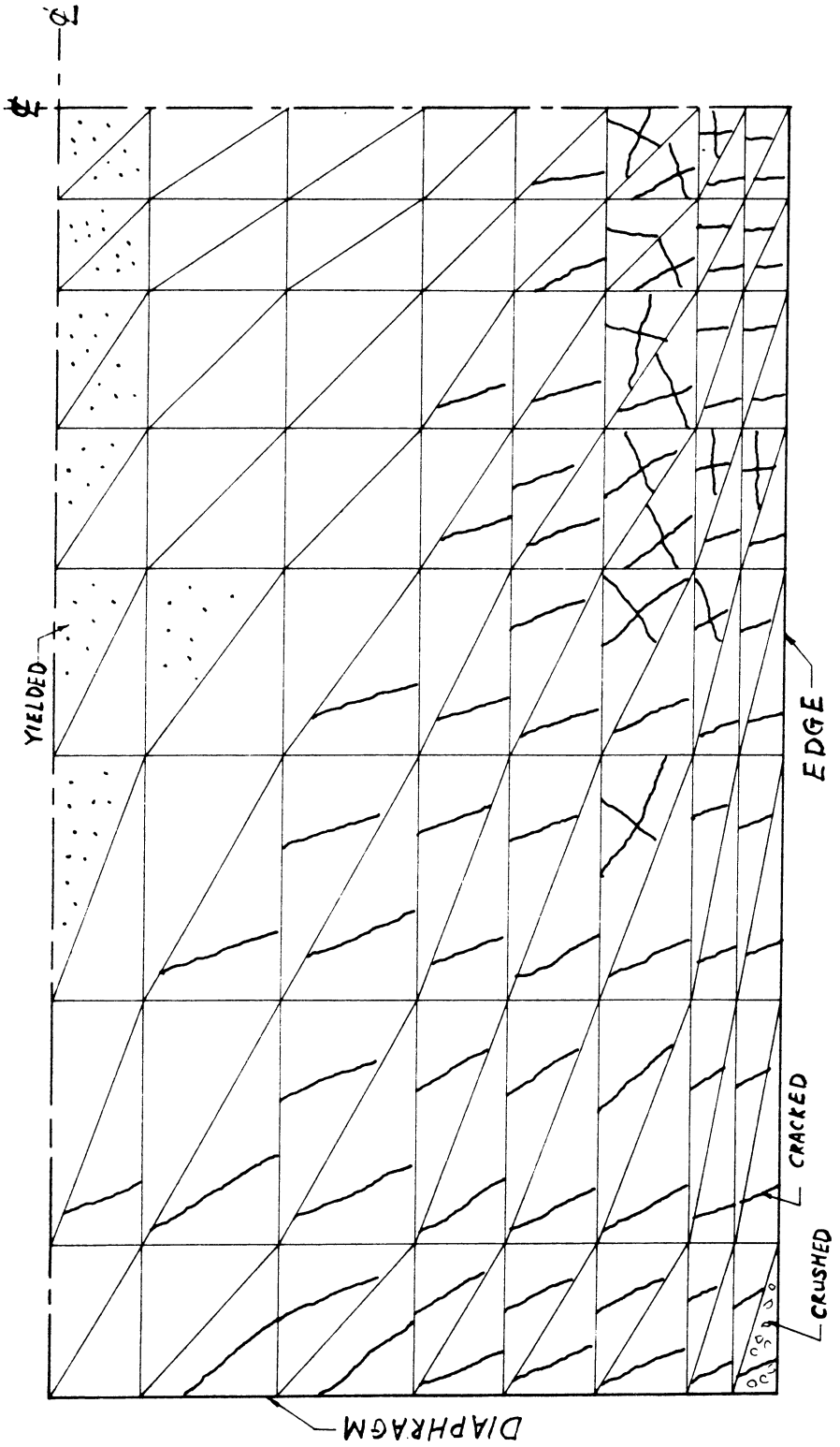

FIG. 5.39 CRACK PATTERN ON THE BOTTOM SURFACE FOR F = 4.0

5.4.2 Example 7 -- Hyperbolic Paraboloid Shell

A doubly curved hyperbolic paraboloid shell, 80 ft. square in plan, with its edge beams completely fixed into abutments at the low points and the high points free to deflect, was designed for dead weight of the shell plus the edge beams and a live load of 20 lbs. per square foot of horizontal projection (Fig. 5.40). A constant thickness of 4 in. was adopted for the entire shell surface. A constant cross-section of 20 in. by 20 in. was used for the edge beams. Unit weight of the concrete was assumed to be 150 lb/ft^3. Concrete with a compressive strength of 3750 psi was used. A single layer of uniform, orthotropic reinforcement parallel to the two straight line generators was nominally designed to resist the maximum membrane forces and bending moments. The edge beams were designed as eccentrically loaded columns to resist the maximum axial forces and bending moments. As shown in Fig. 5.41(a), the structure is symmetrical with respect to two vertical planes, XZ and YZ, therefore only one quadrant of the shell needs to be analyzed. The finite element mesh used, designated as 8 x 8, is also shown in Fig. 5.41(a). Material properties are given in Fig. 5.41(b). The edge beams were treated as thickened shell elements. Each element was divided into 10 layers of equal thickness.

The HP shell is known for the predominant participation of membrane action in load transference. It is also recognized that the simple triangular shell element used in this study

provides a poor representation of membrane action. In order to ensure the convergence of the solution with decreasing mesh size, linear analyses with different mesh sizes were conducted for the design loads using the NARCS program developed as part of the present study. The resulting vertical deflection, axial force and bending moment for one of the edge beams are shown in Fig. 5.42. Also shown for comparison are results from the SAP program, which uses Clough and Felippa's quadrilateral element (refer to Section 3.5). Convergence of the NARCS solution towards the SAP solution with decreasing mesh sizes can be observed. Since the purpose of this example is only to demonstrate the applicability of the method to shells of double curvatures, the 8 x 8 coarse mesh is chosen for the nonlinear analysis.

The resulting nonlinear load-deflection curve is shown in Fig. 5.43. The structure exhibited no cracking under design load, namely dead load plus 20 lb/ft^2 live load. Cracking propagated slowly during the following overloading until a live load of 110 lb/ft^2 was reached. The crack directions were generally parallel to the parabolic arch connecting the crown point and the two low points, Fig. 5.40(b). At 110 lb/ft^2 live load, the crack propagation reached the parabolic ridge connecting the two high points and the crown point. At the following load increment, the shell abruptly failed with a cantilever type failure mechanism. Also shown in Fig. 5.43 are the axial force and the bending moment at section B-B of

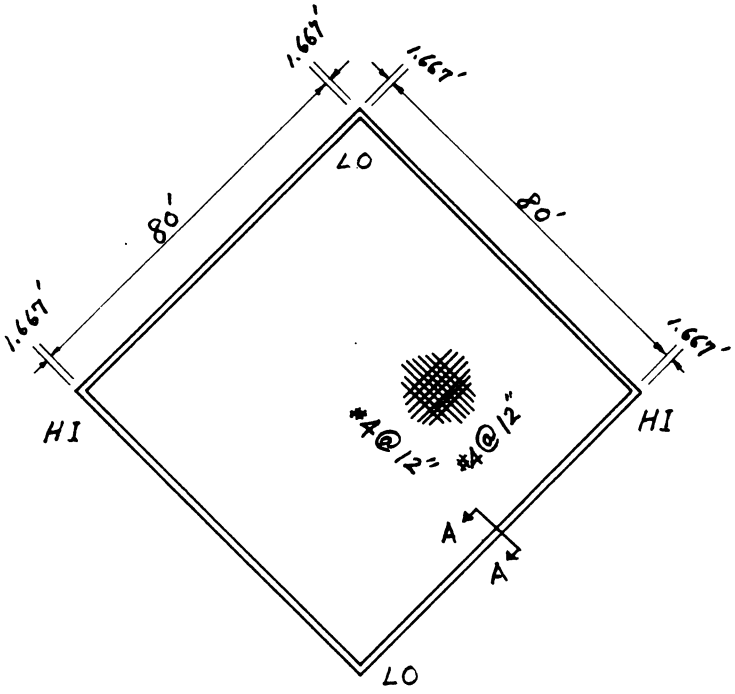

(a) PLAN

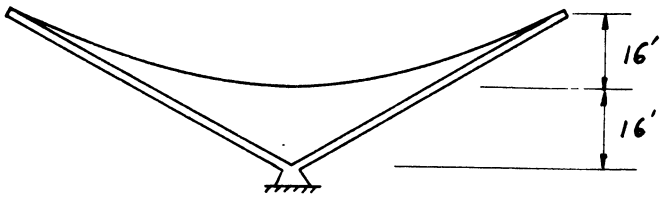

(b) ELEVATION

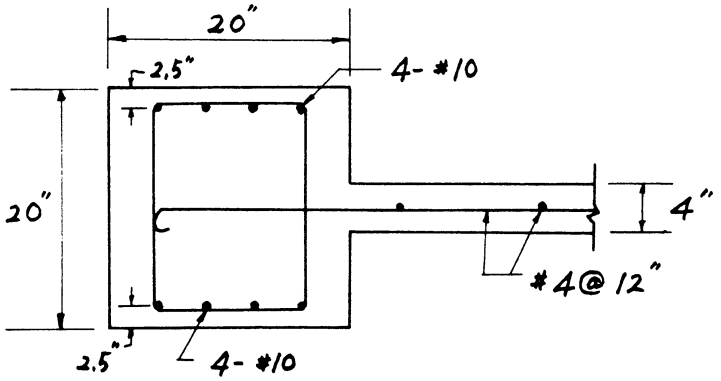

(c) SECTION A-A

FIG. 5.40 EXAMPLE 7 -- HP SHELL

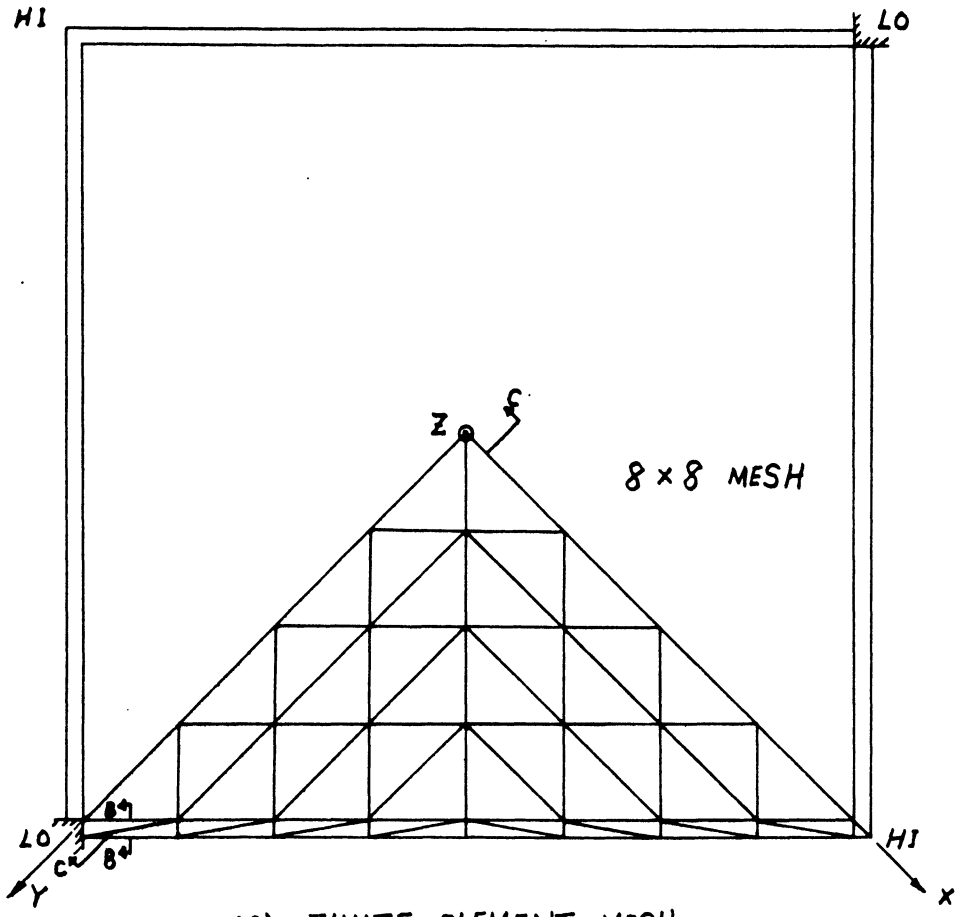

(a) FINITE ELEMENT MESH

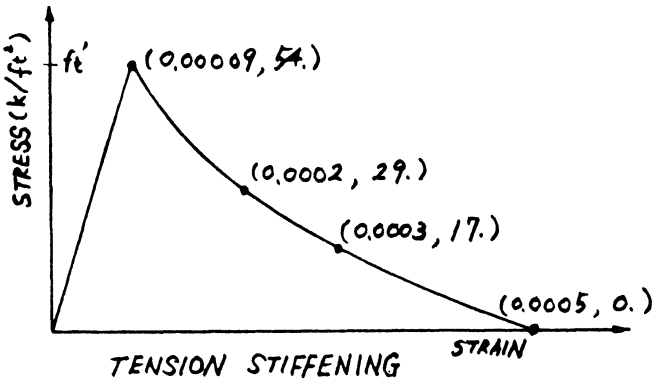

$E_c = 5.36 \times 10^5$ k/ft²

$f_c' = 540$ k/ft²

$f_t' = 54$ k/ft²

$\nu = 0.15$

$E_s = 4.18 \times 10^6$ k/ft²

$f_y = 8640$ k/ft²

$\alpha = 1.0$

(b) MATERIAL PROPERTIES

FIG. 5.41 FINITE ELEMENT MESH AND MATERIAL PROPERTIES - EXAMPLE 7

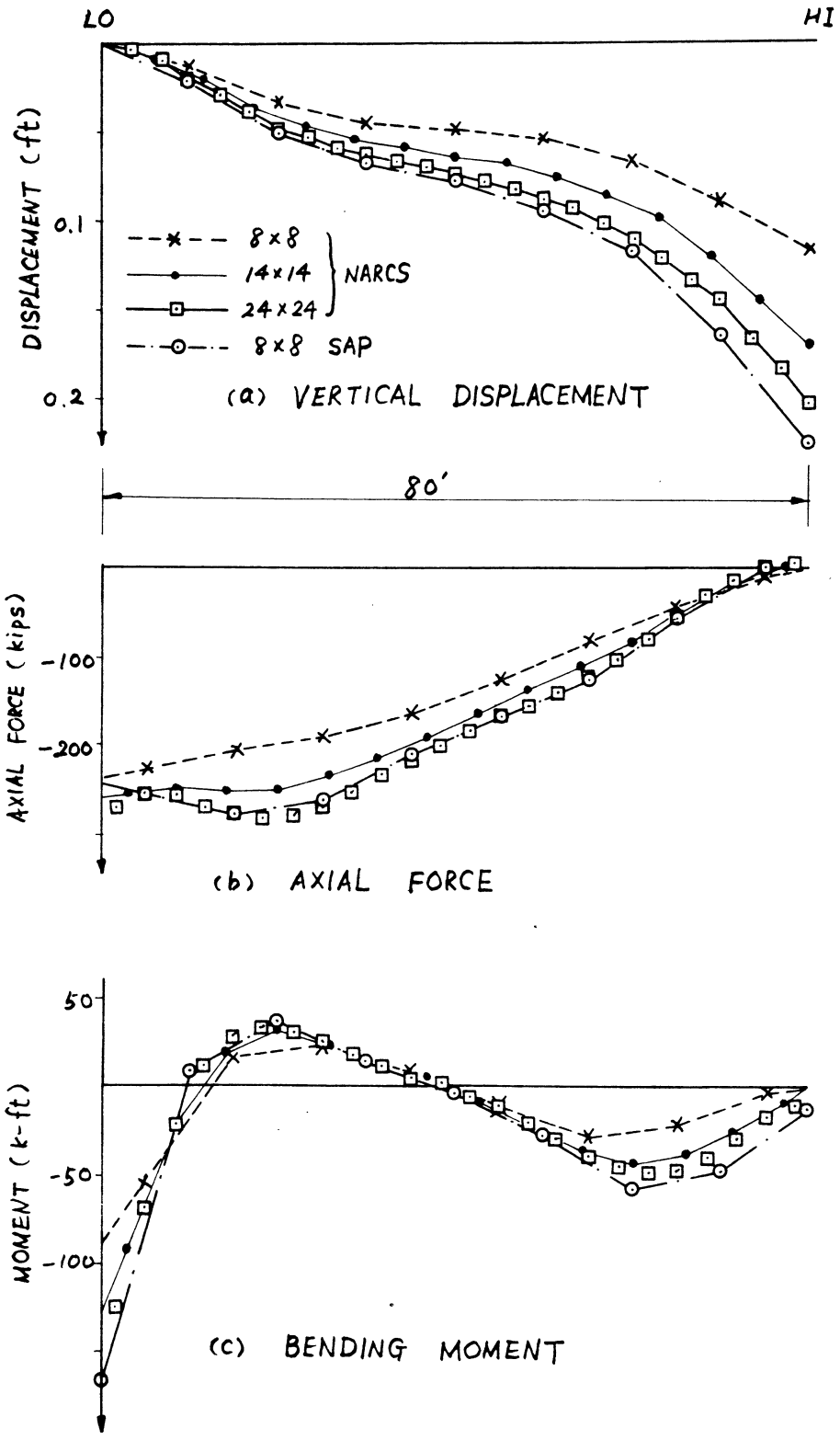

FIG. 5.42 DISPLACEMENTS AND FORCES IN THE EDGE BEAM FROM LINEAR ANALYSES -- EXAMPLE 7

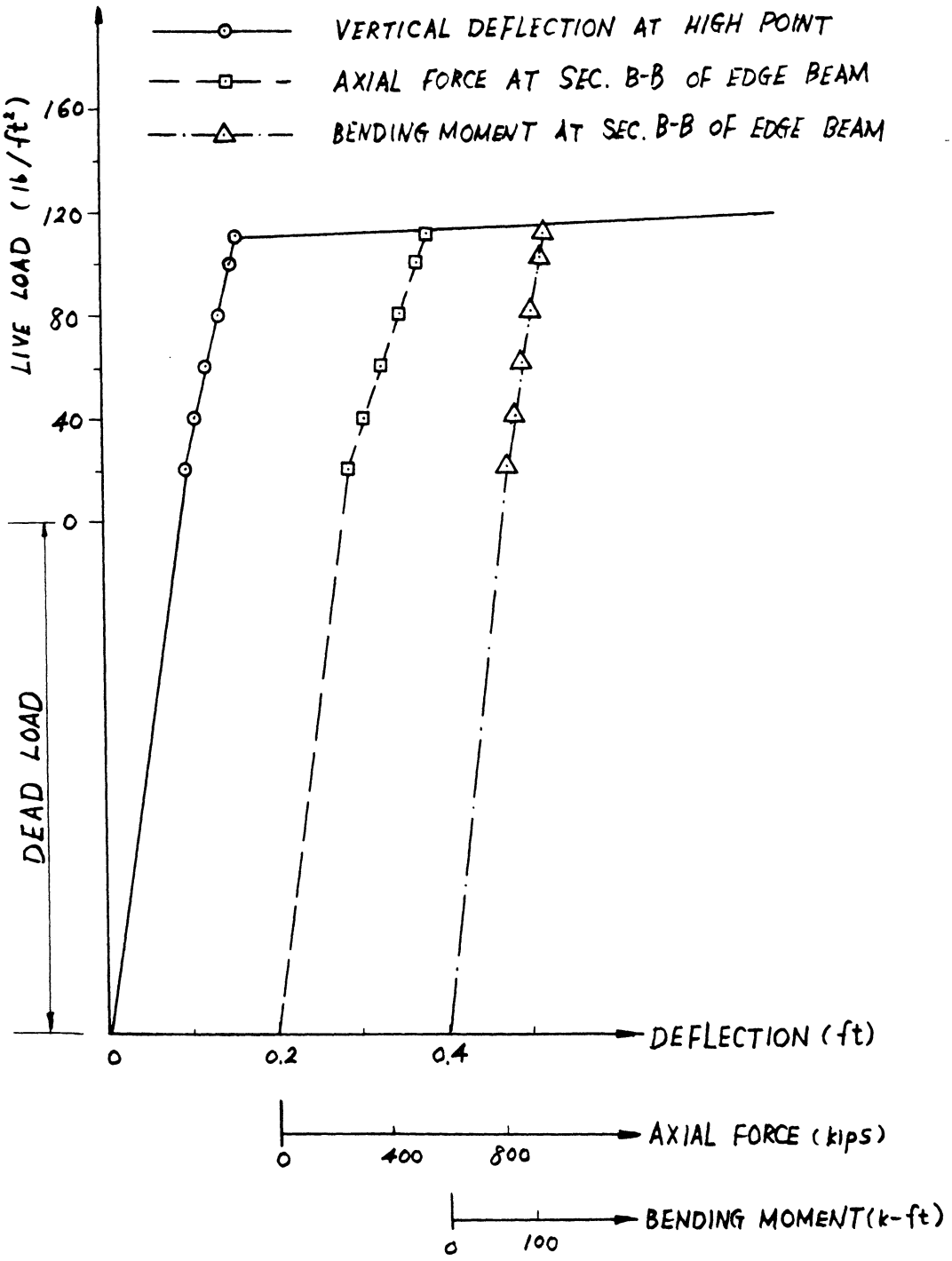

FIG. 5.43 NONLINEAR RESPONSE HISTORY
FOR EXAMPLE 7

an edge beam (Fig. 5.41a). It can be observed that the responses of the deflection, the axial force and the bending moment are almost linear up to the failure load. This indicates that the stress redistribution due to cracking is very localized, thus the global behavior of the shell is almost linearly elastic up to the ultimate stage where a brittle type failure occurs abruptly. In conclusion, the analysis shows the tremendous load carrying capacity, dead load plus 5.5 times design live load, of the lightly-reinforced HP shell, and its lack of ductility during failure.

A static check was made at cross-section C-C in Fig. 5.41(a). for the ultimate load. The calculation is summarized as follows.

Force:	Tensile	420 kips	} should be equal
	Compressive	470 kips	
	Error	11%	
Moment:	Internal	5350 kip-ft	} should be equal
	External	6010 kip-ft	
	Error	11%	

The results were considered satisfactory for the coarse finite element mesh used.

5.5 Computer Time

The most distinct feature of the proposed incremental iterative procedure is the repetition of a series of linear analyses. The required computer time for the implementation

of NARCS program is approximately directly proportional to the total number of iterations. The total number of iterations is controlled by the magnitudes of load increments, convergence criteria and allowable maximum number of iterations for each increment.

The computation involved in each iteration consists of two major parts: (1) solving the equilibrium equations, (2) calculating the internal stresses and updating the element stiffness. The computer time required for the first part is directly proportional to NM^2, where N is the number of unknowns, M the half band width of the structure stiffness matrix. That for the second part is a function of the number of elements, the number of layers in each element and whether output is requested. In general the relative weight of equation solving time increases as the size of structure system increases.

Another distinct feature of the NARCS program is the large amount of bookkeeping using tapes, which requires a lot of additional peripheral processor (PP) time. The cost of PP time usually depends on the total central memory being used by the job. The effective time used for computing cost is the central processor (CP) time plus a fraction of PP time.

The computer time required for the preceding numerical examples on a CDC 6400 computer is tabulated in Table 5.1 for reference.

TABLE 5.1 COMPUTER TIME FOR THE EXAMPLES

EXAMPLE	NO. OF NODES	NO. OF ELEMENTS	NO. OF LOAD INCRE-MENTS	TOTAL NO. OF ITER-ATIONS	OUTPUT CODE*	ONE ITERATION		TOTAL		
						EQUATION SOLVING (SEC)	CP (SEC)	CP (SEC.)	PP (SEC.)	EFFECTIVE TIME (SEC.)
1	14	12	13	78	1	0.50	1.36	110	388	244
2	34	32	9	34	2	1.76	8.24	263	817	570
3	4	2	5	24	1	0.04	0.34	11	38	27
4	4	2	9	29	1	0.04	0.36	13	42	31
5	16	18	15	60	2	1.79	4.75	296	750	533
5 (FINE)	49	72	8	20	2	12.97	25.92	586	1098	902
6	84	128	9	41	1	32.34	44.67	1887	2797	4569
7	34	48	7	33	1	5.08	8.99	311	676	598

* NOTE: 1 indicates output for each load increment only

2 indicates output for every iteration

6. PARAMETER STUDIES

6.1 Introduction

The difficulty associated with attempting a stress analysis of a reinforced concrete system is mainly due to the complexity of the material nonlinearity. The difficulty is further enhanced by the complicated stress states existing in reinforced concrete shells. With the highly simplified material model of this study, there are still factors which cannot be determined quantitatively directly from experiments. The rarity of available experimental data on the shells makes the verification and parameter studies of the analytical method extremely difficult.

The parameters which will be studied in this chapter are limited to those of the analytical model, and the study resorts mainly to numerical experimentation.

6.2 Tension Stiffening Effect

In Chapter 2, the tension stiffening effect was introduced through the behavior of a reinforced concrete member subjected to uniaxial tensile forces. For flexural members, Fig. 6.1 schematically shows the stress distribution between two cracks. The concrete has zero stress at the cracks but gradually gains stress through the bond action between the steel and the concrete. Therefore the post-cracking average stress-strain relationship for concrete may be represented by an unloading curve. The shape of the curve is affected by many variables, such as size, spacing, concrete cover and the

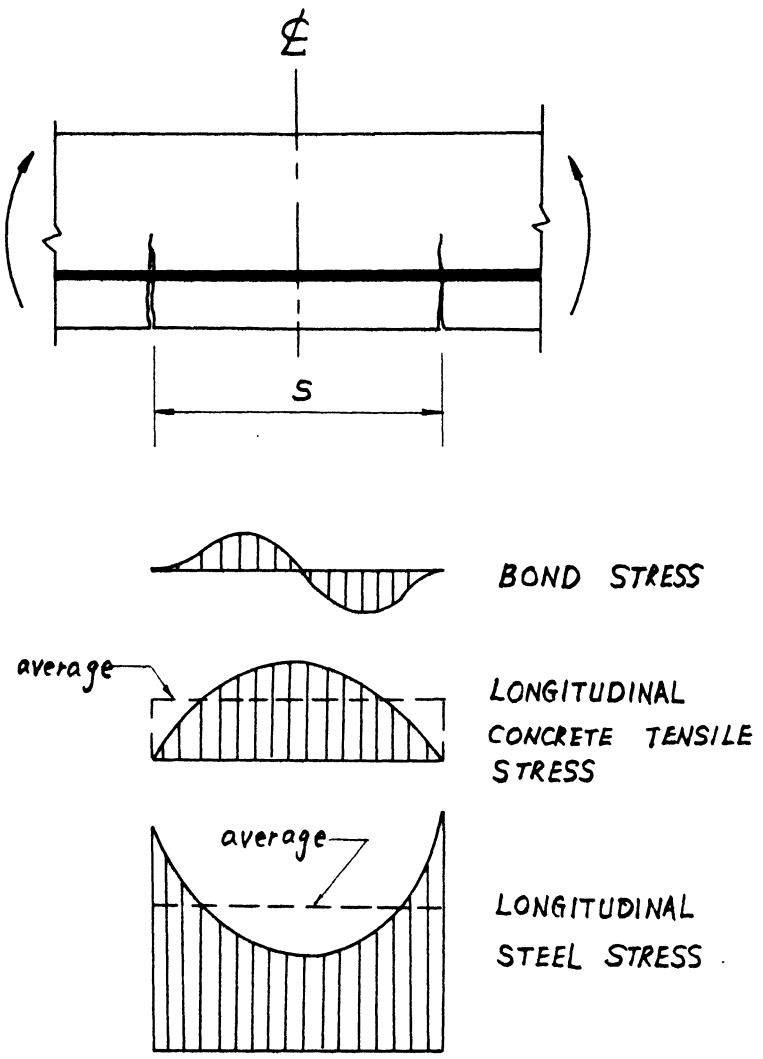

FIG. 6.1 SCHEMATIC STRESS DISTRIBUTION BETWEEN TWO CRACKS IN FLEXURAL MEMBER

surface characteristics of the reinforcing bars, and the strength of concrete, etc. However, the following three necessary characteristics of the curve can be deduced mathematically.

(1) $\sigma = f_t'$ in Fig. 6.2 constitutes the upper bound of the unloading curve.

(2) $\sigma = 0$ in Fig. 6.2 is the lower bound of the curve.

(3) The slope of the curve is less than or equal to zero.

It can be further observed that the average value of the concrete stress decreases as the crack spacing s (Fig. 6.1) decreases. Fig. 6.3(a) shows a typical crack pattern in a flexural member. Flexural cracks initiated from the tension side of the member penetrate to various depths. If the member is divided into an imaginary layer system over the depth, each layer will have various crack spacing. Among the six layers in tension in Fig. 6.3(a), crack spacings increase from layer 1 to layer 6. Therefore the average concrete stress should also increase from layer 1 to layer 6. This is reflected in Fig. 6.3(b), where the decreasing strains from layer 1 to layer 6 correspond to increasing stresses on the unloading curve.

In the finite element analysis, the tensile concrete stress is averaged throughout the element, once the cracking starts. The average stress decreases as the element gets smaller, similar to the effect of decreasing crack spacing. Consequently the tension stiffening unloading curve should

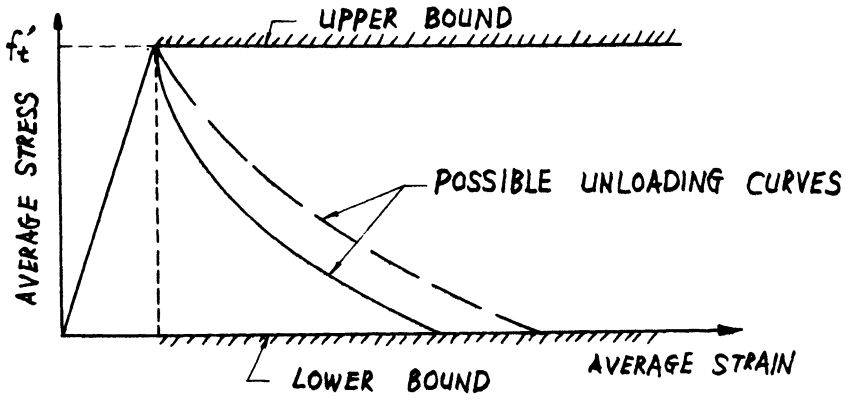

FIG. 6.2 UPPER AND LOWER BOUNDS OF THE TENSION STIFFENING UNLOADING CURVE

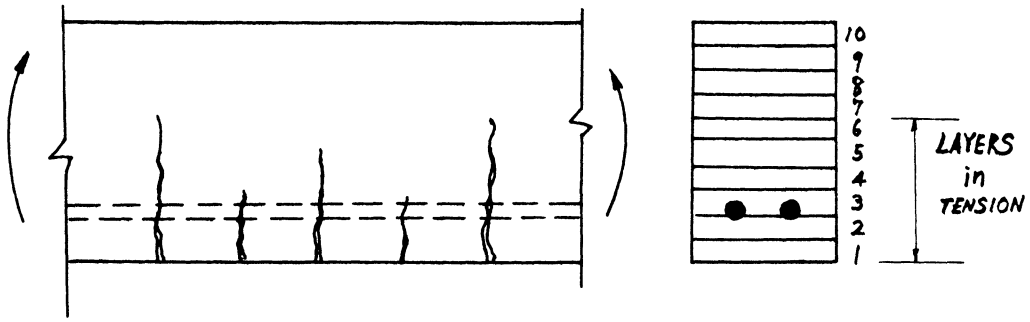

(a) CRACK PATTERN

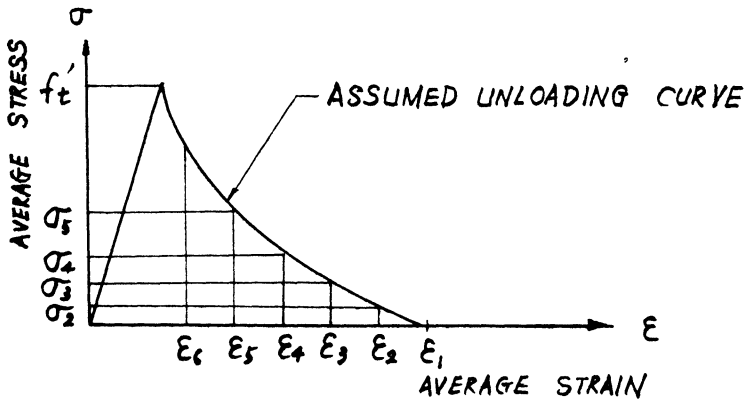

(b) LAYER STRESS VS. LAYER STRAIN

FIG. 6.3 TENSION STIFFENING IN THE LAYERED SYSTEM

also depend on the fineness of the finite element meshes. Theoretically the tension stiffening effect can be neglected if the elements approach infinitesimal size.

Despite the uncertainty of the unloading curve the existence of the tension stiffening effect is unquestionable. The following conclusions can be drawn from the experience in Chapter 5.

(1) The influence of the tension stiffening effect on the response of the reinforced concrete structures is very significant for under-reinforced cases, which constitute the majority of the slabs and shells.

(2) The behavior of the structure at the ultimate stage is not affected by tension stiffening.

(3) An unloading curve similar to the one in Fig. 5.12(b) is generally a reasonable estimate and usually yields satisfactory results.

6.3 Load Increments

As pointed out in Section 4.3, the tensile cracking of concrete is path-dependent, the elasto-plastic analysis for compressive concrete is valid only for small load increments. Therefore it is generally necessary to carry out the solution in a series of small load increments. However, numerical experiments in Examples 1A and 3 of Chapter 5 reveal that the results are not very sensitive to the magnitude of the increment. Considering all of the approximations introduced and the uncertainty of some of the parameters, the effect

of the magnitude of increment is not significant and practically negligible. The major concern in planning load increments is that the increments should be fine enough to capture the drastic changes of slope on the load-response curve. Usually finer increments can better trace the load response curve, but this consumes more computer time. It is generally more efficient to apply larger load increments at the earlier stages and smaller load increments at the ultimate stage in order to bracket the ultimate load more closely.

6.4 Convergence Criteria

Figure 6.4 shows the load-deflection curves for Example 1(a) with Type A tension stiffening using nodal displacement convergence criterion with different convergence tolerances. Similar curves using unbalanced nodal force convergence criterion are shown in Fig. 6.5. The applied loading increments are identical to those previously used in Fig. 5.3. The convergence of the solution with decreasing tolerance can be observed. Fig. 6.6 shows the relation between the total number of iterations and the tolerance. An almost linear relation can be found between the number of iterations and the logarithm of the tolerance.

The determination of the tolerance should be based on the desired accuracy of the results which is often dictated by the accuracy of measurement in an experiment. Both the

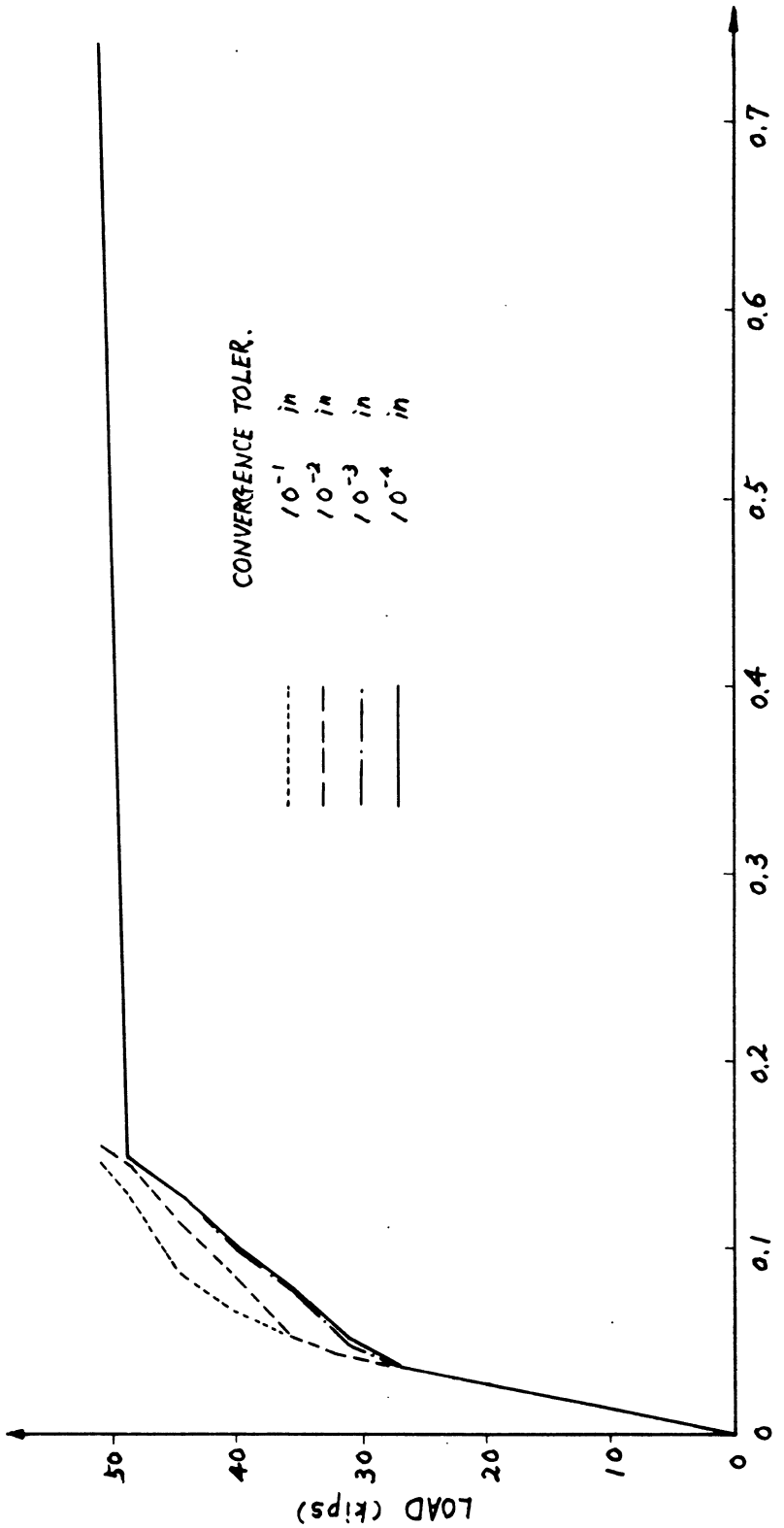

FIG. 6.4 CONVERGENCE STUDY -- NODAL DISPLACEMENT CRITERION

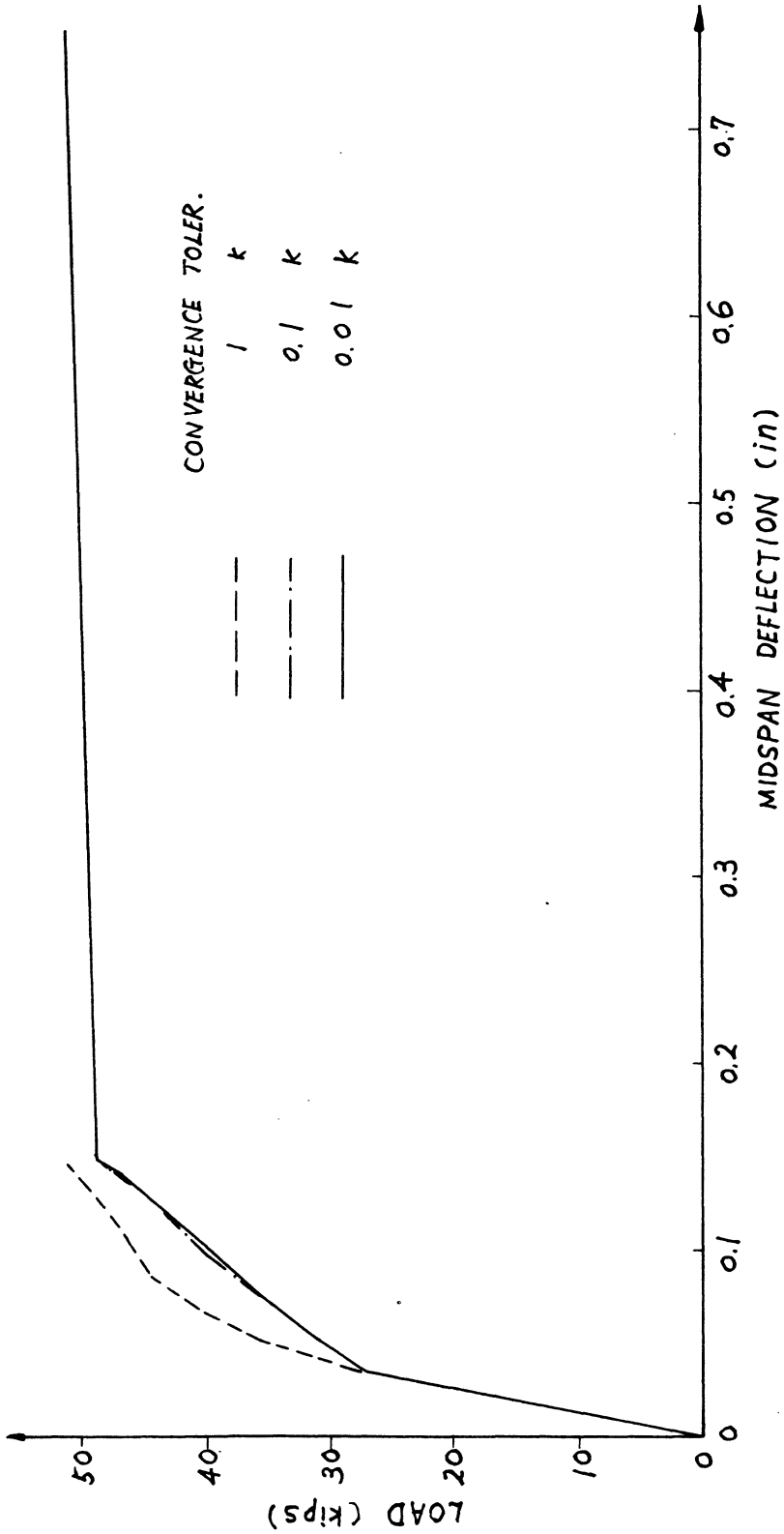

FIG. 6.5 CONVERGENCE STUDY - UNBALANCED FORCE CRITERION

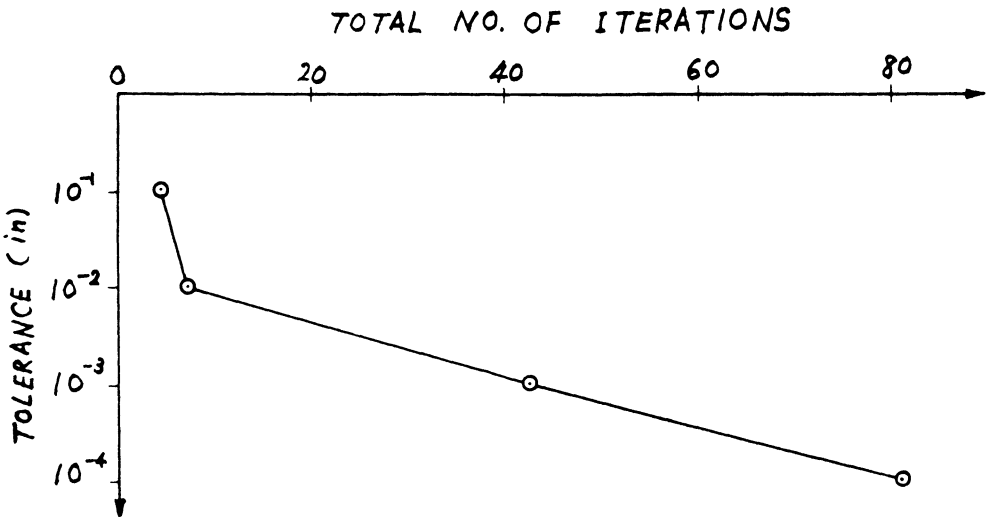

(a) NODAL DISPLACEMENT CRITERION

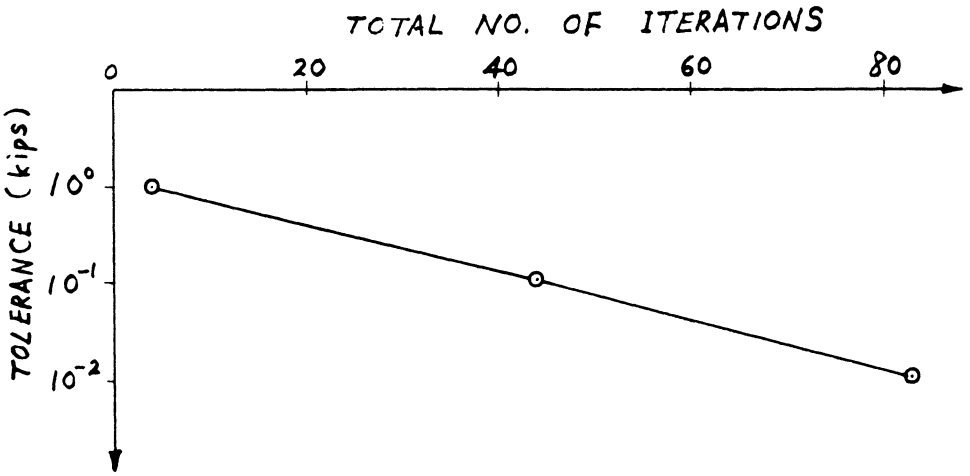

(b) UNBALANCED FORCE CRITERION

FIG. 6.6 COMPARISON OF CONVERGENCE CRITERIA

nodal displacement criterion and the unbalanced nodal force criterion guarantee the convergence to an approximate true solution. The choice between these two criteria should depend on the interest of the analyst. For an experimentalist who is mainly interested in the nodal displacements the nodal displacement criterion appears to be more desirable. On the other hand, a designer may find that the unbalanced nodal force criterion is more suitable because he is more concerned about equilibrium than the nodal displacements.

In the computer program developed for this study, the input convergence tolerance is in terms of components with respect to the global coordinate system rather than local coordinate systems. The use of an unbalanced nodal force criterion becomes very difficult for shell structures.

6.5 Yield Surface and Flow Rule

The adopted von Mises yield criterion is an approximation to the true failure surface, and the validity of its associated flow rule is purely a postulation. The majority of reinforced concrete structures are under-reinforced. Their nonlinear behavior is dominated by the tensile cracking of concrete and the yielding of reinforcement. For these under-reinforced cases, the concrete does not reach the yield state and thus it is obvious that the yield criterion and the flow rule chosen for the concrete are irrelevant.

In order to study the over-reinforced cases in which the concrete will reach yield state before failure, an

extreme case was chosen by modifying Example 5 to a highly over-reinforced slab by increasing the reinforcement ratio to 5% in both directions. The slab was reanalyzed using both the normality flow rule and the "unconstrained flow rule." The difference between the two results was found to be negligible. The extent of yielded region was very limited, and the movement of the stress vectors of yielded layers on the yield surface according to the normality flow rule was negligible.

Therefore, it is concluded that although the validity of any flow rule for concrete is still an open question, for the majority of cases where the yielded region is limited either the normality flow rule or the "unconstrained flow rule" can be applied with little danger of serious error. It should also be noted that the "unconstrained flow rule" has the distinct advantage of extreme simplicity, its adoption may enable one to approximate the true failure surface to almost any desired degree of accuracy without difficulty.

6.6 Cracked Shear Constant

The cracked shear constant is introduced to estimate the effective shear modulus along the cracks due to the effect of dowel action and aggregate interlock. Its value is bound between 0 and 1. In all the examples studied, it

is found that the solution is insensitive to the numerical value of the constant. Values ranging from 0 to 1 were tried, and very little difference was noted. In fact the shear stresses exist along the cracks were always found very small.

However, Hand et al. [1.25] in their latest work found that for a slab subjected to pure torsion an unstable crack configuration was attained with the cracked shear constant set to 0 when the load was approximately one-fourth of the experimental ultimate.

7. CONCLUSIONS

7.1 Summary

A nonlinear finite element method of analysis has been presented for analyzing reinforced concrete slabs of arbitrary geometry and free-form shells under dead loads and monotonically increasing live loads. The method is capable of tracing the load-deformation response and crack propagation, as well as determining the internal concrete and steel stresses through the elastic, inelastic and ultimate ranges in one continuous computer analysis. The nonlinearity due to material properties is considered in the analysis, but not the geometric nonlinearity.

A composite layer system consisting of concrete layers and smeared steel layers is constructed to account for the varied material properties within the finite element. The concrete is assumed to be elasto-plastic in compression, brittle in tension. Von Mises yield surface, the maximum principal stress crack criterion and an effective strain crush criterion are used to define the transition boundaries for different material states. The normality flow rule is adopted to govern the plastic behavior of concrete. The tension stiffening effect of the concrete between cracks is accounted for by releasing the unbalanced stress gradually according to a specified unloading curve. The steel is considered as a one-dimensional elasto-plastic material.

The shell surface is approximated as an assemblage of

flat triangular surfaces. Each triangle is represented by a flat triangular finite element with 5 degrees of freedom at each node. The element is derived from combining a linear curvature compatible triangular bending element with a constant strain triangular membrane element. The coupling effect between the membrane action and bending action is included. The problem of the missing "sixth" degree of freedom in the element formulation, corresponding to the rotation about an axis normal to the plane of the element, is overcome by attaching to each node of the assembled structure stiffness matrix a special boundary element with a high rotational stiffness about an axis normal to the shell surface.

An incremental tangent stiffness iterative procedure is used. Either the nodal displacement criterion or the unbalanced nodal force criterion can be prescribed for the convergence criterion.

Several numerical examples, including beams, slabs and shells, are studied to investigate the validity and applicability of the proposed method. Important parameters, such as the tension stiffening effect, load increments, convergence criteria, yield surface and flow rule, cracked shear constant, are also studied.

7.2 Conclusions

1. The proposed method of analysis appears to be a valid and powerful tool for the nonlinear analysis of reinforced

concrete slabs and shells for the cases or the ranges where the effect of large deformation is negligible.

2. The proposed material idealization is capable of capturing the dominant behavior of the reinforced concrete structures under monotonically increasing loads. For the majority of cases where the yielded region is limited, it is reasonably safe to apply either the normality flow rule or the "unconstrained flow rule."

3. The tension stiffening effect has a very significant influence on the post-cracking response of under-reinforced concrete structures, but not the behavior at the ultimate stage.

4. The adopted simple triangular shell element has the deficiency of poor representation of the shell membrane strains, but is very accurate in approximating the bending action. Therefore, the required fineness of element mesh to obtain reasonably accurate results depends on the predominance of the membrane action or bending action. A doubly curved shell generally requires a finer mesh than a slab.

7.3 Recommendations for Further Study

1. More experimental work is needed to assess the validity of the analytical method and to further improve the analytical model. It is believed that parallel interaction of analyses and experiments will surely lead to fruitful findings.

2. Major improvement in the efficiency of the method can be achieved by improving the membrane representation of the finite element.

3. Systematic parameter studies using the proposed method may yield improvement in the design practice of concrete slabs and shells, noting that the method is capable of treating varying thickness, arbitrary orientation and number of layers for reinforcement.

4. The analytical procedure may be extended to include geometric nonlinearity.

5. Extension of the method to include cyclic loading or load reversal can be done by constructing a simple realistic cyclic material model. However, extensive experimental study of the stress-strain relations for concrete under cyclic loading is imperative for the construction of the material model.

6. The method can also be extended to include creep, shrinkage and temperature effects.

REFERENCES

1.1 Ngo, D. and Scordelis, A.C., "Finite Element Analysis of Reinforced Concrete Beams," ACI Journal, Vol. 64, No. 3, March, 1967.

1.2 Ngo, D., Scordelis, A.C. and Franklin, H.A., "Finite Element Study of Reinforced Concrete Beams with Diagonal Tension Cracks," UC SESM Report No. 70-19, University of California, Berkeley, December 1970.

1.3 Nilson, A.H., "Finite Element Analysis of Reinforced Concrete," Ph.D. Dissertation, Division of Structural Engineering and Structural Mechanics, University of California, Berkeley, March 1967.

1.4 Nilson, A.H., "Nonlinear Analysis of Reinforced Concrete by the Finite Element Method," ACI Journal, Vol. 65, No. 9, September 1968.

1.5 Franklin, H.A., "Nonlinear Analysis of Reinforced Concrete Frames and Panels," Ph.D. Dissertation, Division of Structural Engineering and Structural Mechanics, University of California, Berkeley, March 1970.

1.6 Zienkiewicz, O.C., "The Finite Element Method in Engineering Science," McGraw-Hill Publishing Co., London, 1971.

1.7 Valliappan, S. and Nath, B., "Tensile Crack Propagation in Reinforced Concrete Beams - Finite Element Technique," Proceedings, Int. Conf. on Shear, Torsion and Bond in Reinforced and Prestressed Concrete, Coimbatore, India, January 1969.

1.8 Valliappan, S., Doolan, T.F., "Nonlinear Stress Analysis of Reinforced Concrete," Journal of Struc. Division, ASCE, Vol. 98, No. ST4, April 1972.

1.9 Zienkiewicz, O.C., Valliappan, S. and King, I.P., "Elasto-Plastic Solutions of Engineering Problems -- Initial Stress -- Finite Element Approach," International Journal for Numerical Methods in Engineering, Vol. I, 75-100, 1969.

1.10 Cervenka, V., "Inelastic Finite Element Analysis of Reinforced Concrete Panels under In-Plane Loads," Ph.D. Thesis, Department of Civil Engineering, University of Colorado, Boulder, 1970.

1.11 Mufti, A.A., Mirza, M.S., McCutcheon, J.O. and Houde, J., "A Study of the Behavior of Reinforced Concrete Elements Using Finite Elements," Structural Concrete Series No. 70-5, McGill University, Montreal, September 1970.

1.12 Youssef, A.A.-R., McCutcheon, J.O., Mufti, A.A. and Mirza, M.S., "Inelastic Analysis of Plates and Slabs Using Finite Elements," Structural Concrete Series No. 71-1, McGill University, Montreal, March 1971.

1.13 Youssef, A.A.-R., "Inelastic Bending of Rectangular Plates and Prestressed Concrete Slabs," M. Eng. Thesis, Department of Civil Engineering and Applied Mechanics, McGill University, Montreal, August 1971.

1.14 Mufti, A.A., Mirza, M.S., McCutcheon, J.O. and Spokowski, R.W., "A Finite Element Study of Reinforced Concrete Structures," Structural Concrete Series No. 71-8, McGill University, Montreal, October 1971.

1.15 Spokowski, R.W., "Finite Element Analysis of Reinforced Concrete Members," M. Eng. Thesis, Dept. of Civil Engineering and Applied Mechanics, McGill University, Montreal, May 1972.

1.16 Jofriet, J.C. and McNeice, G.M., "Finite Element Analysis of Reinforced Concrete Slabs," Journal of the Structural Division, ASCE, V. 97, No. ST3, March 1971.

1.17 Bell, J.C., "A Complete Analysis of Reinforced Concrete Slabs and Shells," Ph.D. Dissertation, Dept. of Civil Engineering, Univ. of Canterbury, Christchurch, New Zealand, 1970.

1.18 Bell, J.C. and Elms, D., "Partially Cracked Finite Elements," Journal of the Structural Division, ASCE, V. 97, No. ST7, July 1971.

1.19 Scanlon, A., "Time Dependent Deflection of Reinforced Concrete Slabs," Ph.D. Dissertation, Dept. of Civil Engineering, Univ. of Alberta, Edmonton, Dec. 1971.

1.20 Rashid, Y.R., "Ultimate Strength Analysis of Prestressed Concrete Pressure Vessels," Nuclear Eng. Design, V. 7, p. 334, 1968.

1.21 Rashid, Y.R. and Rockenhauser, W., "Pressure Vessel Analysis by Finite Element Techniques," Conf. on Prestressed Concrete Pressure Vessels, March 1967, The Institute of Civil Engineers, London, 1968.

1.22 Rashid, Y.R., "Analysis of Prestressed Concrete Nuclear Reactor Structures," unpublished notes presented at Conference on Prestressed Concrete Nuclear Reactor Structures, Univ. of California, Berkeley, March 1968.

1.23 Wahl, H.W. and Kasiba, R.J., "Design and Construction Aspects of Large Prestressed Concrete (PWR) Containment Vessels," ACI Journal, V. 66, No. 5, May 1969.

1.24 Yuzugullu, O. and Schnobrich, W.C., "Finite Element Approach for the Prediction of Inelastic Behavior of Shear Wall-Frame Systems," Structural Research Series No. 386, Dept. of Civil Engineering, University of Illinois, May 1972.

1.25 Hand, F.R., Pecknold, D.A. and Schnobrich, W.C., "A Layered Finite Element Nonlinear Analysis of Reinforced Concrete Plates and Shells," Structural Research Series No. 389, Dept. of Civil Engineering, University of Illinois, Aug. 1972.

1.26 Scordelis, A.C., "Finite Element Analysis of Reinforced Concrete Structures," Proceedings of the Specialty Conference on Finite Element Method in Civil Engineering, Montreal, Quebec, Canada, June 1 and 2, 1972.

2.1 Hsu, T.T.C., Slate, F.O., Sturman, G.M. and Winter, G., "Microcracking of Plain Concrete and the Shape of Stress-Strain Curve," ACI Journal, Vol. 60, No. 2, Feb. 1963.

2.2 Hsu, T.T.C. and Slate, F.O., "Tensile Bond Strength Between Aggregate and Cement Paste or Mortar," ACI Journal, Vol. 60, April 1963.

2.3 Slate, F.O. and Olsefski, S., "X-rays for Study of Internal Structure and Microcracking of Concrete," ACI Journal, Vol. 60, May 1963.

2.4 Buyukozturk, O., Nilson, A.H. and Slate, F.O., "Stress-Strain Response and Fracture of a Model of Concrete in Biaxial Loading," Dept. of Structural Engineering, Cornell Univ., Report No. 337, May 1970.

2.5 Buyukozturk, O., Nilson, A.H. and Slate, F.O., "Stress-Strain Response and Fracture of a Concrete Model in Biaxial Loading," ACI Journal, Vol. 68, No. 8, Aug. 1971.

2.6 Buyukozturk, O. and Nilson,A.H., "Finite Element Analysis of a Model of Plain Concrete with Biaxial Loads," Proceedings of the Specialty Conference on Finite Element Method in Civil Engineering, Montreal, Quebec, Canada, June 1 and 2, 1972.

2.7 Popovics, S., "A Review of Stress-Strain Relationships for Concrete," ACI Journal, V. 67, No. 3, March 1970.

2.8 Kupfer, H., Hilsdorf, H.K. and Rusch, H., "Behavior of Concrete under Biaxial Stresses," ACI Journal, V. 66, Aug. 1969.

2.9 Metz, Gene Alan, "Flexural Failure Tests of Reinforced Concrete Slabs," ACI Journal, January 1965.

2.10 Nawy, Edward G., "Flexural Cracking in Two-Way Concrete Slabs Reinforced with High Strength Welded Wire Fabric," ACI Journal, V. 61, No. 8, Aug. 1964.

2.11 Nawy, Edward G., "Crack Control in Reinforced Concrete Structures," ACI Journal, V. 65, Oct. 1968.

2.12 Morley, C.T., "Experiments on the Distortion of Steel Bars Across Cracks in Reinforced Concrete Slabs," Mag. of Concrete Research 18, March 1966.

2.13 Liu, T.C.Y., Nilson, A.H. and Slate, F.O., "Biaxial Stress-Strain Relations for Concrete," ASCE Structural Journal, May 1972.

2.14 Taylor, M.A., Romstad, K.M., Herrmann, L.R. and Ramey, M.R., "A Finite Element Computer Program for the Prediction of the Behavior of Reinforced and Prestressed Concrete Structures Subject to Cracking," CR 72.019, Department of Civil Engineering, University of California, Davis, June 1972.

3.1 Turner, M.J., Clough, R.W., Martin, H.C. and Topp, L.J., "Stiffness and Deflection Analysis of Complex Structures," Journal of Aeronautical Science, Vol. 23, 1956.

3.2 Courant, R., "Variational Methods for the Solution of Problems of Equilibrium and Vibrations," Bull. Am. Math Society, 49, 1-23, 1943.

3.3 Clough, R.W. and Tocher, J.L., "Finite Element Stiffness Matrix for Analysis of Plate Bending," Proceedings of Conference on Matrix Methods in Structural Mechanics, Wright-Patterson, A.F.B., Ohio, 1965.

3.4 Clough, R.W. and Felippa, C.A., "A Refined Quadrilateral Element for Analysis of Plate Bending," Proceedings of 2nd Conference on Matrix Methods in Structural Mechanics, Wright-Patterson, A.F.B., Ohio, 1968.

3.5 Carr, A.J., "A Refined Finite Element Analysis of Thin Shell Structures Including Dynamic Loadings," SESM 67-9, University of California, Berkeley, June 1967.

3.6 Wilson, E.L., "Solid SAP--A Static Analysis Program for Three Dimensional Solid Structures," SESM 71-19, University of California, Berkeley, March 1972.

3.7 Clough, R.W. and Johnson, C.P., "A Finite Element Approximation for the Analysis of Thin Shells," International Journal of Solids and Structures, Vol. 4, Pergamon Press, 1968.

3.8 Johnson, C.P., "The Analysis of Thin Shells by a Finite Element Procedure," SESM Report No. 67-22, University of California, Berkeley, Sept. 1967.

3.9 Scordelis, A.C., "Analysis of Continuous Box Girder Bridges," SESM Report No. 67-25, University of California, Berkeley, Nov. 1967.

3.10 Willam , K., "Finite Element Analysis of Cellular Structures," Ph.D. Dissertation, Division of SESM, University of California, Berkeley, Dec. 1969.

4.1 Issacson, E. and Keller, H.B., "Analysis of Numerical Methods," John Wiley & Sons, 1966.

4.2 Ralston, A., "A First Course in Numerical Analysis," McGraw-Hill, 1965.

4.3 Hildebrand, F.B., "Introduction to Numerical Analysis," McGraw-Hill, 1956.

4.4 Golomb, M. and Shanks, M., "Elements of Ordinary Differential Equations," 2nd edition, McGraw-Hill, 1965.

4.5 Bazant, Z.P., "Matrix Differential Equation and Higher Order Numerical Methods for Problems of Nonlinear Creep, Viscoelasticity and Elasto-Plasticity," International Journal for Numerical Methods in Engineering," V. 4, No. 1, January-February 1972.

4.6 Chi, H.M. and Powell, G.H., "Computational Procedure for Inelastic Finite Element Analysis," UC SESM 73-2, University of California, Berkeley, January 1973.

5.1 Bresler, B. and Scordelis, A.C., "Shear Strength of Reinforced Concrete Beams," Series 100, Issue 13, Structures and Materials Research, Department of Civil Engineering, University of California, Berkeley, June 1961.

5.2 Bresler, B. and Scordelis, A.C., "Shear Strength of Reinforced Concrete Beams," ACI Journal, Proceedings, V. 60, No. 1, Jan. 1963.

5.3 Cardenas, A. and Sozen, M.A., "Strength and Behavior of Isotropically and Nonisotropically Reinforced Concrete Slabs Subjected to Combinations of Flexural and Torsional Moments," Structural Research Series No. 336, Dept. of Civil Engineering, Univ. of Illinois, May 1968.

5.4 Hedgren, A.W., "A Numerical and Experimental Study of Translational Shell Roofs," Ph.D. Thesis, Princeton University, New Jersey, 1965.